The Dissertation Committee for Shruti Jain Certifies that this is the approved version of the following dissertation:

Modeling Competing Fracture for Dry Transfer of Thin Films to a Flexible Substrate

Committee:

Roger T. Bonnecaze, Supervisor

Kenneth M. Liechti, Co-Supervisor

Gyeong Hwang

C. Grant Willson

Wei Li

Modeling Competing Fracture for Dry Transfer of Thin Films to a Flexible Substrate

by

Shruti Jain

Dissertation

Presented to the Faculty of the Graduate School of

The University of Texas at Austin

in Partial Fulfillment

of the Requirements

for the Degree of

Doctor of Philosophy

The University of Texas at Austin

August 2018

Dedication

To my father who is my pillar of strength,

to my mother for her unconditional love and support,

to my brother for bringing joy in my life,

&

to Vivek for motivating me throughout this journey.

Acknowledgements

Pursuing graduate school at the University of Texas at Austin has been one of the best decisions of my life. These five years have been very rewarding professionally and personally, thanks to the amazing people I have met and worked with. My advisors Dr. Roger Bonnecaze and Dr. Kenneth Liechti, guided and supported me throughout my PhD. Their enthusiasm for science and research motivated me through this journey and I would like to thank them for being great mentors. I would like to thank my committee members - Dr. Gyeong S. Hwang, Dr. C. Grant Willson and Dr. Wei Li for their insights and suggestions that added value to my PhD work. I am also thankful to Dr. Seung R. Na whose expertise in experiments and finite element simulation packages led to meaningful collaborations expanding the scope of my dissertation. I am grateful to Dr. Wei Li, Dr. C. Grant Willson, Dr, Deji Akinwande, Dr. Michael Cullinan, Dr. Hao Xin, Dr. Xiaohan Wang and Tianhao Yang for the discussions and feedback I received during the graphene meetings. I also want to thank Dr. Chenglin Wu and Dr. Sundeep Palvadi for helpful suggestions on beam theory modelling and simulations.

I would like to take this opportunity to thank the members of the Bonnecaze group with whom I have shared office space, interesting discussions and fun times. Dr.Mark Ferraro, Dr. Talha Arshad, Dr. Michael Clements, Dr. Andrew Spann, Dr. Benjamin Huntington, Dr. Meghali Chopra, Dr. Akhilesh Jain, Dr. Fardin Khabaz, Mohammadreza Shafiei, Tianfei Liu, Soumik Das, Xilan Zhu, Steven Stanley and Yang Ban have all been very helpful and supportive. As a part of the NASCENT Student Council for three years, I also had the pleasure to work with Akhilesh Jain, Prabhakar Marepalli, Craig Milroy, Ian Ladner, Xin Xu, Akhila Mallavarapu, Margaret Payne and

Andrew Cochrane. We shared exciting times organizing and planning events and I have made lifelong friendships through these experiences. It was an absolute delight to work with Dr. Bonnecaze, Dr. S. V. Sreenivasan, Larry Dunn, Matthew Weldon, Janet Monaco, Darlene Yanez, Diane McNair and Risa Hartman. Their support was instrumental in the success of NASCENT events.

Over the years, I have lived with great roommates and supported each other during our graduate school journey. I am thankful to Ankita Chaudhary, Shrankhla Narya and Neha Nogia for creating memories I will cherish for life. I would also like to thank Paras Ajay and Amey Puranik for the amazing times together and sharing their wisdom on science, life and everything in between.

I do not have enough words to express my gratitude to my best friend and fiancé, Vivek Yadav, who has always been encouraging, supportive and for being my family away from home. Lastly, I would like to thank my parents Vipin and Nisha Jain for their unconditional love, my brother Samyak, and family for cheering me in tough times so I could reach this milestone.

Modeling Competing Fracture for Dry Transfer of Thin Films to a Flexible Substrate

Shruti Jain, Ph.D.

The University of Texas at Austin, 2018

Supervisors: Roger T. Bonnecaze, Kenneth M. Liechti

Dry transfer printing is where a thin film is transferred from a host substrate to a target substrate by taking advantage of the difference in adhesion between the thin layer and the substrates. This technique can lead to high throughput industrial-scale manufacturing of flexible devices using thin films and 2D materials. A major roadblock for applying the method is an inadequate understanding of how transfer printing depends on the material properties of the substrates and the thin film and their interfacial interactions, which limits the reliability of dry transfer methods. This dissertation provides this knowledge through computational analysis with cohesive zone models.

Two approaches are used: 2D finite element simulations and 1D finite difference beam theory models. Both mode I and mixed-mode fractures are simulated. Scaling equations are developed to quantify load, crack length, end rotation, damage zone length and mode-mix as a function of material and interface properties. Competing fracture during the transfer of a 2D material like graphene is simulated with finite element models in ABAQUS®. Two damage initiation criteria are used with cohesive zone models.

Interface strength is observed to be the primary factor affecting crack path selection for both damage criteria. Weaker interfaces break first, independent of the fracture energy. However, convergence issues with ABAQUS® are identified. So, fast, robust beam theory models are developed to understand the parametric dependence of crack growth on material and interface properties and captured in a fracture map.

In addition to 2D materials, transfer printing of thin films is also studied. Parameters such as interface defects, thin film thickness and interface properties are varied to understand crack growth in thin film transfer. Interface defects modeled as initial crack lengths are observed to be the most significant factor in determining the success of the transfer process. When interface cracks are of equal lengths, fracture energy determines the crack path selection for stiff thin films and thicker films whereas for soft thin films, interface strength determines which interface breaks. A strong correlation between steady state crack tip mode-mix and crack path selection is observed despite using a mode-independent fracture energy.

Table of Contents

List of Tables

List of Figures

Chapter 1: Introduction

Two-dimensional materials like graphene have interesting properties with applications in next generation electronics such as flexible solar cells and large area flexible displays. This chapter discusses these materials with a focus on graphene, its growth and transfer for device fabrication, followed by a discussion on transfer printing. Basic concepts of modeling techniques for the transfer process are described and an outline for the dissertation is presented towards the end of this chapter.

1.1 2D MATERIALS

Two-dimensional (2D) materials are freestanding atomic layers. Examples include graphene, transition metal dichalcogenides (TMDs) such as MoS_2, WS_2 and layered metal oxides like MoO_2 and TiO_2. Due to their atomic thicknesses, these materials exhibit unique physical and electrical properties that can be utilized in high performance sensors, electronics, gas separation, and catalysis. New classes of superconductors, metallic materials, semimetals, semiconductors and insulators can be fabricated with these materials [1].

1.2 GRAPHENE

One extensively studied 2D material is graphene. Graphene is a monolayer of carbon atoms packed in a hexagonal lattice. It is a building block for 0D fullerenes, 1D nanotubes and 3D graphite (Fig.1.1a) [2]. Graphene has a room temperature mobility of up to 15,000 $cm^2\ V^{-1}\ s^{-1}$, mean elastic modulus of 1-2 TPa, thermal conductivity of about 5000 $Wm^{-1}K^{-1}$ and 97.7% transparency [3]. Material properties such as mechanical flexibility, chemical durability, strength and elasticity, electrical and thermal conductivity among others make graphene a promising material for applications in electronics [4-7],

photonics [6, 8], energy storage devices [6, 9], gas sensors [6, 9-11] and bio-applications [6, 11-15]. According to a market report published by Transparency Market Research, the graphene electronics market was valued at USD 8.5 million in 2014, and it is expected to reach USD 1.2 billion by 2025 [16].

(a)

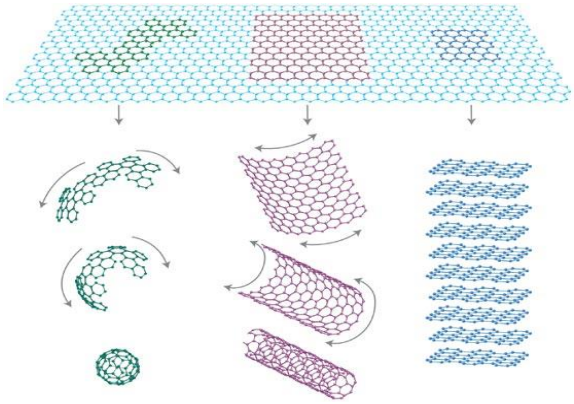

(b)

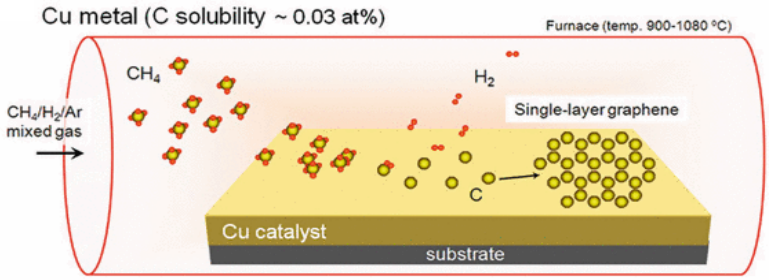

Figure 1.1: (a) Graphene: building block of carbon materials.[2] (b) Schematic of CVD growth process. [17]

Graphene is grown at a large scale using chemical vapor deposition (CVD) on a copper foil (Fig. 1.1b). CVD Graphene is formed by high temperature pyrolysis of carbon containing gases such as hydrogen and methane on transition metal substrates including Fe, Ru, Co, Rh, Ir, Ni, Pd, Pt, Cu and Au[18]. However, metal films like Ni and Co have

high carbon solubility which makes it difficult to control the amount of dissolved carbon atoms and hence, graphene growth yields non-uniform films[17]. In the case of Cu, low carbon solubility suppresses the dissolution of carbon atoms into the metal leading to a self-limiting mechanism to produce mono-layer graphene[19]. Multiple CVD recipes have been developed over the years for synthesis of graphene with different morphology and grain sizes.

1.2.1 Graphene Transfer

For device manufacturing of flexible electronics, graphene has to be transferred from the growth substrate (usually a copper foil) to a suitable substrate (silicon wafers or polymer films) without damaging the uniform layer or leaving residues on the graphene surface[20]. Existing transfer methods use polymer supports, etching or thermal release tapes. Electrochemical bubbling and dry transfer methods are also popular among researchers. Commonly used transfer processes for graphene are briefly described below.

1.2.1.1 Use of Polymer Support

Graphene transfer using polyimide (PI)[21, 22] and polymethyl methacralate (PMMA)[23] as supports have been reported by many researchers. In this approach the polymer support is spin-coated on the graphene layer which provides mechanical support for graphene when the growth substrate is etched away[7, 19, 24] or separated by bubbling[25] or peeling[22]. The graphene is then placed over the desired substrate and finally, the polymer support is removed by dissolution in a solvent. However, polymer residues left on the surface and solvent rinsing process may cause cracks in the graphene film[26]. Kang et al. [27] and Bae et al.[28] demonstrated a variation of this transfer process in a roll-to-roll mechanism (Fig. 1.2).

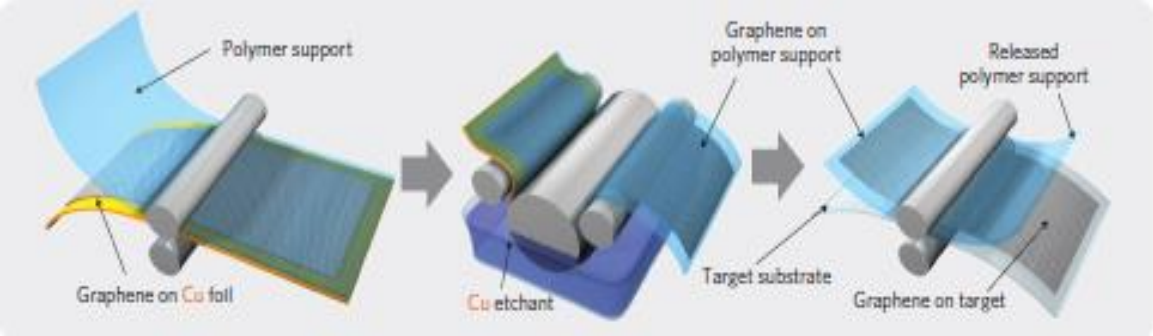

Figure 1.2: Schematic of the roll-to-roll transfer of graphene films from copper foils developed by Bae et al.[28].

1.2.1.2 Thermal Release Tapes

This transfer method was developed by Caldwell et al.[29] in which the tape adhesive sticks to the graphene layer and peels it from the growth substrate. The tape with the graphene is then placed onto the target substrate and heated to a temperature slightly above the tape's release temperature. The tape is then removed leaving behind the transferred graphene layer on the desired substrate.

1.2.1.3 Electrochemical Delamination

In this transfer process, PMMA is first spin-coated on the graphene/Cu samples as a protection layer and direct current voltage is applied to the PMMA/graphene/Cu cathode and a glassy carbon anode[30]. Hydrogen bubbles emerge at the graphene/Cu interface due to water reduction and detach the graphene film from the Cu foil at the edges. Permeation of electrolyte into the interlayers also aids the process. This technique is industrially scalable and allows reusability of Cu foil in multiple growth and delamination cycles[30]. Another variation was demonstrated by Gao et al. [31] using Pt foil as anode. Wang et al. [32] demonstrated a direct delamination process for transferring graphene to polyimide in five minutes.

1.2.1.4 Dry Transfer

Use of elastomeric stamps like PDMS for exfoliation or dry transfer is gaining popularity due to clean transfer without use of any etchants or solvents. Etchants are harsh, environmentally hazardous and expensive to dispose[33]. The ability of epoxy, PI and Polystyrene (PS) stamps to transfer graphene has been shown in recent years [34-37]. The method relies on speed dependent adhesion of stamps that pick up graphene when peeled from the growth substrate at a slow speed and deposit graphene on the target substrate when peeled away at a fast rate[38]. Use of elastomeric stamps like PDMS, PI and PS for exfoliation or dry transfer of graphene is gaining popularity due to clean transfer without use of any etchants or solvents and allowing reuse of copper foils [34-36]. Yoon et al. [34] demonstrated the dry transfer of graphene to polyimide by the assistance of an epoxy layer. A schematic of a dry-transfer process is shown in Fig. 1.3a.

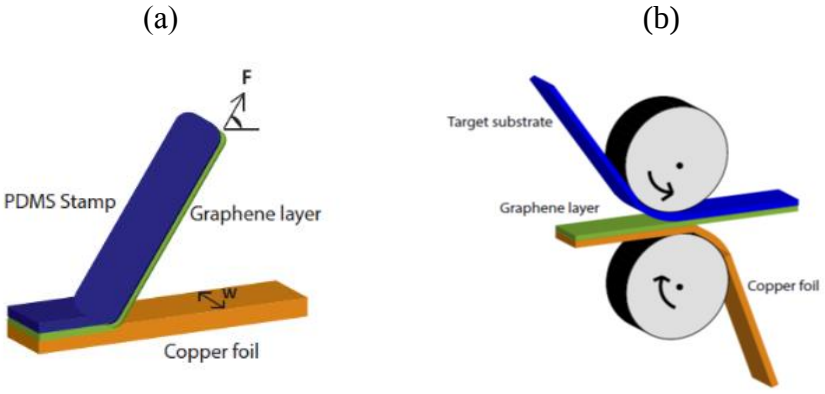

Figure 1.3: (a) Schematic of dry transfer of graphene onto a PDMS stamp (b) Roll-to-roll schematic for graphene transfer.

It would be desirable to transfer graphene to materials like polyethylene napthalate (PEN) and polyetherimide (PEI) which are flexible, transparent and have a high glass transition temperature using a roll-to-roll transfer mechanism as illustrated in Fig. 1.3b. Recently, Xin et al. [39] developed a roll-to-roll graphene transfer system and

achieved more than 98% graphene coverage at high film speeds. Understanding the adhesion mechanics and mixed-mode fracture mechanics of this transfer process also called transfer printing is important not only for graphene electronics but also for other 2D materials which may exhibit similar characteristics.

1.3 TRANSFER PRINTING

Transfer printing is a fabrication technique for microelectronics and other applications where a thin film is transferred from a host substrate to a target substrate by taking advantage of the difference in adhesion between the thin layer and the two substrates. This technique has been studied for the case of few microns thick layers [38, 40, 41] and has also been demonstrated to work for transferring two-dimensional (2D) materials like graphene [42]. A transfer printing schematic is shown in Fig. 1.4 where a thin film is transferred from a host substrate to a target flexible device substrate.

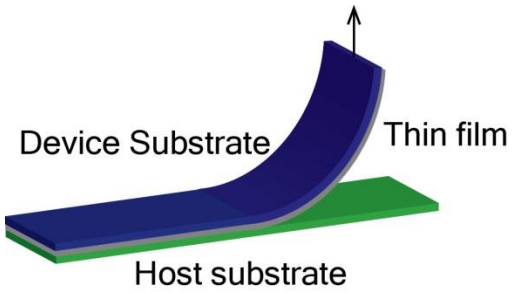

Figure 1.4: Schematic diagram of transfer printing of thin films.

Transfer printing was developed to generate structures smaller than 100 nm and categorized collectively with a few other non-lithographic patterning techniques as "soft lithography"[43]. A patterned PDMS stamp was used to print self-assembled monolayers (SAMs) to the surface of the substrate by contact and was first demonstrated for SAMs of alkanethiolates on gold [44] in 1993. Since then, the technique has been developed for the transfer of many other thin materials (or "inks") to a variety of substrates. Three basic

transfer printing modes are shown in Fig. 1.5 and the surface is modified to control adhesion between different substrates using chemical, thermal and mechanical strategies in all three modes of transfer.

Inorganic semiconductors like silicon [45, 46], GaAs, InP [47] and CdSe [48], metals such as gold [49], copper [50] and aluminum [51], carbon in the form of diamond [52], graphene [53] and carbon nanotubes [54], organic materials [55-57], colloids [58] and biological materials[59, 60] can be transferred to substrates in the form of nanomembranes, nanoribbons, nanowires, thin films, SAMs and quantum dots. Some examples of devices fabricated using transfer printing are shown in Fig. 1.6.

1.3.1 Mechanics of Transfer Printing

Transfer of the film relies on the competing forces associated with fracture at the interfaces between the film/host substrate and the film/target substrate. The delamination can be modeled as a crack initiation and propagation along the interfaces. Each interface has a characteristic toughness Γ and strength σ, which provide competing fracture pathways. Usually, the interface with the lower critical energy release rate cracks first [38]. For polymers like polydimethylsiloxane (PDMS) which show some viscoelasticity, the energy release rate required for growth exhibits a dependence on the velocity of the peel [61, 62] which sets a critical velocity above which the separation takes place.

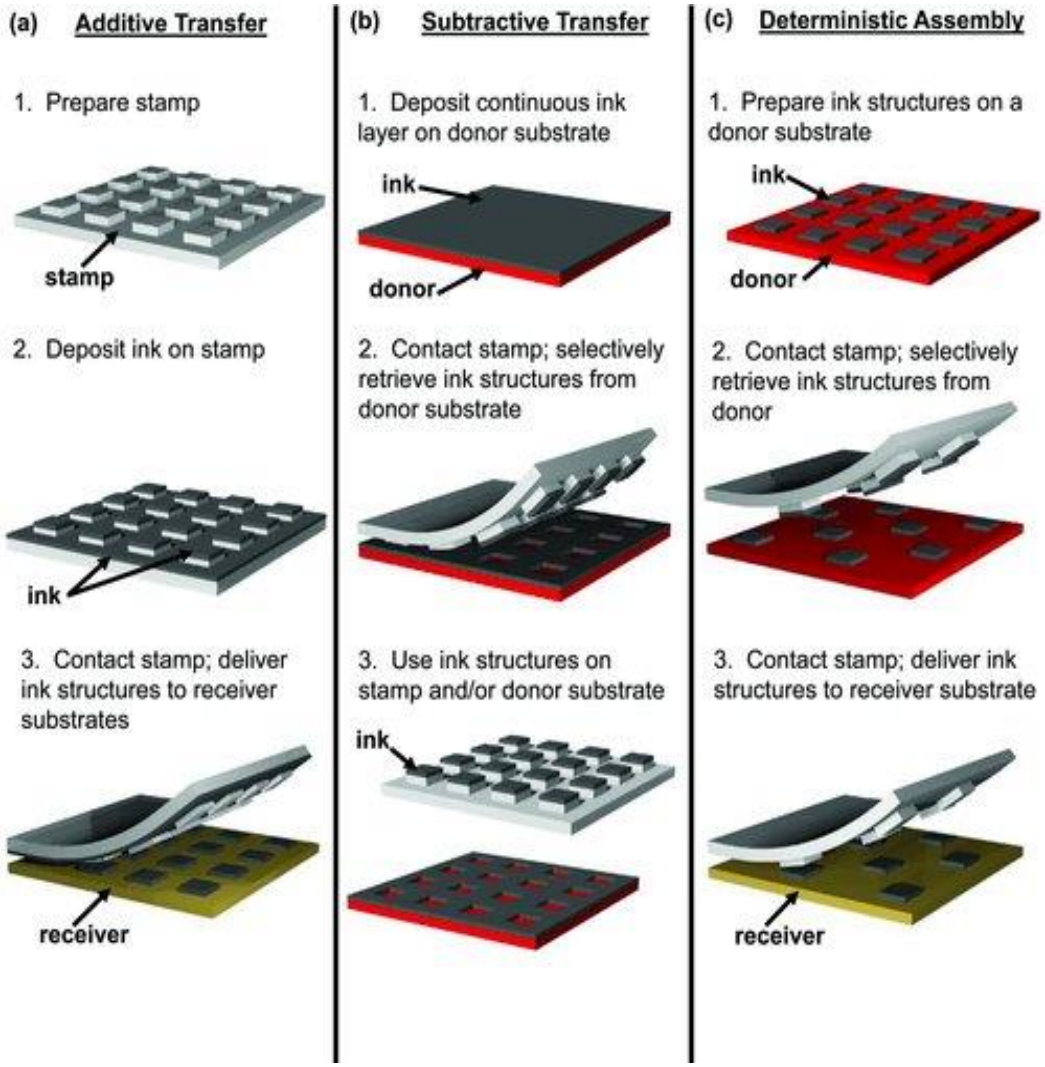

Figure 1.5: Schematic illustrations of transfer printing modes. (a) Additive Transfer (b) Subtractive Transfer (c) Deterministic Assembly. Images from [38].

(a) (b)

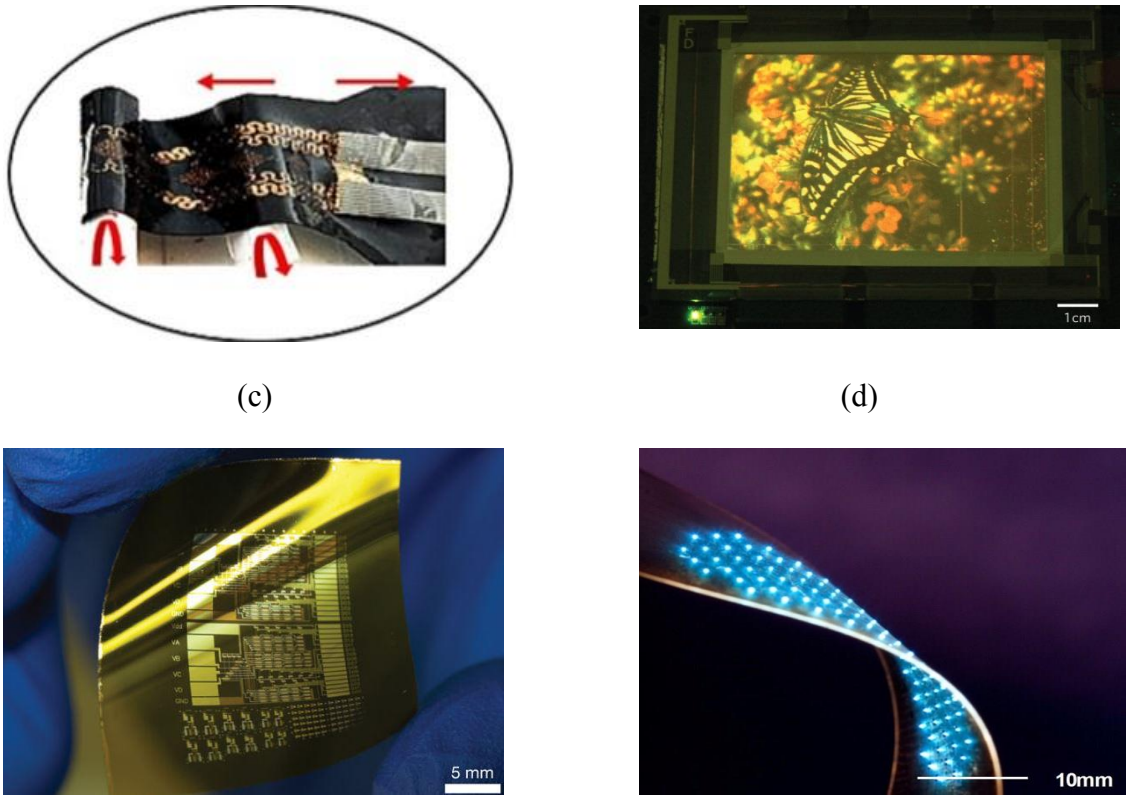

(c) (d)

Figure 1.6: (a) Skin-like electronics system that enables conformal lamination to the skin surface, which provides recording of skin temperature among other electrical signals [63]. (b) A 4-inch, full-color quantum dot LED display [48]. (c) Flexible integrated circuit that uses printed networks of single walled carbon nanotubes [64]. (d) Image of a flexed array of ultrathin, microscale LEDs printed from a source wafer onto a thin strip of plastic [65].

The criteria and speed dependence for transfer printing are often described with a semi-empirical power law relating energy release rate to velocity of peel (Eq. 1.1) [38].

$$\Gamma = \Gamma_0 \left[1 + \left(\frac{v}{v_0} \right)^n \right], \tag{1.1}$$

where Γ_0 is the critical energy release rate as indicated by a peel velocity v approaching zero, v_0 is the reference peel velocity at which the critical energy release rate doubles to Γ_0, and the exponent n is a scaling parameter that can be determined from experiments.

The power law relation (Eq. 1.1) however, fails to directly relate the fitting parameters to material properties and geometry of the thin films. In fact there is little fundamental understanding of crack propagation with competing interfaces. Transfer printing has many challenges such as obtaining strong adhesion between the thin film and target substrate, ensuring uniform coverage of the transferred film on the device substrate, avoiding cracks and defects in the thin layer during transfer, and achieving high throughput transfer for industrial manufacturing. Understanding the parametric relations that control the adhesion properties and quantifying the effect of competing interface interactions, mode-mix and viscoelasticity in this technique can improve the current manufacturing processes for transfer printing of graphene and thin films in general.

1.4 Fracture Mechanics

Transfer printing can be studied in terms of crack propagation at the interfaces of the intermediate thin layer with the host substrate and the device substrate. There are three types of loading that a crack can experience during fracture as illustrated in Fig. 1.7. In mode I, the principal load is applied normal to the crack plane. In-plane shearing is the principal load in mode II and out-of-plane shearing is the principal load in mode III

[66]. A combination of two or three modes is called mixed-mode fracture which is common in transfer printing.

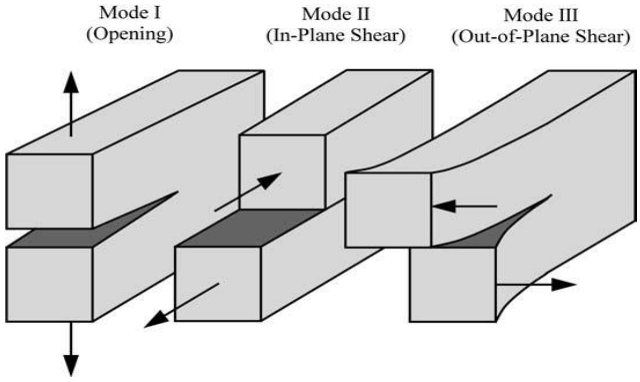

Figure 1.7: Three modes of loading that can be applied to a crack.[66]

Most often, the severity of cracks at interfaces between linearly elastic materials is defined in terms of the so-called energy release rate *G,* which is the rate of change of potential energy within the crack area [67]. At the moment of fast fracture, $G = \Gamma$ where Γ is the critical energy release rate, a measure of fracture toughness. For rate dependent fracture, growth is usually characterized by the dependence of the energy release rate during growth on the crack speed.

Another approach to define fracture is based on *K*, the stress intensity factor. Stresses near the crack tip in a linear elastic material are proportional to a calculable constant *K* given the crack geometry and loading. If the material of thickness *h* cracks locally at some critical combination of stress and strain, then fracture occurs at a critical stress intensity K_c. The three modes of fracture have different stress intensity factors differentiated by a subscript and are denoted as K_I, K_{II} and K_{III}. For a material with Young's modulus *E*, Poisson's ratio υ and shear modulus μ in plane strain,

$$G = K_I^2\left(\frac{1-\upsilon^2}{E}\right) + K_{II}^2\left(\frac{1-\upsilon^2}{E}\right) + K_{III}^2\left(\frac{1}{2\mu}\right). \tag{1.2}$$

The linearly elastic fracture mechanics (LEFM) approach just described ignores the microscopic mechanisms of fracture as all material aspects are lumped into one parameter, fracture toughness [68] and hence, has limitations for interfaces between thin layers [69]. A phenomenological approach that gets closer to the microscale interactions are cohesive zone models [70, 71], which have gained popularity to model interfacial fracture in thin films [72-74]. These models require specific parameters determined by the chemical and physical interactions at the interfaces. The stress in the cohesive zone ahead of the crack is a function of the separation between the two materials. Some examples of these traction-separation relations are shown in Figs. 1.8a-d.

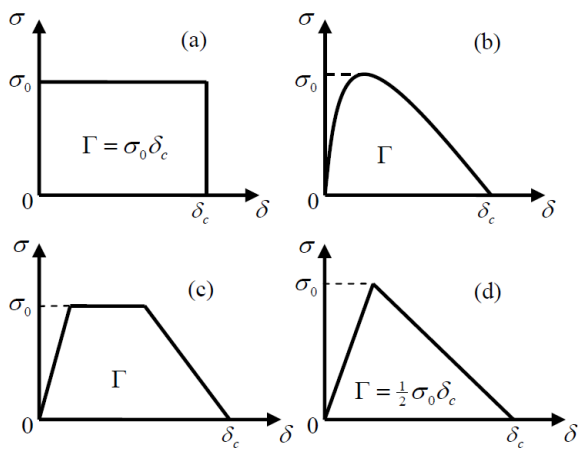

Figure 1.8: (a) Constant traction, (b) Smooth non-linear, (c) Trapezoidal, (d) Bilinear traction-separation relations [68].

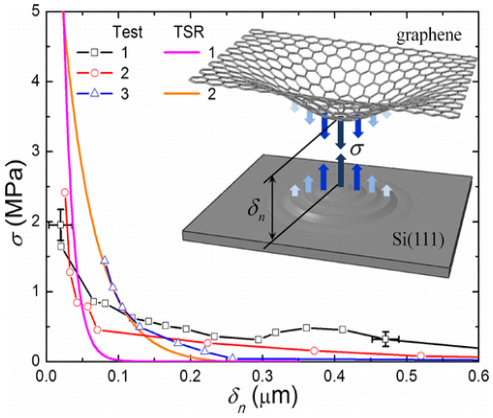

Figure 1.9: Traction-separation relation from experiment and cohesive zone model for graphene-silicon interactions [75].

The maximum stress σ_0 and critical displacement δ_c are the two most important parameters that characterize the traction-separation relation. The fracture toughness Γ can be obtained as the area under the traction-separation curve and proportional to the product $\sigma_0\delta_c$. Once the displacement in the cohesive zone reaches the critical value, the interface is fully damaged and the crack propagates. In cases where the cohesive length scale given by $E\Gamma/\sigma_0^2 h$ is greater than 0.4, LEFM fails to predict damage growth near the crack tip [76] indicating another advantage of using cohesive zone models. These traction-separation parameters can be determined experimentally and the model can be easily used in complex systems with multiple interfaces. A comparison of experimental data and traction-separation relations is shown in Fig. 1.9 for a wedge test experiment done by Na et al. [75].

Previous studies [73, 77, 78] have suggested that the shape of the traction-separation relation is secondary to the strength and toughness parameters. In this work a non-linear traction-separation relation with linear softening has been used to simulate crack initiation and growth at the interfaces, as shown in Fig. 1.8d. The interface initially

opens elastically with initial stiffness K when subject to an opening stress σ until the stress reaches the interface strength value $\sigma = \sigma_0$. Damage initiation occurs at this nominal stress and a damage parameter D (0 < D < 1) describes the state of the interface using equation 1.3 [69].

$$D = \frac{\delta_c(\delta_m - \delta_0)}{\delta_m(\delta_c - \delta_0)}. \tag{1.3}$$

Here, δ_0 is the critical separation for damage initiation and δ_m is the maximum separation that the interface element experiences over the entire loading history. When δ_m equals δ_c, D = 1 and σ = 0 indicating that the interface element is fully fractured. The fracture energy release rate, $\Gamma = \sigma_0\delta_c / 2$ for the linear softening model.

1.5 Research Questions Addressed by this Dissertation

The flexible electronics market is expected to grow from US $24 billion in 2018 to US $40 billion by 2023 [79]. Thin film transfer is an extremely useful manufacturing process for such devices. However, there is limited understanding of the mechanics of this process and no models for scale-up for industrial applications. This work aims to understand interface interactions in the transfer/peeling process to quantify how the competing interactions determine whether transfer of thin films and 2D materials is successful. Cohesive zone modeling is used to describe these interface interactions. Both mode I and mixed-mode transfer are studied with finite element method (FEM) simulations in ABAQUS after which semi-analytical beam theory models are developed to address the following questions-

- Can beam theory and scaling be used to create faster, more robust models in comparison to FEM?
- What are the important parameters and their relationships that determine the success of material transfer?

- What is the effect of mode-mix on material transfer?

1.6 OUTLINE OF DISSERTATION

In this research, models for thin film transfer of non-patterned 2D materials and micron-thick films have been developed using CZM to get a comprehensive understanding of the effect of geometry, material properties and interface properties on competing fracture. The dissertation is divided into six chapters:

- Chapter 2: covers the basics of single interface fracture mechanics in Mode I and discusses modeling and scaling analysis to yield algebraic equations for load, crack length and damage zone length.
- Chapter 3: develops a single interface mixed-mode fracture model followed by scaling and empirical equations for crack length, mode-mix, damage zone length and other process results.
- Chapter 4: FEM simulations and beam theory models are developed for graphene transfer and results indicate the importance of interface strength over fracture energy for successful transfer.
- Chapter 5: presents FEM simulation results for thin film transfer and discusses the interface selection with changes in film thickness, crack lengths, elastic moduli and a strong correlation with mode-mix.
- Chapter 6: offers concluding remarks on key results and future directions for further development of transfer printing models.

Chapter 2: Characteristic Scaling Equations for Softening Interactions Between Beams[1]

A reduced order analytical model for peeling of elastic thin films and interface fracture is presented by treating the thin film as a finite length beam with interface interactions accounted for by cohesive zone modeling. The results obtained are shown to be in excellent agreement with finite element simulations and experimental data. Scaling analysis and equations for steady state load and crack length are derived that clearly summarize their parametric dependence.

2.1 INTRODUCTION

From a continuum perspective, interactions between contacting surfaces, with their chemical, molecular and electrostatic origins, possibly mediated by moisture effects and surface roughness, can be represented by traction -separation relations through an approach that has come to be known as cohesive zone modeling. The approach can also be used to account for the behavior of thin adhesives layers between the beams. Perhaps the earliest exponent of this view was Prandtl [80]; Prandtl and Knauss [81], who considered the work done by the unloading tractions near the tip of a growing crack. This was followed by the approaches of Dugdale [70] and Barenblatt [82], who represented the interactions between the crack surfaces as a constant traction over the range of the interaction. While interactions between crack faces in monolithic bodies or at interfaces have been modeled in many configurations using traction–separation relations, the focus here will be mainly on the double cantilever beam.

Interactions between the surfaces of two beams were essentially first considered by Kanninen [83], who was interested in relaxing the common assumption of no rotation

[1] Much of this chapter appeared in "Characteristic scaling equations for softening interactions between beams ", Jain, S., Na, S.R., Liechti, K.M., Bonnecaze, R.T., 2016, Int J Fract 201, 1-9.

at the crack tip of a double cantilever beam specimen. The effect of an adhesive layer between two beams was represented in a similar manner by Chow et al. [84], where the elastic behavior of the adhesive layer provided the elastic foundation. Transverse shear effects were accounted for by Williams [85]. In all cases, the interactions between the beams were linearly elastic with no damage.

The case of damaged or softening interactions between the surfaces of two beams was first addressed by Ungsuwarungsri and Knauss [86]. The effect of several forms of traction-separations on the global load-displacement response was considered. Based on the forms of traction–separation relations that were considered, the rising portion of the load–displacement response was sensitive to the shape of the traction-separation relation. However this was not the case for the descending portion, which corresponds to steady state crack propagation. Guidelines were provided for extracting the unknown traction–separation relations associated with a particular interaction from a number of measurable characteristics associated with the response of double cantilever beam specimens. Stigh [87] considered the same problem but with a completely analytical approach where the continuity conditions were evaluated algebraically. The load in the rising portion of the load–displacement was initially linear, as expected, and consistently higher than the solution provided by Ungsuwarungsri and Knauss [86], suggesting a slight numerical error there. The problem was later reconsidered to include the effect of shear in a higher order beam theory, along with a broader range of exemplar traction–separation relations [88].

The softening behavior of a thin polyvinyl acetate layer sandwiched between two aluminum beams was obtained from measurements of the displacement of the upper surface of the double cantilever beam specimen as it was being separated [89]. The softening behavior was attributed to void formation ahead of the crack front. The

transverse loading of the double cantilever beam specimen does give rise to shear at the crack front. Its contribution to the energy release rate requires finite element solutions and cannot be obtained from steady state energy release rate arguments or higher order beam theories [76, 78]. As with any consideration of shear effects in beams, the contribution can become negligible for sufficiently long cracks. An expression for the J-integral associated with a double cantilever beam with softening interactions was developed in Gowrishankar et al. [69] using a completely analytical approach that was formulated for wedge testing. The results were used in the direct extraction of traction–separation relation parameters associated with interactions between silicon and epoxy. More recently, unknown interfacial properties were identified in a one-step algorithm in an integrated digital image correlation technique where the displacement kinematics embodied in a closed form solution of a double cantilever beam with interactions between the contacting surfaces were incorporated [90].

This chapter develops the analysis in sections 2.2 and 2.3, followed by a numerical and experimental validation of the approach in section 2.4. The results of a parametric study are presented in section 2.5 and form the basis of the scaling arguments developed in section 2.6.

2.2 BEAM THEORY AND COHESIVE ZONE MODELS

We consider symmetric double cantilever beams with cohesive interactions between the contacting surfaces (Fig. 2.1). The deflection of a beam with elastic modulus E, Poisson's ratio v and moment of inertia I is given by

$$E^* I \frac{d^4 w}{dx^4} = -q(x) \quad , \tag{2.1}$$

where $E^* = E/(1-\upsilon^2)$ in the case of plane strain and the interactions between the films are accounted for in the term q(x) in Eq. (2.1). We use a cohesive zone model (CZM) to characterize these interface tractions.

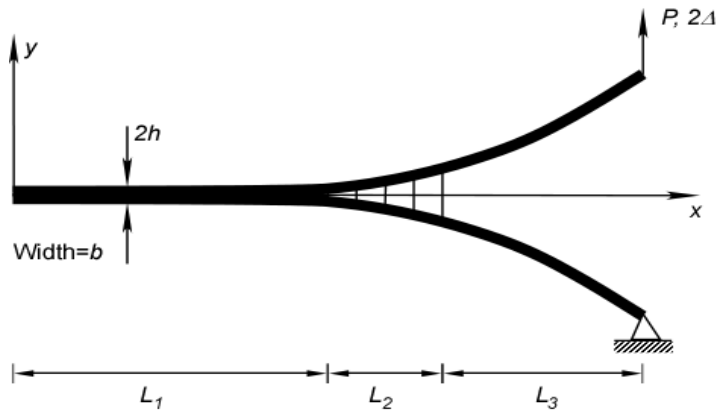

Figure 2.1: Schematic of double cantilever beam under fixed displacement and a force distribution at the interface. Region 1 is where the interface opens elastically, region 2 corresponds to the damage zone and region 3 is the separated free beam.

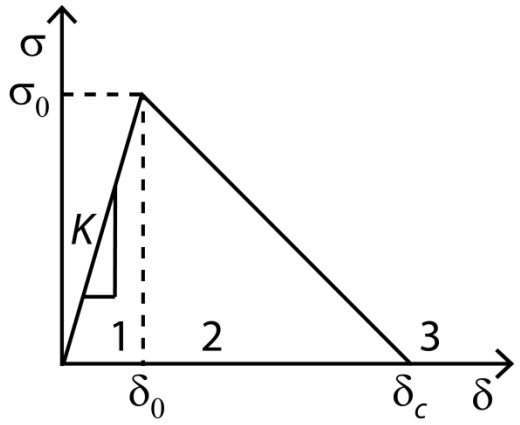

Figure 2.2: Bilinear traction-separation relation for an interface.

Cohesive zone models (CZMs) are phenomenological models that describe interfacial fracture between thin films [72-74]. These models require specific parameters of the traction–separation relation (TSR) as well as criteria for mixed-mode failure to make fracture predictions. Previous studies [73, 77, 78] have suggested that the shape of the TSR is secondary to the strength and toughness parameters. In this work a traction–separation relation with linear softening has been used to simulate crack initiation and growth at the interfaces, as shown in Fig. 2.2. The interface initially opens elastically with initial stiffness K when subject to an opening stress σ until the stress reaches the interfacial strength $\sigma = \sigma_0$. Damage initiation occurs at this nominal stress and a damage parameter D ($0 < D < 1$) describes the state of the interface [69] given by,

$$D = \frac{\delta_c(\delta_m - \delta_0)}{\delta_m(\delta_c - \delta_0)} \ . \tag{2.2}$$

Here, δ_0 is the critical separation for damage initiation, δ_c is the critical separation for fracture and δ_m is the maximum separation that the interfacial element experiences over the entire loading history. When $\delta_m = \delta_c$, we have $D = 1$ and $\sigma = 0$ indicating that the interface element is fully fractured.

The normal stresses for the three regions as shown in Fig. 2.2 are:

$$\sigma = \begin{cases} \sigma_0 \delta / \delta_0 : 0 \le \delta \le \delta_0 & (region\ 1) \\ \sigma_0(\delta_c - \delta)/(\delta_c - \delta_0) : \delta_0 \le \delta \le \delta_c & (region\ 2) \\ 0 : \delta_c \le \delta & (region\ 3) \end{cases} \tag{2.3}$$

Region 1 has a linear increase in stress corresponding to the elastic response of the interface, region 2 has linear damage, and region 3 is traction-free. The fracture toughness or energy release rate Γ is given by the area under the TSR curve, which

simplifies to $\Gamma = \sigma_0 \delta_c / 2$ for the linear softening model. Combining this TSR with beam theory gives rise to three separate equations for the three regions in a beam with interface tractions treated as externally distributed loads.

2.3 METHOD

Given the symmetry of the double cantilever beam setup, a thin film of width b, length L and thickness h with an initial crack length $a = 10h$ (to minimize the effect of shear) is considered with material properties and adhesion TSR parameters as listed in Table 2.1. Note that for the entire specimen, the fracture energy will be twice the value reported in Table 2.1.

Table 2.1: Material properties and TSR for model and ABAQUS simulations.

Layer	**Elastic modulus** E **(MPa)**	**Poisson's ratio** υ	**Interface strength** σ_0 **(MPa)**	**Stiffness** K **(MPa/mm)**	**Fracture Energy** Γ **(mJ/mm^2)**
Film	2500	0.34	-	-	-
Interface	-	-	1	100,000	0.01

The thin film is displaced at one end by Δ and the steady state crack growth solution for this configuration is obtained by solving the non-dimensional form of the following equations for the film:

$$E^* I \frac{d^4 w}{dx^4} = -\frac{\sigma_0 b w}{\delta_0} : 0 \le w \le \delta_0 \tag{2.4a}$$

$$E^* I \frac{d^4 w}{dx^4} = \frac{\sigma_0 b (w - \delta_c)}{\delta_c - \delta_0} : \delta_0 \le w \le \delta_c \tag{2.4b}$$

$$E^* I \frac{d^4 w}{dx^4} = 0 : \delta_c \le w \le \Delta \tag{2.4c}$$

These equations are non-dimensionalized by normalizing x with L and w with Δ to give the dimensionless equation set (2.5) where we have retained the notation for x and subscripted w for each region.

$$\frac{d^4 w_1}{dx^4} = -\lambda^4 w_1 : 0 \le w_1 \le \alpha_0 \tag{2.5a}$$

$$\frac{d^4 w_2}{dx^4} = \lambda^4 \alpha_0 \frac{(w_2 \Delta - \delta_c)}{\delta_c - \delta_0} : \alpha_0 \le w_2 \le \alpha_c \tag{2.5b}$$

$$\frac{d^4 w_3}{dx^4} = 0 : \alpha_c \le w_3 \le 1 \tag{2.5c}$$

Here $\alpha_0 = \delta_0 / \Delta$, $\alpha_c = \delta_c / \Delta$ and $\lambda = L[\sigma_0 b / (E^* I \delta_0)]^{1/4}$. The dimensionless boundary conditions and continuity of displacements, moments and shear across the interfaces between the regions are:

$$x = 0 : w_1 = 0 \tag{2.6a}$$

$$x = 0 : \frac{dw_1}{dx} = 0 \tag{2.6b}$$

$$x = \frac{L_1}{L} : w_1 = w_2 = \alpha_0 \tag{2.6c}$$

$$x = \frac{L_1}{L} : \frac{dw_1}{dx} = \frac{dw_2}{dx} \tag{2.6d}$$

$$x = \frac{L_1}{L} : \frac{d^2 w_1}{dx^2} = \frac{d^2 w_2}{dx^2} \tag{2.6e}$$

$$x = \frac{L_1}{L} : \frac{d^3 w_1}{dx^3} = \frac{d^3 w_2}{dx^3} \tag{2.6f}$$

$$x = \frac{L_1 + L_2}{L} : w_2 = w_3 = \alpha_c \tag{2.6g}$$

$$x = \frac{L_1 + L_2}{L} : \frac{dw_2}{dx} = \frac{dw_3}{dx} \tag{2.6h}$$

$$x = \frac{L_1 + L_2}{L} : \frac{d^2 w_2}{dx^2} = \frac{d^2 w_3}{dx^2} \tag{2.6i}$$

$$x = \frac{L_1 + L_2}{L} : \frac{d^3 w_2}{dx^3} = \frac{d^3 w_3}{dx^3} \tag{2.6j}$$

$$x = 1 : w_3 = 1 \tag{2.6k}$$

$$x = 1 : \frac{d^2 w_3}{dx^2} = 0 \tag{2.6l}$$

For a sufficiently long beam, the deflection in region 1 has the form given by Stigh [87]

$$w_1(x) = \left[c_1 \sin\left(\frac{\lambda x}{\sqrt{2}} \right) + \alpha_0 \cos\left(\frac{\lambda x}{\sqrt{2}} \right) \right] \exp\left(-\frac{\lambda x}{\sqrt{2}} \right). \tag{2.7}$$

Here, c_1 is a constant. Knowing the solution for region 1 helps us reduce the boundary conditions such that we can easily find solutions for regions 2 and 3, say with a shooting method. These reduced boundary conditions are:

$$x = \frac{L_1}{L} : \frac{1}{\lambda^3} \frac{d^3 w_2}{dx^3} - \frac{1}{\lambda} \frac{dw_2}{dx} + \sqrt{2} w_2 = 0 \tag{2.8a}$$

$$x = \frac{L_1}{L} : \frac{1}{\lambda^2} \frac{d^2 w_2}{dx^2} - \frac{\sqrt{2}}{\lambda} \frac{dw_2}{dx} + w_2 = 0 \tag{2.8b}$$

$$x = \frac{L_1 + L_2}{L} : w_2 = w_3 = \alpha_c \tag{2.8c}$$

$$x = \frac{L_1 + L_2}{L} : \frac{dw_2}{dx} = \frac{dw_3}{dx} \tag{2.8d}$$

$$x = \frac{L_1 + L_2}{L} : \frac{d^2 w_2}{dx^2} = \frac{d^2 w_3}{dx^2} \tag{2.8e}$$

$$x = \frac{L_1 + L_2}{L} : \frac{d^3 w_2}{dx^3} = \frac{d^3 w_3}{dx^3} \tag{2.8f}$$

$$x = 1 : w_3 = 1 \tag{2.8g}$$

$$x = 1 : \frac{d^2 w_3}{dx^2} = 0 \tag{2.8h}$$

For solving the initial unsteady crack growth in presence of an initial crack, we determined the end displacement at which damage zone begins to develop (Δ^*) by modifying the load based damage modeling [69] to a displacement control approach to obtain the following expression:

$$\Delta^* = \frac{\delta_0}{3}\frac{\left[3+2\left(\frac{\lambda a}{16L}\right)^3+6\left(\frac{\lambda a}{16L}\right)^2+6\left(\frac{\lambda a}{16L}\right)\right]}{\left(1+\frac{\lambda a}{16L}\right)} \quad . \tag{2.9}$$

For displacements greater than Δ^*, there will always be three regions described by the same equations (2.5, 2.7–2.8) with the exception of equations (2.8c–f) which change to equations (2.8c*–f*).

$$x = \frac{L-a}{L} : w_2 = w_3 \tag{2.8c*}$$

$$x = \frac{L-a}{L} : \frac{dw_2}{dx} = \frac{dw_3}{dx} \tag{2.8d*}$$

$$x = \frac{L-a}{L} : \frac{d^2w_2}{dx^2} = \frac{d^2w_3}{dx^2} \tag{2.8e*}$$

$$x = \frac{L-a}{L} : \frac{d^3w_2}{dx^3} = \frac{d^3w_3}{dx^3} \tag{2.8f*}$$

Analytical solutions for subsets of these equations have been studied in the past [69, 83, 86, 87] which required solving for multiple constants and many parameters affecting the peel test were suggested [91]. We used MATLAB to solve these equations numerically by starting with a guess for dw_3/dx and d^3w_3/dx^3 at $x=1$ and sequentially solving Eq. (2.5c) followed by Eq. (2.5b) and updating the guesses based on Eqs. (2.8a) and (2.8b) unlike the two-point boundary value problem approach employed by Ungsuwarungsri and Knauss [86]. This reduced order model with three dimensionless groups was then validated using finite element modeling (FEM) in ABAQUS as well as comparison with experimental data. We have extended prior work on analytical solutions by conducting a scaling analysis to find algebraic equations that quantify the elastic response length, damage length, crack length and load in terms of material properties and TSR parameters for a given end displacement in Mode I fracture.

2.4 Numerical and Experimental Validation

2.4.1 Numerical Validation with ABAQUS

The deflection of the film was determined using FEM simulations in ABAQUS with CPE4R (4-node bilinear plane strain quadrilateral, reduced integration) elements for thin films with L = 5 mm with a square mesh size of 10 μm. The solution for $w(x)$ and the load-displacement response for the two methods implemented in plane strain were compared (Fig. 2.3a–b) and excellent agreement was obtained in both cases, validating our beam theory model.

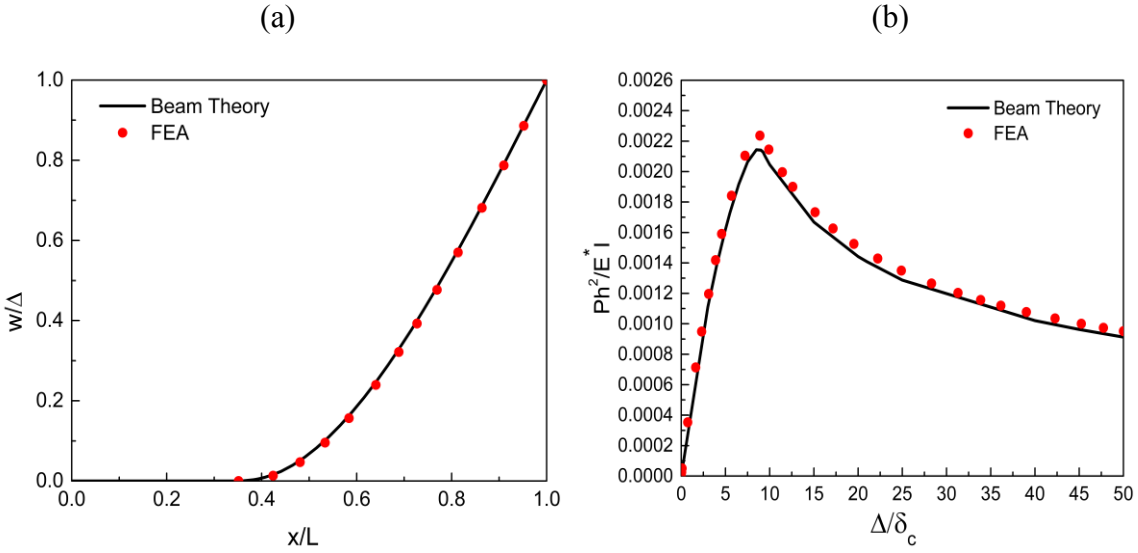

Figure 2.3: Comparison of analytical and numerical simulations: (a) displacement along the length of the beam, and (b) load–displacement response for Δ = 0.15 mm.

2.4.2 Experimental Validation

Na et al. [92] performed experiments to characterize the interactions between hydroxylated silicon surfaces from the perspective of cohesive zone modeling. They performed a wedge test and obtained the traction-separation relation for the interactions by using J-integral techniques and measurements of the crack opening displacements

(Fig. 2.4). Since the system is symmetric, we used our analytical model to find the steady state displacement solution for the top silicon layer and compared it with the reported experimental results. Properties of the silicon layer as well as the TSR as described in the paper are listed in Table 2.2. The comparison of the opening displacement along the crack length is shown in Fig. 2.5.

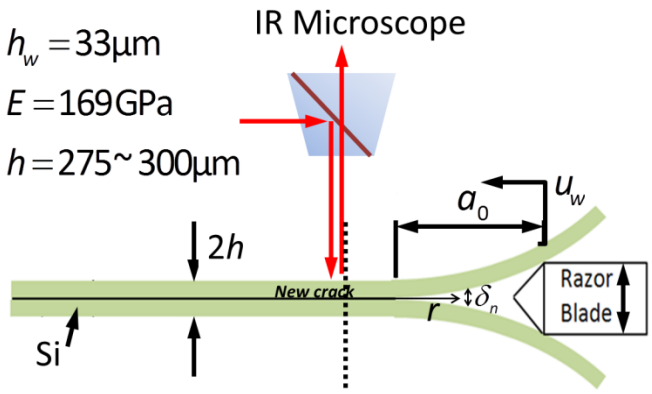

Figure 2.4: Schematic of the wedge setup [92].

Table 2.2: Material properties and TSR for experimental validation [92].

Layer	**Elastic modulus** E **(MPa)**	**Poisson's ratio** υ	**Interface strength** σ_0 **(MPa)**	**Stiffness** K **(MPa/mm)**	**Critical displacement** δ_c **(mm)**
Silicon	1.69×10^5	0.22	-	-	-
Interface	-	-	12	1.7×10^6	3.65×10^{-4}

The experimental data shows some variation in comparison to the simulation results due to the presence of repulsive interactions which are not accounted for in the selected traction-separation relation. Several potential sources of repulsive interactions and their repercussions on the normal crack opening displacements near crack fronts are

discussed in Na et al. [92]. Both numerical and experimental validation prove that our semi-analytical model captures the peeling process.

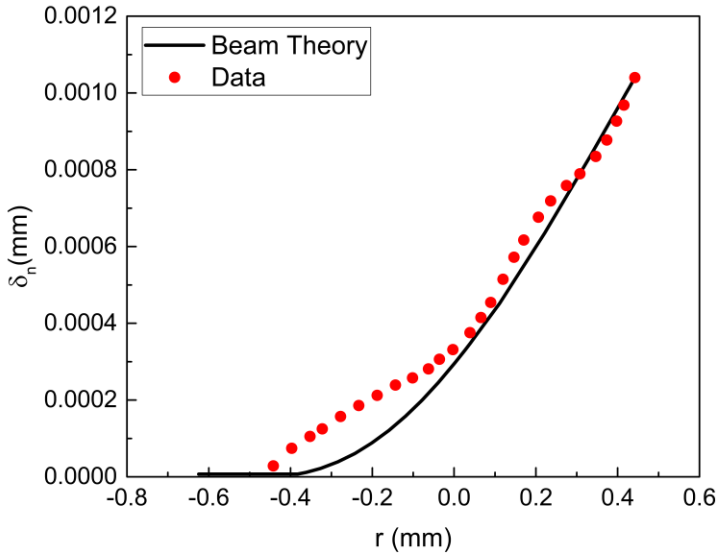

Figure 2.5: Normal crack opening displacements along the crack length.

2.5 RESULTS

We performed a parametric analysis to study the influence of different material properties and TSR parameters on the resultant load P, damage zone length L_2 and crack length L_3. A scaling analysis was then performed (as described in the Sect. 2.6) to obtain algebraic equations showing the exact dependence on the parameters. Results of the parametric analysis as well as their comparison with the scaling equations are described and illustrated in this section.

The variation in the load–displacement curve with change in δ_c, with K and σ_0 held constant is shown in Fig. 2.6a. It can be seen that the load increases for a TSR with higher δ_c (and hence, higher fracture energy, Γ). Evolution of the damage zone and crack length is illustrated in Fig. 2.6b where we can see the damage zone length L_2 steadily

increasing with normal displacement and then stabilize for steady-state crack growth. The crack length L_3 remains constant while the damage zone develops and once initiated, the crack keeps growing with increasing displacement.

(a)

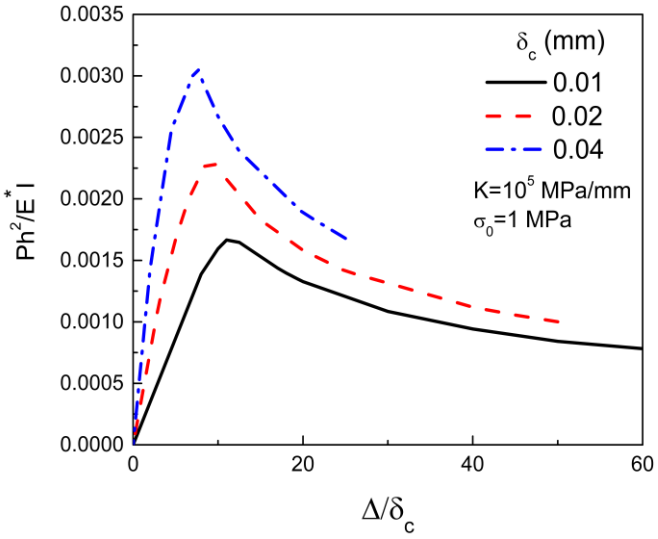

(b)

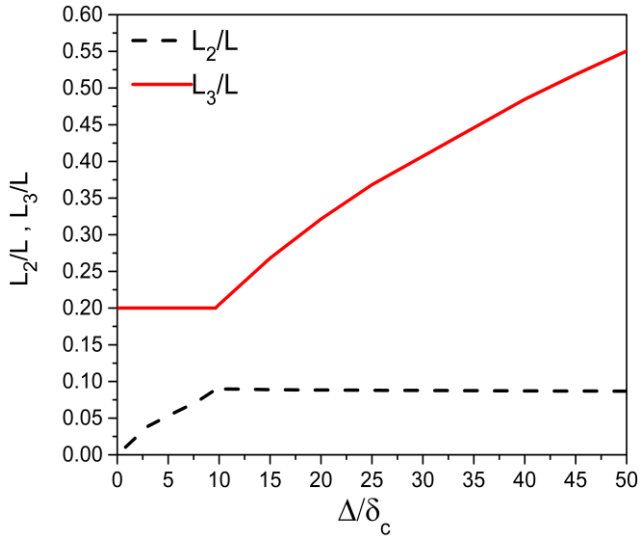

Figure 2.6: (a) Load-displacement response as a function of δ_c, and (b) damage zone and crack length as a function of Δ.

It has been suggested in earlier works [78, 93, 94] that the shape of the TSR and stiffness *K* have negligible effect on the fracture process. The results show that load and crack lengths are insensitive to δ_0 as shown in Fig. 2.7a-b but the interface strength σ_0 does effect the fracture propagation (Fig. 2.8). As expected, higher interface strength leads to a higher load for a given displacement. The scaling equation for load i.e. Eq. (2.13) captures the results well.

The effects of δ_c and σ_0 on L_2 and L_3 are shown in Fig. 2.9a-b. Here, $\alpha_0 = \delta_0 / \Delta$, $\alpha_c = \delta_c / \Delta$ and $\Lambda = (E^* \Delta) / (\sigma_0 h)$. It is clear that damage zone and crack length are longer for a TSR with higher δ_c and weaker interface strength. For Λ = 12,500 in Fig. 2.9a, both σ_0 and Δ were varied which results in some scattered points but the scaling equation still fits the data well.

2.6 DISCUSSION

In this section, we discuss our approach to a scaling analysis which provides explicit equations to calculate steady state load, damage zone length and crack length based on the material properties of the thin film and the TSR describing its interface with another substrate.

2.6.1 Region 1: Length of Elastic Zone with Asymptotic Displacement Decay

For a given end displacement, material properties and TSR, there will be a finite length over which the asymptotic solution will decay from a displacement of δ_0 to zero. We call this length L_1^*. The differential equation for this region is given by Eq. (2.4a). In this region, for an order of magnitude estimate, $w \sim \delta_0$ and $x \sim L_1^*$. Thus,

$$E^* I \frac{d^4 w_1}{dx^4} = -\frac{\sigma_0 b w_1}{\delta_0} \Rightarrow E^* I \frac{\delta_0}{L_1^{*4}} \sim \frac{\sigma_0 b \delta_0}{\delta_0}$$

$$L_1^* \sim \left[\frac{E^* I \delta_0}{\sigma_0 b} \right]^{1/4} \text{ or } \frac{L_1}{h} \sim \left[\frac{E^* \delta_0}{\sigma_0 h} \right]^{1/4}$$

(a)

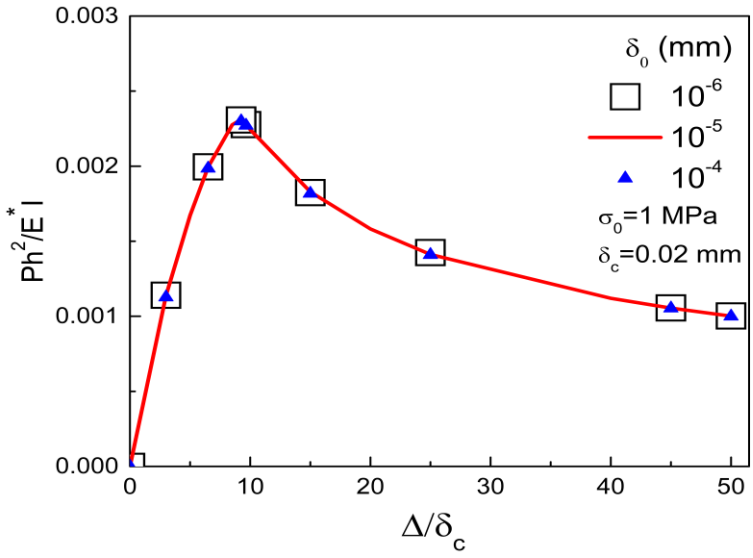

(b)

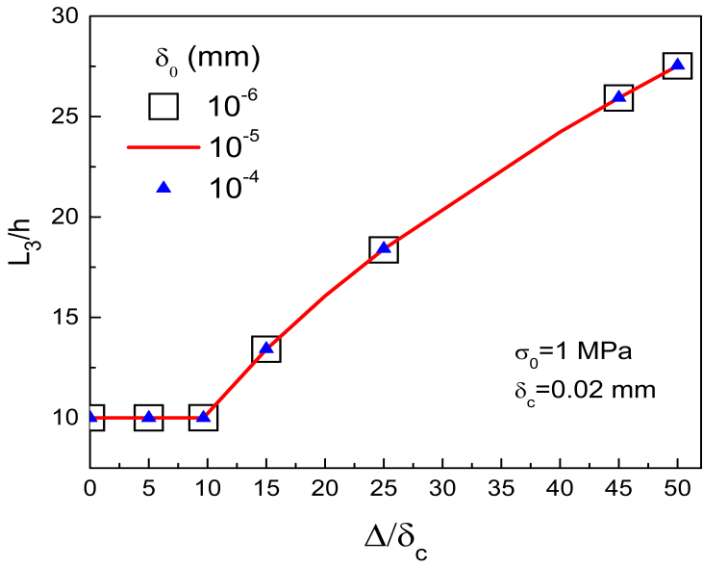

Figure 2.7: Effect of δ_0 on fracture load and crack length. Base case is plotted as a line and results for other δ_0 values were calculated for discrete points. (a) Load–displacement response as a function of δ_0, and (b) crack length as a function of δ_0.

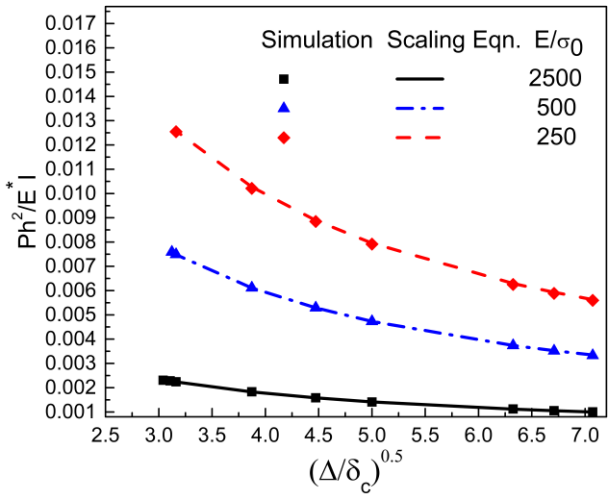

Figure 2.8: Load-displacement behavior as a function of interface strength.

The scaling equation for L_1^* is then

$$\frac{L_1^*}{h} = 4.56\Lambda^{1/4}\alpha_0^{1/4} \tag{2.10}$$

where the *O(1)* number is obtained from data fitting for $w_1 = 0.01\alpha_0$ i.e. when w_1 decays asymptotically to 1% of the normalized δ_0 value.

2.6.2 Region 2: Length of Damage Zone

The differential equation for this region is given by Eq. (2.4b). In this region, for an order of magnitude estimate, $w \sim \delta_c$ and $x \sim L_2$. Thus, for $\delta_0 << \delta_c$:

$$E^* I \frac{d^4 w}{dx^4} = \frac{\sigma_0 b w}{\delta_c} - \sigma_0 b \Rightarrow E^* I \frac{\delta_c - 0}{\left[L_1^* + L_2\right]^4} \sim \sigma_0 b$$

$$So,\ L_2 \sim \left[\frac{E^* I}{\sigma_0 b}\right]^{1/4} \left(\delta_c^{1/4} - \delta_0^{1/4}\right)\ or\ \frac{L_2}{h} \sim \left[\frac{E^* \Delta}{\sigma_0 h}\right]^{1/4} \left(\alpha_c^{1/4} - \alpha_0^{1/4}\right)$$

yielding the scaling equation for L_2 after data fitting as

$$\frac{L_2}{h} = 1.1\Lambda^{1/4}(\alpha_c^{1/4} - \alpha_0^{1/4}) \tag{2.11}$$

Equation (2.11) fits the results of the simulations very well, as can be seen in Fig. 2.9a.

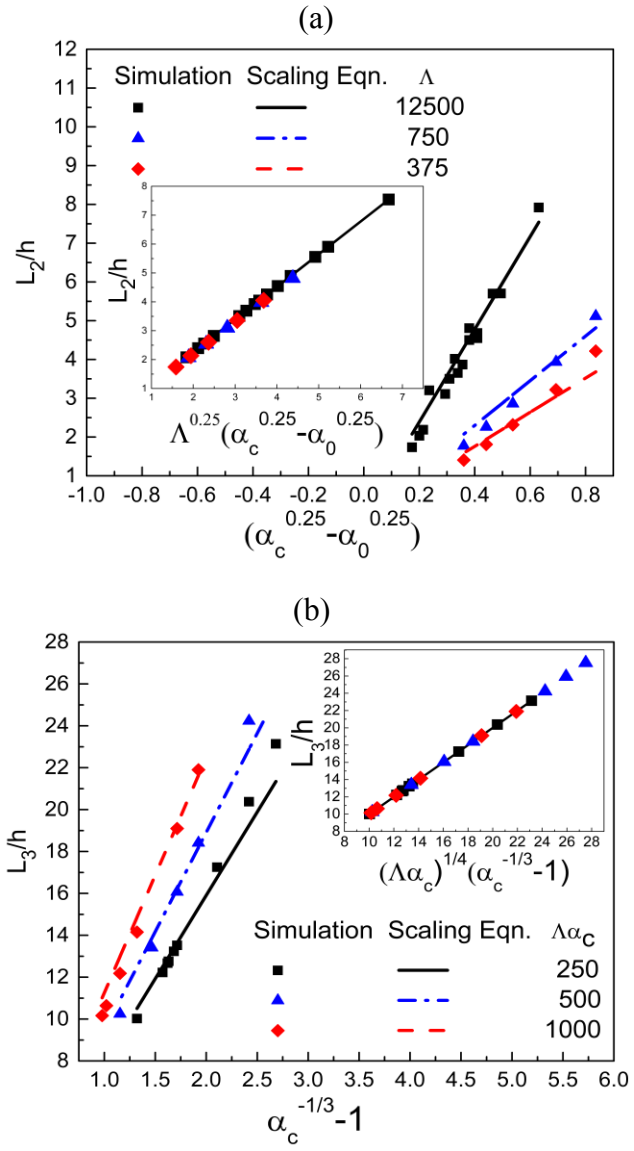

Figure 2.9: Effect of δ_c and Λ on fracture propagation. (a) Damage zone evolution as a function of δ_c and Λ, and (b) crack growth as a function of δ_c and Λ. Both insets with the legend same as the main figure show that results collapse onto a master curve.

2.6.3 Region 3: Crack Length and Load

The force balance for the cracked layer in region 3 dictates that the third derivative of displacement be a constant throughout the region. This implies:

$$E^* I \left.\frac{d^3 w}{dx^3}\right|_{x=L_1^*+L_2+L_3} = E^* I \left.\frac{d^3 w}{dx^3}\right|_{x=L_1^*+L_2}$$

$$\frac{\Delta}{\left[L_1^* + L_2 + L_3\right]^3} \sim \frac{\delta_c}{\left[L_1^* + L_2\right]^3}$$

$$L_3 \sim \left[\frac{E^* I \delta_c}{\sigma_0 b}\right]^{1/4} \left[\left(\frac{\Delta}{\delta_c}\right)^{1/3} - 1\right]$$

After fitting the data to find the constant of proportionality, we find

$$\frac{L_3}{h} = 2\left(\Lambda \alpha_c\right)^{1/4} \left[\alpha_c^{-1/3} - 1\right] \tag{2.12}$$

The comparison of Eq. (2.12) with simulation results is shown in Fig. 2.9b and the equation fits the simulation results very well.

To obtain scaling equation for steady state load during crack propagation, we use beam theory relations for fracture in absence of cohesive force [66] where *a* is the crack length of the beam in absence of cohesive interactions:

$$\Gamma_{ss} = -\frac{\Delta}{2b}\left(\frac{dP}{da}\right)_{\Delta}$$

$$\frac{P}{E^* I} = \left.\frac{d^3 w}{dx^3}\right|_{(x=a)} \sim \frac{\Delta}{a^3} \;\; and \;\; \Gamma_{ss} \sim \delta_c \sigma_0$$

$$So, \;\; \delta_c \sigma_0 \sim \frac{P^2}{b}\left(\frac{\Delta E^* I}{P}\right)^{2/3} \frac{1}{E^* I}$$

$$\frac{P}{E^* I} \sim \left(\frac{\sigma_0 b \delta_c}{E^* I}\right)^{3/4} \frac{1}{\Delta^{1/2}}$$

After data fitting, we find

$$\frac{P h^2}{EI} = 3.74\left(\frac{\sigma_0}{E^*}\right)^{3/4} \frac{\delta_c^{3/4}}{h^{1/4} \Delta^{1/2}} \tag{2.13}$$

Figure 2.8 shows excellent agreement between simulation results and the scaling equation (Eq. 2.13).

The largest applied displacement that was considered in developing the results for Fig. 2.8 was on the order of the beam thickness and was associated with a large amount of crack growth. This means that geometric nonlinearity did not play a large role here, as is commonly the case for most practical applications of the double cantilever beam configuration being considered here. Large deformations, along with material nonlinearity usually play a much larger role in peeling experiments, as noted in the recent analysis by Gialamas et al. [93].

2.7 CONCLUSIONS

In this paper the peeling mechanics of elastic thin films was modeled for the interaction between the film and the substrate using classical beam theory and cohesive zone models. The analytical model was validated using ABAQUS and experimental data. The model was used to study the dependence of load and crack length on film properties and TSR parameters. The load and crack length were found to be independent of δ_0 but they did depend on interface strength implying that interaction stiffness does play a role in crack propagation. Scaling analysis was performed to identify the exact dependence of crack growth on material properties and interface interactions. Three dimensionless groups (Λ, α_0 and α_c) were identified to quantify steady state load, crack length and damage zone length. Hence, the complexity of beam theory models was reduced to yield simple equations to determine crack growth.

In the next chapter, the beam theory model is developed further to include shear tractions at the interface. Transfer printing is an inherently mixed-mode fracture process which is why developing a single interface mixed-mode fracture model is an important step before simulating competing fracture in thin film transfer.

Chapter 3: A Cohesive Zone Model and Scaling Analysis for Mixed-Mode Interfacial Fracture[2]

A semi-analytical methodology is developed to study mixed-mode interface fracture that combines beam theory and cohesive zone interactions. The method is validated with predictions from a non-linear commercial finite element package and results in the literature. Compared to commercial finite element packages, the method is significantly faster (>1000X) and robustly converges. Scaling equations are extracted that predict load, crack length, damage zone length and mode-mix. These equations can be used to extract cohesive zone interactions from experimentally obtained load-displacement data.

3.1 INTRODUCTION

Bi-material interfaces are prevalent in multiple natural and engineering applications from adhesive joints and composites to thin film transfer and self-assembled monolayers (SAMs). To design such layered structures which can potentially fail due to interface cracking or to design a process requiring delamination, an understanding of mixed-mode interface fracture is of utmost importance.

Significant contributions to the understanding of bi-material cracks were made through analytical approaches using linear elastic fracture mechanics [95-100], experiments [101-103] and numerical simulations [104-107]. While many experimental investigations included an adhesive interlayer and found the critical energy release rate to be a function of the mode-mix, some experimental studies without an interlayer [108, 109] obtained a similar result. In the former, the toughening effect was attributed to

[2] Much of this chapter appeared in "A cohesive zone model and scaling analysis for mixed-mode interfacial fracture", Jain, S., Na, S.R., Liechti, K.M., Bonnecaze, R.T., 2017, Int J Solids Struct. 129, 167-176.

increased viscoplastic dissipation in the epoxy. Fiber bridging or asperity shielding [110] from interfacial roughness may have been the cause of toughening in the latter studies.

Recently, cohesive zone models (CZMs) have gained popularity for studying cracks to incorporate both toughness and strength parameters for the interfaces. The early approaches [70, 82] were extended to include elastic and softening interactions at the interface, and these models have been used extensively to study adhesion in double cantilever specimens and predominantly mode I fracture [83, 84, 86-88, 111]. In the case of adhesive interlayers, experimental [69, 75, 112], analytical and numerical [113, 114] works have been presented to characterize interfaces and develop scaling equations for pull-off force and cohesive zone size.

In this paper we consider interactions represented by mixed-mode traction-separation relations (TSRs), which capture interactions with chemical, molecular and electrostatic origins and can also embody the effects of surface roughness and moisture. Previous mixed-mode fracture studies with linear beam theories and CZMs [78, 91, 115] employed finite element techniques and developed equations for load as a function of physical parameters. An equation for phase angle for multiple configurations was developed with tabulated coefficients [76]. However, closed form solutions for crack length, damage zone length and mode-mix for a mixed-mode fracture configuration have not been previously reported. Here, we present a one-dimensional (1-D) model for mixed-mode peeling of a thin film from a rigid surface based on classical beam theory and bi-linear TSR. The equations are easily solved numerically and scaling analysis is used to derive algebraic equations to correlate load, fracture length, damage zone length and mode-mix with the mixed-mode fracture properties of the interface. The outline of the paper is as follows. Section 3.2 summarizes some of the most commonly used forms of bi-linear TSRs for mixed-mode fracture. The model is developed in section 3.3,

followed by numerical validation in section 3.4. The results of parametric analysis and scaling equations are presented in section 3.5.

3.2 COHESIVE ZONE MODELS

Cohesive zone models for interfaces have three main characteristics: the shape of the traction-separation relation (linear, bi-linear, trapezoidal, exponential, polynomial or multi-linear), the criterion for damage initiation and the criterion for failure of the interfaces. In the case of mixed-mode fracture, interface strengths, interaction ranges and fracture energies may be defined separately for both normal and tangential deformations along with a definition of mode-mix based on energies or tractions. The review of CZMs [116] provides a good summary of different models that have been used in fracture studies. This section briefly describes the bi-linear TSR and various criteria used for damage initiation and failure.

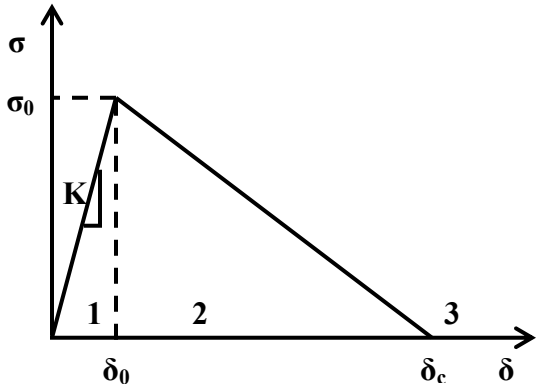

Figure 3.1: Schematic of a bi-linear traction-separation relation for an interface.

Consider an interface with traction σ, stiffness K, opening displacement δ and critical fracture energy release rate Γ_c. In the case of a bi-linear TSR (Fig. 2.1) for Mode I, the interface first deforms elastically (region 1). Interface damage begins (and continues in region 2) once a damage initiation condition is met ($\delta = \delta_0$ or $\sigma = \sigma_0$). The

interface is fractured (region 3) on satisfying the failure criterion ($\delta = \delta_c$ or $\Gamma = \Gamma_c$). Criteria for mixed-mode fracture are comparatively more complex and some of them are described below.

3.2.1 DAMAGE CRITERIA

The quadratic stress condition is based on the normal stress σ and shear stress τ at the interface, and damage being initiated when

$$\left(\frac{\sigma}{\sigma_0}\right)^2 + \left(\frac{\tau}{\tau_0}\right)^2 = 1 \ , \tag{3.1a}$$

where σ_0 and τ_0 are the normal and shear interface strengths. Studies which have used this condition include analysis for a moment-loaded double cantilever beam (MLDCB) specimen [117] and single leg bending (SLB) specimen [118].

The fracture energy based criterion for damage initiation is given by:

$$\frac{\Gamma_n}{\Gamma_{nc}} + \frac{\Gamma_t}{\Gamma_{tc}} > \eta, \tag{3.1b}$$

where η is a prescribed ratio less than unity, Γ_n and Γ_t are energy release rates in normal and shear directions, and Γ_{nc} and Γ_{tc} are the critical energy release rates in normal and shear directions. This condition was used for an MLDCB specimen [119].

For our present work, a displacement based criterion for damage initiation is used and is of the form

$$\delta = \sqrt{w^2 + u^2} = \delta_0, \tag{3.1c}$$

where w is the normal displacement and u is the shear displacement at the interface. This condition has the simplicity of requiring only one parameter i.e. the critical displacement δ_0. The stress and fracture energy based criteria in comparison require two or three parameters.

3.2.2 FAILURE CRITERION

The most popular failure criterion is based on fracture energy and is

$$\frac{\Gamma_n}{\Gamma_{nc}} + \frac{\Gamma_t}{\Gamma_{tc}} = 1. \tag{3.2a}$$

This condition has been successfully implemented in multiple studies [78, 91, 117-119].

Another popular criterion for failure and the one used in this paper is the condition based on the total displacement at the interface [112], namely

$$\delta = \sqrt{w^2 + u^2} = \delta_c, \tag{3.2b}$$

where δ_0 is the critical value for fracture at the interface. Of course at failure, the normal and shear stress vanish at the interface. For total displacements between δ_0 and δ_c, the stresses are assumed to be linearly dependent on the displacements and the damage parameter D ($0 \le D \le 1$) so that

$$\sigma = K_n(1-D)w \quad , \quad \tau = K_s(1-D)u \tag{3.3}$$

and

$$D = \frac{\delta_c(\delta - \delta_0)}{\delta(\delta_c - \delta_0)}. \tag{3.4}$$

Here it is assumed that the stiffness in the elastic region is the same for both normal and shear displacement, that is $K = K_n = K_s$.

In summary, we consider an interface with stiffness K in both normal and tangential directions, effective displacement δ_0 for damage initiation and effective displacement δ_c for damage completion. With these three parameters, for a bilinear TSR, the fracture energy is given by $K\delta_0\delta_c / 2$ and the total adhesion strength σ_T is $K\delta_0$. The

stresses in each region can be expressed as

$$\sigma = \begin{cases} Kw & , \text{ region 1} \\ K(1-D)w, & \text{region 2} \\ 0 & , \text{ region 3} \end{cases} , \quad \tau = \begin{cases} Ku & , \text{ region 1} \\ K(1-D)u, & \text{region 2} \\ 0 & , \text{ region 3} \end{cases} . \tag{3.5a}$$

This model is equivalent to the interface behaving like a non-linear (in this case, bi-linear) spring where

$$\bar{\sigma} = K(1-D)\delta \quad , \quad \sigma = \frac{w}{\delta}\bar{\sigma} \quad , \quad \tau = \frac{u}{\delta}\bar{\sigma}, \tag{3.5b}$$

where $\bar{\sigma}$ is the magnitude of the summed normal and shear stress vectors. The CZM formulation used in this study has the advantage of only requiring three parameters. Further, no prior knowledge of mode-mix is needed. The local mode-mix at any location can be determined as part of the solution using the following equation:

$$\tan\Psi = \left(\frac{u}{w}\right) . \tag{3.6}$$

The following section details the differential equations, boundary conditions and method used for simulating mixed-mode peeling.

3.3 MIXED-MODE PEELING MODEL

Consider a thin film or beam of width b, length L and thickness h adhered to a rigid substrate as shown in Fig. 3.2(a). There is an initial crack of length $l_0 >> 10h$ at the interface and the top layer is displaced at one end by Δ.

The thickness of the film or beam and its deflection are such that beam theory can be used to describe the elastic forces. The normal deflection of the beam w with elastic modulus E, Poisson's ratio v and moment of inertia I is obtained using the free body diagram in Fig. 3.2(b) and given by

(a)

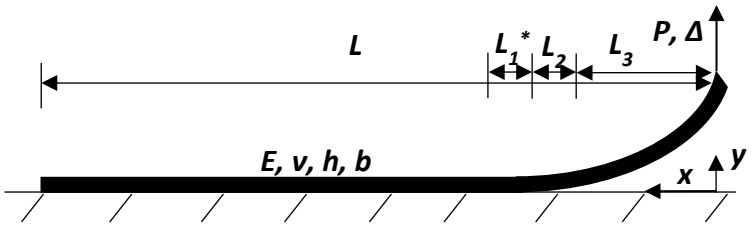

(b)

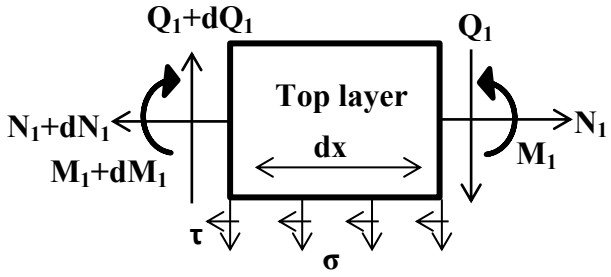

Figure 3.2: (a) Schematic of peeling from a rigid substrate under fixed displacement; (b) free body diagram of an element of the top layer.

$$E^* I \frac{d^4 w}{dx^4} - \frac{bh}{2}\frac{d\tau(x)}{dx} + b\sigma(x) = 0, \tag{3.7}$$

where the shear displacement at the bottom surface of the thin film $u = \frac{h}{2}\frac{dw}{dx}$ and $E^* = E/(1-\nu^2)$ in case of plane strain. The cohesive zone interactions are accounted for in the terms $\sigma(x)$ and $\tau(x)$ which are the normal and shear stress acting on the beam due to the interface. We consider an elastic region of length L_1^*, damage region of length L_2 and crack length $L_3 \geq l_0$. Substituting the equation for tractions from equation (3.5a) into equation (3.7), we have the following three differential equations for each region:

$$E^* I \frac{d^4 w_3}{dx^4} = 0 \qquad 0 \leq x \leq L_3 \tag{3.8a}$$

$$E^* I \frac{d^4 w_2}{dx^4} + bK(1-D)w_2 - \frac{bh}{2}\frac{d}{dx}\left(K(1-D)\frac{h}{2}\frac{dw_2}{dx}\right) = 0 \qquad L_3 \leq x \leq L_2 + L_3 \tag{3.8b}$$

$$E^* I \frac{d^4 w_1}{dx^4} + bKw_1 - \frac{bh}{2}\frac{d}{dx}\left(K\frac{h}{2}\frac{dw_1}{dx}\right) = 0 \qquad L_2 + L_3 \le x \le L_1^* + L_2 + L_3 \qquad (3.8c)$$

Equation (3.8c) for the elastic response in region 1 has the following general solution:

$$\frac{w_1}{\Delta} = A\exp(-\frac{\alpha x}{\sqrt{2}h}) + B\exp(-\frac{\beta x}{\sqrt{2}h}) \qquad (3.9)$$

where $\alpha = \sqrt{\frac{3Kh}{E^*} - \sqrt{\left(\frac{3Kh}{E^*}\right)^2 - \frac{48Kh}{E^*}}}$ and $\beta = \sqrt{\sqrt{\left(\frac{3Kh}{E^*}\right)^2 - \frac{48Kh}{E^*}} + \frac{3Kh}{E^*}}$ and A and B are constants of integration.

From this asymptotic solution, an estimate of the length over which the effective displacement decays L_1^* is set by the location where $w_1 = 0.01\delta_0$. Knowing the solution in region 1, we obtain boundary conditions (3.10a-b) for the elastic-damage boundary and solve the equations for only regions 2 and 3 with a shooting method because boundary locations depend on L_2 and L_3 which are not fixed. Note that $Kh/E^* > 16/3$ is required for real values of exponential coefficients in region 1 (equation 3.9). For $Kh/E^* > 16/3$, displacement in region 1 will have imaginary exponential coefficients and equations 3.10a-b will never be satisfied. Based on continuity of displacements, rotation, moments and forces, the boundary conditions for the system of differential equations are:

$$\frac{(\alpha+\beta)h^2}{\sqrt{2}}\frac{d^2 w_2}{dx^2} + h^3\frac{d^3 w_2}{dx^3} + \frac{\alpha\beta h}{2}\frac{dw_2}{dx} = 0 \qquad : x = L_2 + L_3 \qquad (3.10a)$$

$$-h^3\frac{d^3 w_2}{dx^3} - \frac{\alpha h^2}{\sqrt{2}}\frac{d^2 w_2}{dx^2} + \frac{\beta^2 h}{2}\frac{dw_2}{dx} + \frac{\alpha\beta^2 w_2}{2\sqrt{2}} = 0 \qquad : x = L_2 + L_3 \qquad (3.10b)$$

$$w_2 = w_3, \quad \frac{dw_2}{dx} = \frac{dw_3}{dx}, \quad \frac{d^2 w_2}{dx^2} = \frac{d^2 w_3}{dx^2}, \quad \frac{d^3 w_2}{dx^3} = \frac{d^3 w_3}{dx^3} \quad : x = L_3 \qquad (3.10c\text{-}f)$$

$$w_3 = \Delta, \quad \frac{d^2 w_3}{dx^2} = 0 \qquad : x = 0 \qquad (3.10g\text{-}h)$$

and boundaries are defined at steady state by the equations:

$$\delta = \sqrt{w_2^2 + u_2^2} = \delta_0 \quad : x = L_2 + L_3, \qquad \delta = \sqrt{w_2^2 + u_2^2} = \delta_c \quad : x = L_3 \quad \text{(3.10i-j)}$$

While the damage zone is growing towards its steady state value, equation (3.10j) is not required since the boundary is known to be at $x = l_0$.

The equations are solved using a shooting method with MATLAB®. A guess is made for dw_3/dx and d^3w_3/dx^3 at $x = 0$ to solve equation (3.8a) for the cracked region followed by the damaged region equation (3.8b) and guesses are updated based on equations (3.10a-b) for convergence.

3.4 NUMERICAL VALIDATION

The 1-D model is validated by comparing the solutions with those from a full 2-D finite element ABAQUS 6.14® simulation in the next section. As a base problem, we consider the peeling of the thin film from a rigid surface where realistic values are chosen for the mixed-mode TSR based on the experimental results of Wu et al. [112]. The top film is silicon with E^*=165,500 MPa, h=0.6 mm, b=5 mm, L=45 mm, l_0=12 mm, K =1,600,000 MPa/mm, δ_c=0.721 μm, δ_0 =0.052 μm and Δ=0.26 mm. The displacement of the film, stresses at the interface and load-displacement curve are extracted from FEM simulations in ABAQUS® with 4-node bilinear plane strain quadrilateral elements with reduced integration for the substrates with a square mesh size of 0.2 mm for the bottom substrate, a finer mesh for the top layer and surface based cohesive behavior.

Comparisons for normal and shear displacements of the thin film are shown in Fig. 3.3. Excellent agreement is seen in both cases. Normal and shear stresses at the interface are compared in Fig. 3.4 where the position of the crack tip matched within 0.09% and the damage zone length matched within 7% but the peak values are very different. We attribute this difference to our use of asymptotic boundary conditions rather than solving the elastic region whereas ABAQUS® solves for displacements along the entire length of the beam. At damage initiation, this led to local mode-mix values of -51°

and -74° in the finite element and beam analyses, respectively. In addition, the limited number of options for damage initiation criteria in ABAQUS® did not include the one selected for the beam analysis. The one selected for the finite element analysis was the closest possible one, but the traction values for damage initiation did differ by the amounts shown in Fig. 3.4, pointing to the internal consistency of each analysis.

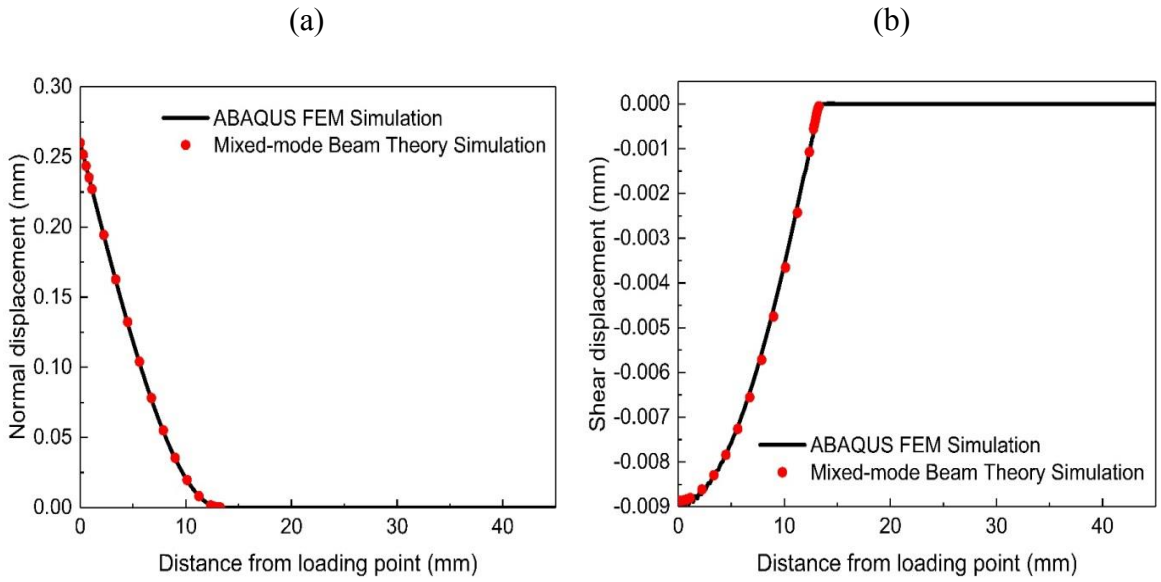

Figure 3.3: Results for FEM simulations and beam theory model- (a) Comparison of normal displacements along the beam, and (b) comparison of shear displacement along the beam.

The comparison for load-displacement values is shown in Fig. 3.5 and the results are in close agreement. These comparisons validate our beam theory model. Note that the 1-D finite difference shooting method takes a few seconds to produce a converged solution whereas commercial software can take hours to solve a cohesive zone interface fracture problem and requires considerable troubleshooting for convergence. These advantages show the importance of having a simpler semi-analytical framework to model interface fracture.

(a)

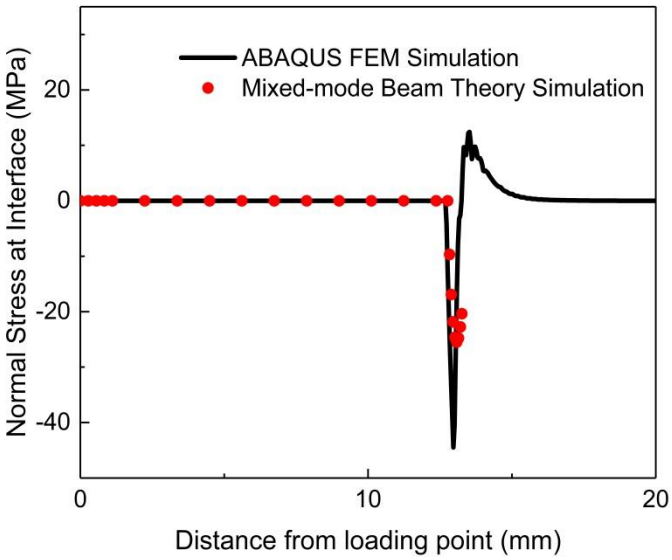

(b)

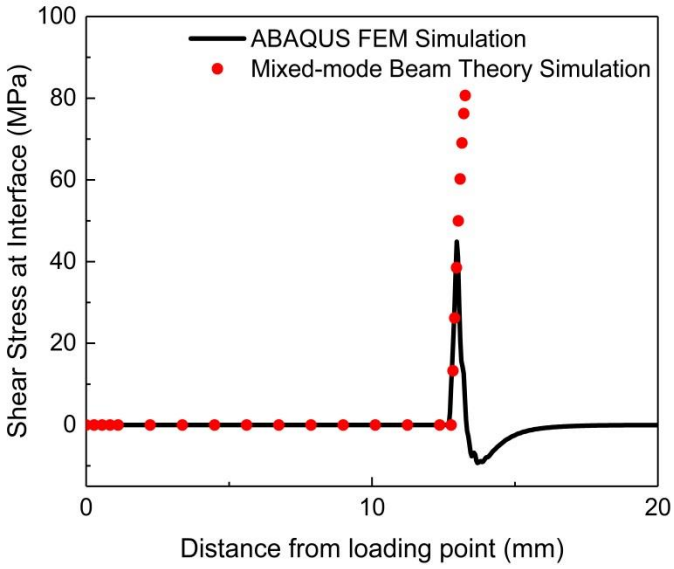

Figure 3.4: Results for FEM simulations and beam theory model- (a) Comparison of normal stresses at the interface, and (b) comparison of shear stresses at the interface.

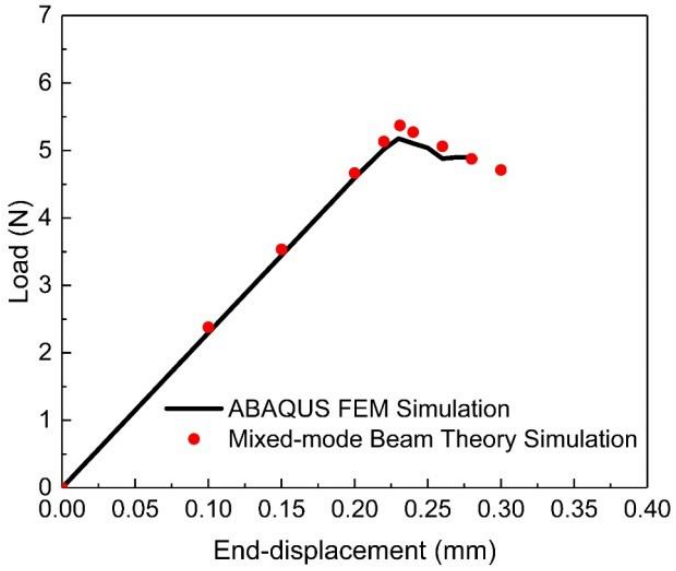

Figure 3.5: FEM and beam theory results for the load-displacement curve.

3.5 Results and Discussion

Parametric analysis is performed to study the influence of different material properties, layer thickness and TSR parameters on the resultant load P, damage zone length L_2, crack length L_3 and mode-mix among others. Scaling equations are obtained to determine the exact dependence of parameters on fracture. The base case is presented first in this section, followed by results of parametric analysis.

3.5.1 Base Case

We consider a base case of a silicon layer with simulation parameters mentioned in Table 3.1.

Table 3.1: Material properties, geometry and TSR parameters for the base case.

E^* (MPa)	L (mm)	b (mm)	h (mm)	l_0 (mm)	K (MPa/mm)	δ_c (μm)	δ_0 (μm)	Δ (mm)	Γ_c (J/m^2)
165,500	45	5	0.6	12	1,480,000	0.721	0.052	0.3	27.74

Fig. 3.6 (a) shows the load –displacement curve and Fig. 3.6 (b) shows the length of the crack for increasing displacement. The load increases linearly with displacement until steady state crack growth begins and then decreases as the crack grows. Crack length does not grow from its initial value of l_0 until the onset of steady state crack growth. Fig. 3.7 (a-b) illustrates the development of the damage zone and the energy release rate in the damage zone at steady state. It can be seen that the damage zone length remains fairly constant during steady state crack growth and so does the energy release rate. The mode-mix at the crack tip as a function of end displacement is shown in Fig. 3.8(a). It maintains a value of approximately -50.2^0 which falls in the range of mode-mix angles reported for interface cracks in a bilayer[120]. All of these trends are consistent with characteristics of crack growth and support the applicability of our effective displacement - based cohesive zone model for mixed-mode fracture.

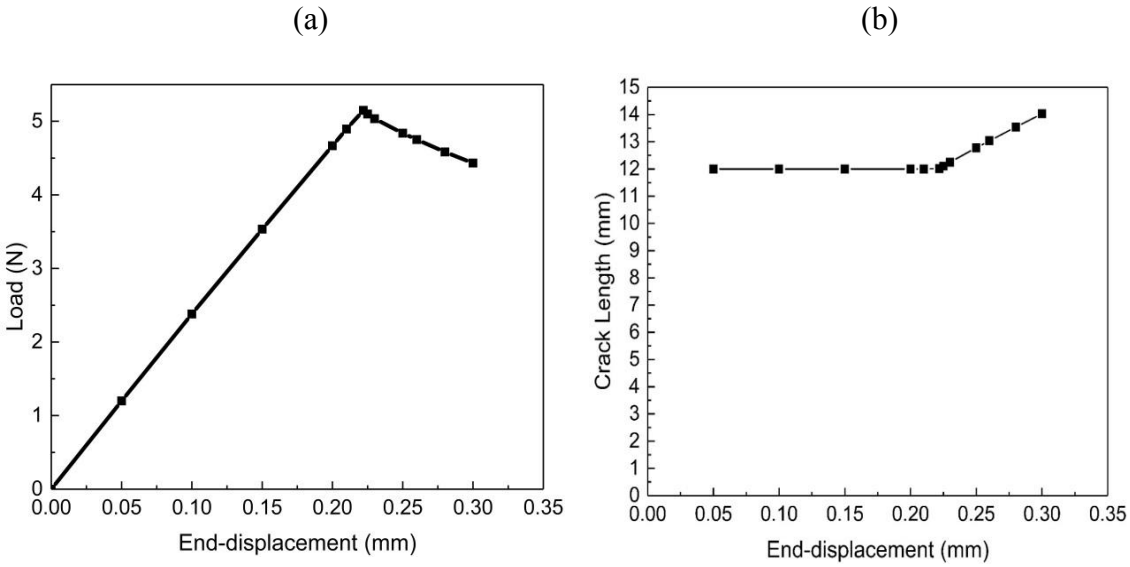

Figure 3.6: (a) Load-displacement curve for the base case; (b) crack length as a function of end displacement.

(a)

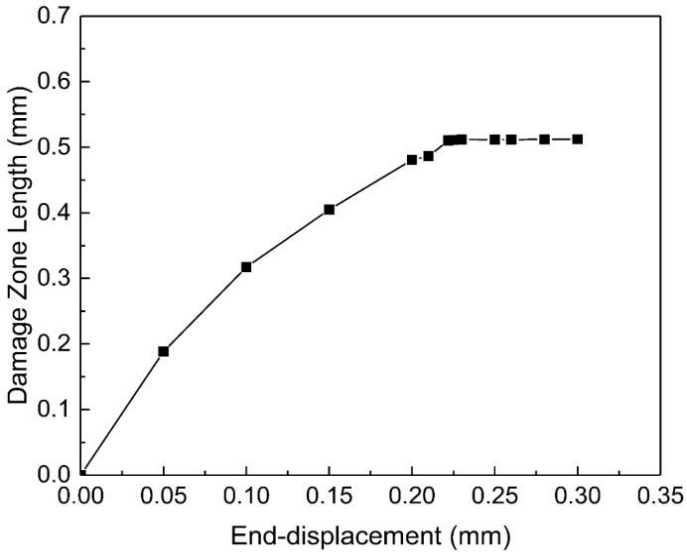

(b)

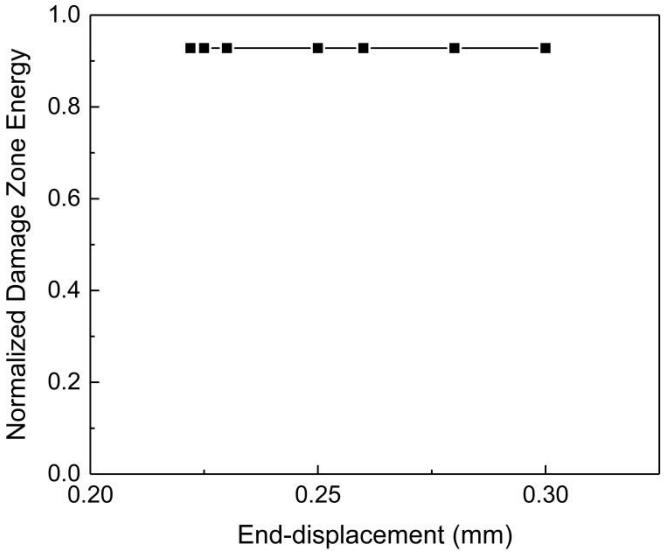

Figure 3.7: (a) Damage zone length as a function of displacement; (b) energy release rate in the damage zone normalized by the fracture toughness at steady state.

Interface stresses are extracted from simulation results and compared with the input bilinear TSR as shown in Fig. 3.8(b), where displacements are normalized by the maximum displacement in respective directions. The input and output TSRs match perfectly, and shear stresses contribute the most to interface stresses. At the damage initiation point where the effective stress peaks at $K\delta_0$, shear stress is at its maximum value but normal stresses continue to increase initially during shear softening. Variations in TSR parameters and layer thickness change this behavior and it is discussed later on in section 3.5.2.6.

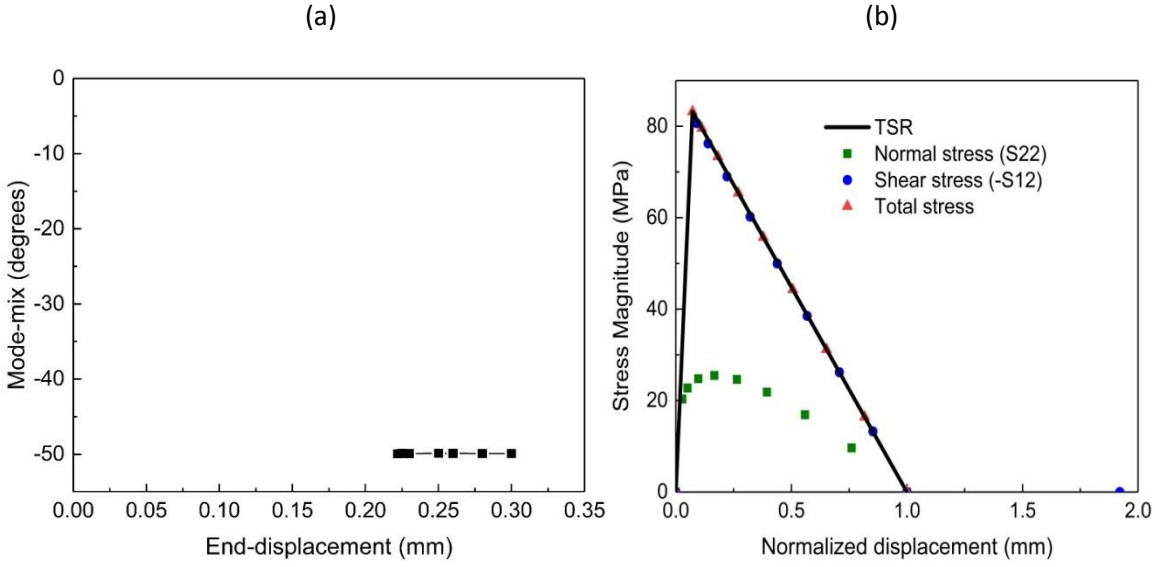

Figure 3.8: (a) Mode-mix as a function of displacement during stead-state crack growth; (b) Comparison of input and output TSR.

3.5.2 Parametric Analysis

For parametric analysis of steady state crack growth, E^* was varied from 120,000 - 165,500 MPa, h was varied from 0.6 - 1.1 mm, K was varied from 1,480,000 - 2,700,000 MPa/mm, δ_c was varied from 0.5 - 1.2 μm, δ_0 was varied from 0.035 - 0.09 μm and Δ was varied from 0.22 - 0.3 mm. Note that the window where $Kh/E^* > 16/3$ and cracks

grow in steady state sets the bounds on the parameter space for this analysis. Next we discuss parametric analysis and scaling arguments to predict load, crack length, damage zone length and mode-mix for steady state crack growth.

3.5.2.1 Load

Results show that the load required to peel the layer increases with increase in K, E^*, δ_c, δ_0 and h but decreases with Δ. We use the beam theory relationship for fracture in absence of cohesive forces [66]:

$$\Gamma_c = -\frac{\Delta}{2b}\left(\frac{dP}{dL_3}\right)_\Delta , \tag{3.11}$$

and in the cracked region of length L_3 where w increases from δ_c to Δ, we can approximate the third derivative to find that $\frac{P}{E^* I} = \frac{d^3 w}{dx^3}\Big|_{x=0} \sim \frac{\Delta - \delta_c}{L_3^3}$,

which means $L_3 \sim \left[(\Delta - \delta_c) E^* I / P\right]^{1/3}$.

For a bi-linear TSR where $\Gamma_c = K\delta_0\delta_c / 2$ or simply $\Gamma_c \sim K\delta_0\delta_c$, which is substituted into Eq. (11) along with scaling relationship for L_3, it is found that

$$K\delta_0\delta_c \sim \frac{\Delta E^* h^3 (\Delta - \delta_c)}{\left(\frac{(\Delta - \delta_c) E^* I}{P}\right)^{4/3}} \tag{3.12}$$

and on rearrangement yields $P \sim O(1)(K\delta_0\delta_c h)^{3/4} b \frac{E^{*1/4}(\Delta - \delta_c)^{1/4}}{\Delta^{3/4}}$. After data fitting, we find that:

$$P = 0.31(K\delta_0\delta_c h)^{3/4} b \frac{E^{*1/4}(\Delta - \delta_c)^{1/4}}{\Delta^{3/4}} \tag{3.13a}$$

which simplifies in cases of long initial cracks (or $\Delta >> \delta_c$) to:

$$P = 0.31(K\delta_0\delta_c h)^{3/4} b E^{*1/4} / \Delta^{1/2} . \tag{3.13b}$$

It can be seen in Fig. 3.9 that simulation results from the parametric analysis agree well with the scaling equation. The values in the legend represent the range of variation for each parameter with units being the same as in Table 3.1. For example, when h is varied between 0.6 mm to 1.1 mm, other parameters are kept constant at the values mentioned in Table 3.1. It should be noted that Eq. (3.13b) for mixed-mode peeling has the same parametric dependence as load for a DCB configuration obtained in our previous work [111] but the fracture energy in mixed-mode is the total fracture energy including contributions from both normal and shear stresses. The equation for the load for the DCB configuration is clearly very similar to that presented here in Eq. (3.13b). In the dimensionless form, Eq. (3.13b) can be written as -

$$\frac{P}{E^* h} = 0.31\left(\frac{K\delta_0\delta_c}{E^* h}\right)^{3/4}\left(\frac{h}{\Delta}\right)^{1/2}. \tag{3.13c}$$

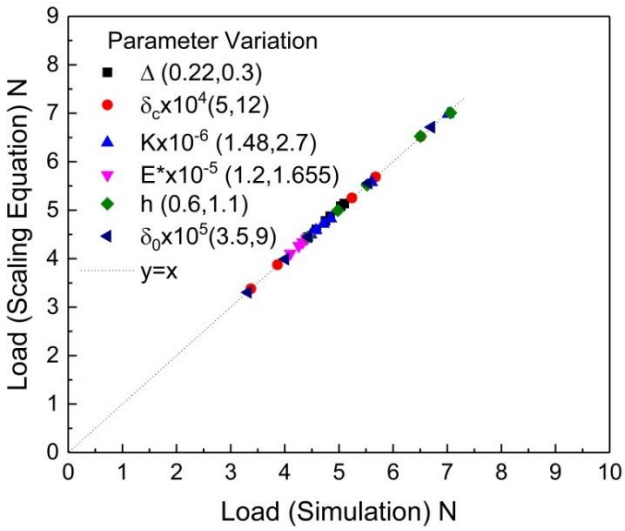

Figure 3.9: Parametric analysis for load and comparison with scaling equation. Parenthetical values are the range of the parameters explored for the simulations.

3.5.2.2 Crack Length

In region 3, we know that load is proportional to the third derivative and we can use a scaling argument for the derivative to obtain an equation for crack length- $\frac{P}{E^* I} = \frac{d^3 w}{dx^3}\Big|_{x=0} \sim \frac{\Delta - \delta_c}{L_3^3}$ and on substituting equation (13a) for P, we get:

$$L_3 = 0.9\left[\frac{E^* h^3}{K\delta_0\delta_c}\right]^{1/4} \Delta^{1/4}(\Delta - \delta_c)^{1/4} \tag{3.14a}$$

which can be written in a dimensionless form as:

$$\frac{L_3}{h} = 0.9\left[\frac{E^* h}{K\delta_0\delta_c}\right]^{1/4} \left(\frac{\Delta}{h}\right)^{1/4} \left(\frac{\Delta - \delta_c}{h}\right)^{1/4}. \tag{3.14b}$$

Fig. 3.10(a) compares the parametric analysis results from simulations to results from the scaling equation (3.14a) and excellent agreement is observed.

(a) (b)

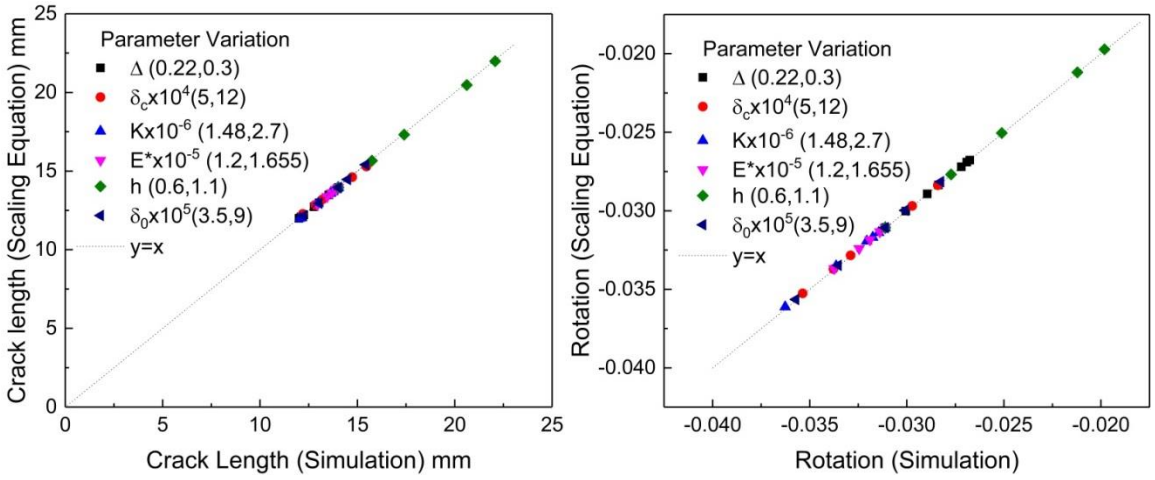

Figure 3.10: (a) Parametric analysis for crack length L_3 and comparison with scaling equation; (b) comparison of rotation at the loading point as obtained from simulations versus scaling equation results.

The critical end displacement Δ_c at which the damage zone is fully developed and steady -state crack growth will begin can be calculated by solving Eq. (3.14a) for $L_3 = l_0$. For $\Delta >> \delta_c$, Δ_c is given by

$$\Delta_c = 1.23\left[\frac{K\delta_0\delta_c}{E^* h^3}\right]^{1/2} l_0^2 \tag{3.15}$$

3.5.2.3 Rotation at Loading Point

The shooting method in this study relies on two guesses at the loading point - dw/dx and d^3w/dx^3. A good guess for the latter can be estimated from Eq. (3.13a) and for the former, we use another scaling argument to estimate

$$\left.\frac{dw}{dx}\right|_{x=0} \sim \frac{\Delta - \delta_c}{L_3}.$$

Using Eq. (3.14a), we find

$$\left.\frac{dw}{dx}\right|_{x=0} = 1.61\left(\frac{K\delta_0\delta_c}{E^*}\right)^{1/4} \frac{(\Delta-\delta_c)^{3/4}}{\Delta^{1/4}h^{3/4}} \sim 1.61\left(\frac{K\delta_0\delta_c}{E^* h}\right)^{1/4}\left(\frac{\Delta}{h}\right)^{1/2} \quad (\text{for } \Delta >> \delta_c). \tag{3.16}$$

A parity plot comparing the values from simulation with the scaling equation is shown in Fig. 3.10(b) and excellent agreement between the two can be seen.

3.5.2.4 Damage Zone Length

Two possible scaling arguments can be made for the length of the damage zone based on the requirement that

$$\left.\frac{d^3w}{dx^3}\right|_{x=0} = \left.\frac{d^3w}{dx^3}\right|_{x=L_3}.$$

Thus, it is expected that $\frac{\Delta-\delta_c}{L_3^3} \sim \frac{\delta_c-\delta_0}{L_2^3}$ *or* $\frac{\Delta-\delta_c}{L_3^3} \sim \frac{\Delta-\delta_0}{(L_3+L_2)^3}$.

However, these resulting scaling equations do not yield results in agreement with simulations. This is because the normal displacements can vary significantly from the vectorial critical displacements. Instead the empirical equation

$$L_2 = 0.4\left(\frac{\delta_c}{\delta_0}\right)^{1/2}\left(\frac{E^*}{K}\right)^{1/3} h^{2/3} \tag{3.17}$$

for the length of the damage zone is determined based on dimensional analysis and data fitting. Fig. 3.11 shows the comparison between simulations and this empirical equation.

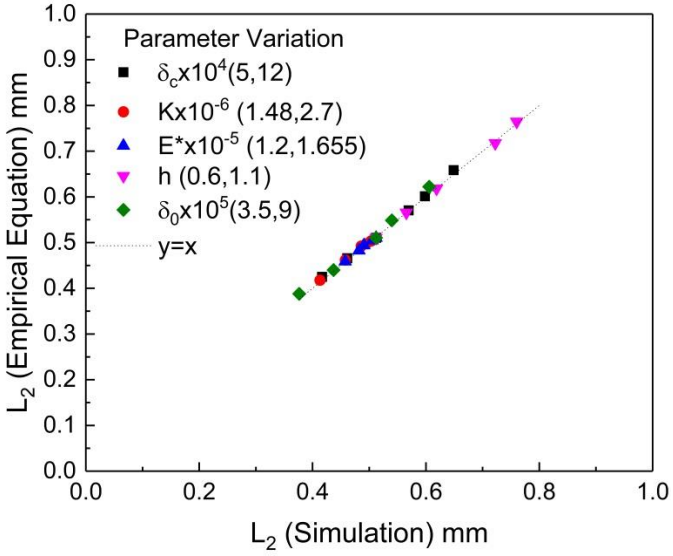

Figure 3.11: Comparison of simulations with empirically fitted Eq. 3.17 for the length of the damage zone length L_2.

CZM analysis with only normal stresses for the peeling process [88] considered a characteristic damage length $\bar{l}$ and the damage zone length was simply a function of this characteristic length:

$$L_2 \sim f(h,\bar{l}) \text{ where } \bar{l} = \frac{2}{3}\left(\frac{E\Gamma_c}{\bar{\sigma}^2}\right) = \frac{2}{3}\left(\frac{E\delta_c}{K\delta_0}\right) \tag{3.18a}$$

and bi-linear TSR scaling analysis for mode I [111] yielded:

$$L_2 = 1.1\left(\frac{E^* h^3(\delta_c - \delta_0)}{K\delta_0}\right)^{1/4}. \tag{3.18b}$$

Our consideration of shear at the interface gives similar parametric dependence as mode I (equations 3.18a-b) but different power law dependences on TSR parameters.

Equation (3.17) suggests that materials with higher elastic moduli and thicknesses will have longer damage zones and so will interfaces with lower strength.

3.5.2.5 Energy Release Rate in the Damage Zone

Clearly, the damage zone energy for a bilinear TSR is given by $\Gamma_d = K\delta_0(\delta_c - \delta_0)/2$ but it can also be estimated from simulations by calculating the J-integral over the vectorial TSR $\overline{\sigma}(\delta)$ as $\Gamma_d = \int_{\delta_0}^{\delta_c} \overline{\sigma} d\delta$. The energies calculated from these two methods are compared as another validation method for our CZM framework and excellent agreement is seen in Fig. 3.12(a).

3.5.2.6 Mode-mix at Crack Tip and Softening at the Damage Initiation Point

For same interface stiffness in both normal and tangential directions, we define mode-mix from the ratio of shear and normal displacements (Eq. 3.6) at the crack tip, so that

$$\tan\Psi_c = \left(\frac{u_c}{w_c}\right). \tag{3.19}$$

In the absence of a simple differential equation in the damage zone, we empirically obtain the following dependence of mode-mix on various parameters

$$\tan\Psi_c = -2.7\left(\frac{K\delta_0}{E^*}\right)^{0.37}\left(\frac{h}{\delta_c}\right)^{0.3}. \tag{3.20}$$

Equation (3.20) suggests a higher mode-mix for thicker layers with low elastic moduli and interfaces with high effective strengths and lower interaction ranges. The larger the difference between the separation at damage initiation and the critical separation for failure in the system, the closer it is to predominantly mode I crack growth. Since there is a lower bound of 16/3 on the combination Kh/E^*, the two separation parameters will have to differ by three to four orders of magnitude to have a mode-mix

under 20^0. The parity plot comparing simulation results with empirical equation is shown in Fig. 3.12(b). For the peeling configuration considered here, the resulting mode-mix is always higher than -45^0 indicating significant contributions from shear at the crack tip.

(a)

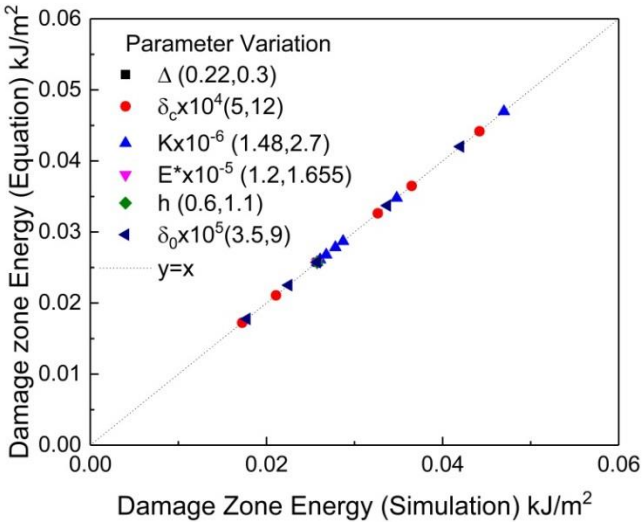

(b)

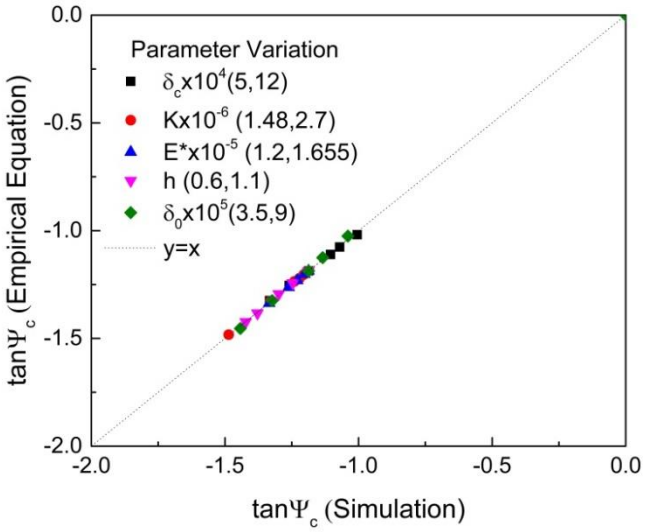

Figure 3.12: (a) Comparison of damage zone energy release rates obtained from simulations and equation for bilinear TSR; (b) Comparison of mode-mix in simulations with results from the empirical equation.

One limitation of mixed-mode CZMs is that they can provide positive stiffness during softening which is undesirable unless the material demonstrates stiffening behavior (Park and Paulino 2013). In these simulations, we observe that certain parameter values result in positive stiffness in either the normal or tangential direction during damage. Fig. 3.13 compares the stress at damage initiation to the peak stress attained during damage. While the shear stress at initiation was equal to the peak shear stress for thin layers irrespective of TSR parameters, the normal stress at initiation was equal to the maximum normal stress only for low values of δ_c, low values of δ_0 and thick layers. This parametric dependence could guide the characterization of an interface based on its stiffening behavior during damage.

(a) (b)

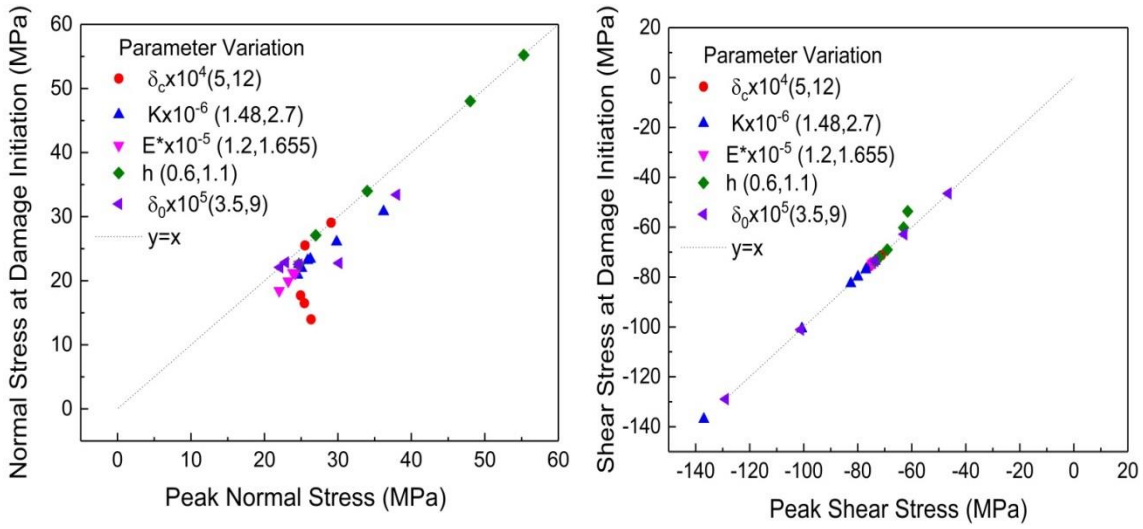

Figure 3.13: (a) Comparison of normal stress at damage initiation versus peak normal stress during damage; (b) comparison of shear stress at damage initiation versus peak shear stress during damage.

3.5.2.7 Length of Elastic Region

It can be seen from Eq. (3.8c) and Eq. (3.9) that scaling analysis is not straightforward because of multiple terms of similar orders of magnitude. An estimate of the length of the elastic region is obtained from the asymptotic solution (Eq. 3.9) by using derivatives at the boundary of region 1 and 2 from the shooting method solution to find the unknown constants *A* and *B*, and then estimating the length at which effective displacement reduces to 0.01 δ_0. Results indicate the following dependence:

$$L_1^* \sim \left(\frac{E^* \delta_c}{K} \right)^{1/4} f(h, \delta_0) \ . \tag{3.21}$$

$f(h, \delta_0)$ could not be estimated by empirical power law fitting because there was a non-monotonous change in L_1^* with variation in h and δ_0. From equation (3.9), we can infer that the characteristic dimensionless length would be a function of. E^* / Kh. In comparison, for a triangular TSR without any damage region and considering shear deformations in the beam but only normal damage at the interface, the following equation was derived [88]:

$$L_1^* \sim \left(\frac{E \delta_c}{K \delta_0} \right)^{1/4} h^{3/4} \tag{3.22}$$

with $\delta_c = \delta_0$ in the absence of a damage zone. Equations (3.21) and (3.22) have exactly the same dependence on E, K and δ_c. Clearly, the elastic zone region increases for materials with higher elastic modulus and interfaces with lower stiffness.

In the entire analysis presented in this section, two most prominent dimensional groups in the scaling equations are E^* / σ_T and $E^* h / \Gamma$ reinforcing the importance of effective interface strength and fracture energy in crack growth.

3.6 CONCLUSIONS

A three-parameter and bilinear mixed-mode TSR is proposed with K, δ_0 and δ_c as the effective stiffness, effective separation at initiation and separation at fracture, respectively. A shooting method formulation is used with a 1-D classical beam model and the asymptotic solution for the elastic region to study mixed-mode interactions during fracture. Interface strength, mode-mix and energy release rate are extracted as results of the simulation. The observed trends for steady-state crack growth are in agreement with established characteristics of CZM based fracture models. The model is also validated using the commerical finite element package ABAQUS®. Algebraic equations for steady state crack growth are extracted from the 1-D model for load, crack length, critical displacement, rotation at load point, damage zone length and mode-mix to clearly identify their parametric dependence on material properties and interface properties. The equations show that the two most important parameters in this mixed-mode TSR are the strength $\sigma_T = K\delta_0$ and effective separation at fracture δ_c. Values of K and δ_c individually may only affect the elastic zone length and the damage zone length. Another important aspect is that scaling equations for mode I and mixed-mode fracture have similar form when using a simple vectorial TSR analogous to a mode I bi-linear TSR.

In the next chapter, the graphene transfer process is modelled by extending the mixed-mode beam theory model discussed here. Finite element simulations and beam theory results give an insight into the important parameters impacting the success of graphene transfer.

Chapter 4: A Parametric Cohesive Zone Beam Theory Analysis of Mixed-mode Graphene Transfer

Competing interface fracture paths in the transfer of 2D materials from their growth substrate to a flexible polymer substrate are examined by developing finite element and semi-analytical beam theory models. With limited data on interface characterization for 2D materials, a parameter space is chosen based on the polyimide-graphene-copper foil system. Cohesive zone models with two different damage initiation criteria are explored. Algebraic equations to predict load, crack length, damage zone length, rotation and mode-mix are extracted through scaling analysis and correlation of the numerical data. Successful transfer of graphene to a polymer substrate is observed to be dependent on relative interface strengths rather than fracture energies.

4.1 INTRODUCTION

Two-dimensional (2D) materials, like graphene and MoS_2, have interesting mechanical and electrical properties with potential applications for next generation flexible electronics [121, 122]. Device fabrication with these materials requires an exfoliation step to transfer them from their growth substrate to the target substrate without damaging the layer or leaving undesired residues on the surface [20]. Use of elastomeric stamps like polydimethylsiloxane (PDMS), polyimide (PI) and polystyrene (PS) for exfoliation or dry transfer of graphene is gaining popularity due to clean transfer without use of any etchants or solvents and allowing reuse of copper foils [34, 36, 37, 39, 123] (Fig. 1a). Understanding the parametric relations that control the adhesion properties and quantifying the effect of competing interface interactions in this technique can improve processes for transfer printing of graphene and other 2D materials.

Crack propagation at interfaces has been studied for a single bi-material interface extensively through analytical approaches [95-100], experiments [101-103] and numerical simulations [104-107]. Recently, cohesive zone models [70, 82] have gained popularity for studying cracks to incorporate both toughness and strength parameters for interfaces [83, 84, 86, 88, 111, 124]. For bi-material interfaces with non-zero Dundurs (β) parameter, a combination of strength and toughness provides a cohesive length scale for an appropriate crack tip phase angle and allows for the analysis of mixed-mode fracture. Mixed-mode fracture studies with beam theories and cohesive zone models [78, 91, 115, 125] employed finite element and analytical techniques to develop equations for crack propagation as a function of physical parameters. For a cohesive length scale greater than 0.4, predictions from linear elastic fracture mechanics for fracture load were found to be significantly different from the results from numerical simulations [78].

Here, we model transfer printing in terms of crack growth at the interfaces of the intermediate 2D material with the growth substrate and the target substrate. We study competing interfacial fracture paths under mixed-mode loading using cohesive zone models and beam theory to gain insight into the factors affecting the crack path selection between the two interfaces. This is expected to help design processes for successful transfer of 2D materials to the desired flexible substrate. Tucker et al. [40] studied a transfer printing system using ABAQUS® for a 600 nm thick PMMA film, considering the effects of fracture energy and crack lengths. Kim-Lee et al. [41] presented another computational study for nanomembranes as thin as 100 nm and reported on the effect of fracture energies and nanomembrane thickness with experimental validation.

To understand the effects of polymer properties, interface strengths and fracture energies on competing interfacial fracture, we present models for mixed-mode transfer of atomically thin materials based on classical beam theory and bi-linear traction-separation

relations. Data analysis is used to derive algebraic equations to correlate load, crack length, damage zone length and mode-mix with the mixed-mode fracture properties of the fracturing interface.

The outline of the paper is as follows. Section 4.2 summarizes the methods and equations used to develop the models. The results of the simulations and parametric analysis with derived equations are presented in section 4.3 with sub-sections for two different damage initiation frameworks applied to finite element and beam theory models.

4.2 METHODS AND THEORY

Consider a system (Fig. 4.1b) comprised of a 2D material (e.g., graphene) on a stiff growth substrate (e.g., copper) and a target polymer substrate (e.g., polyimide) on top in contact with the 2D material. The system is clamped along the left edge, the growth substrate is fixed along the right edge and the polymer experiences an applied displacement along its right edge. The schematic shows two interfaces (not to scale) of the 2D material: the top interface with the polymer and the bottom interface with the growth substrate both have the same initial crack length l_0. This delaminating system potentially consists of 19 parameters (elastic moduli E_j, Poisson's ratios ν_j and thicknesses h_j of the three materials, four properties for each interface as per the characteristic traction separation relation chosen, the applied end displacement Δ^* and the initial crack length at the interfaces). By considering a stiff growth substrate and a zero thickness graphene layer, we limit our parameter space to focus on the effect of polymer properties and interface properties on crack path selection during competing interface fracture. The cohesive zone model for an interface is explained in section 4.2.1.

(a)

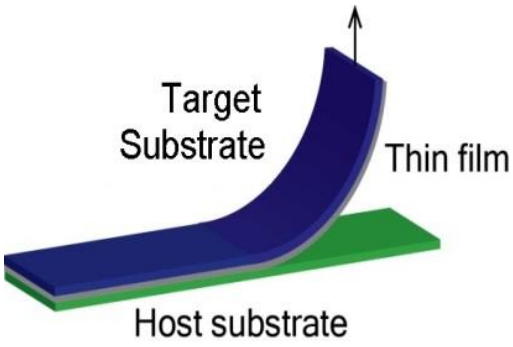

(b)

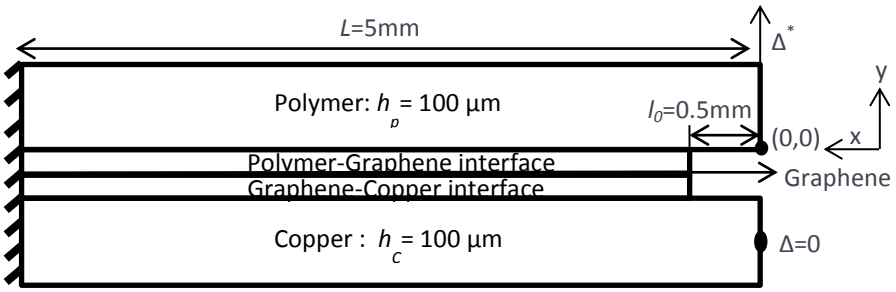

Figure 4.1: (a) General schematic of transfer printing. (b) Model schematic of a 2D material transfer system from a stiff substrate to a flexible polymer.

4.2.1 Cohesive Zone Model

As explained in the previous chapter, cohesive zone models for interfaces have three main characteristics: the shape of the traction-separation relation (linear, bi-linear, trapezoidal, exponential, polynomial or multi-linear), the criterion for damage initiation and the criterion for failure of the interfaces. Here, a bi-linear traction-separation relation is chosen as shown in Fig. 4.2. The criterion for failure is based on the total critical displacement δ_c or total fracture energy Γ_c. The initiation criteria for mixed-mode fracture are comparatively more complex and the criteria used in this work are described below.

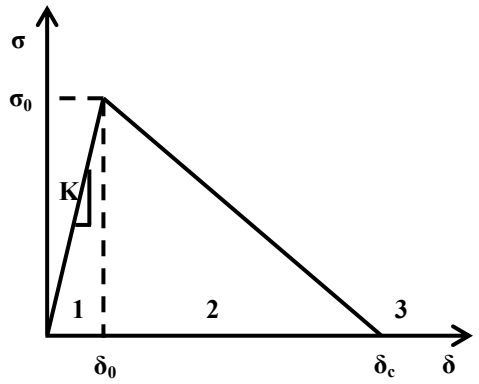

Figure 4.2: Schematic of a bi-linear normal traction-separation relation for an interface.

The first one to be considered is the maximum stress condition. In this case, interfacial damage is initiated when the maximum nominal stress ratio (defined in Eqn. 4.1a) reaches a value of one.

$$\max\left\{\left(\frac{\sigma}{\sigma_0}\right),\left(\frac{\tau}{\tau_0}\right)\right\}=1, \tag{4.1a}$$

where σ_0 and τ_0 are the normal and shear interface strengths. Next, the quadratic stress condition is based on the normal and shear stresses at the interface and damage is initiated when

$$\left(\frac{\sigma}{\sigma_0}\right)^2+\left(\frac{\tau}{\tau_0}\right)^2=1\ . \tag{4.1b}$$

The displacement at the moment of damage initiation is considered to be δ_0.

4.2.2 Finite Element Simulations

The commercial finite element software ABAQUS® is used to simulate the graphene transfer schematic of Fig. 4.1b. Interface elements are modeled using cohesive elements with a bilinear traction-separation relation and 2D plane strain continuum reduced integration (CPE4R) elements are used for the polymer and copper substrates. A rigid beam type multi-point constraint is defined at the edges of the substrates to

prescribe the displacement boundary conditions. A mesh size of 10 microns is used to ensure a sufficient number of cohesive elements in the damage zone, numerical convergence and reasonable simulation run time. Polymer elastic modulus, interface strength, interface stiffness and fracture energy are varied in order to understand their effect on interface selection for crack growth. Two different cohesive zone models are studied; one model is based on the maximum stress for damage initiation and the other model uses a quadratic stress condition for damage initiation. This allows us to explore the standard cohesive zone modeling functionalities of ABAQUS® and identify any differences in crack path selection.

In some cases, ABAQUS® simulations with cohesive elements fail to converge or obtain stress equilibrium without any explicit reason. On the other hand, a beam model on elastic foundation combined with cohesive zone model provides a simple tool for a parametric study of competing fracture with at least 1000x faster run time and convergence in cases where ABAQUS® fails to get converged solutions. The thickness of the layers and the deflections in this system are such that beam theory can be used to describe the forces. For this reason, a beam theory model is developed for simulating mixed-mode graphene transfer and the following section details the differential equations and boundary conditions used for it.

4.2.3 Beam Theory

For the polymer beam with a moment of inertia I, the normal deflection Δ is given by

$$E^* I \frac{d^4\Delta}{dx^4} - \frac{bh_P}{2}\frac{d\tau_i(x)}{dx} + b\sigma_i(x) = 0 \tag{4.2}$$

and $\Delta = w_1 + w_2$, (4.3)

where w_i are the normal displacements for the interfaces (subscript 1 is for the polymer-graphene interface while subscript 2 is for the graphene-copper interface), $E^* = E/(1-\nu^2)$ for plane strain and the shear displacement for each interface is $u_i = (h/2)(dw_i/dx)$. The displacements are positive in the positive axis directions as shown in Fig. 1b. The cohesive zone interactions are accounted for in the terms $\sigma_i(x)$ and $\tau_i(x)$ which are the normal and shear tractions acting on the interfaces. We consider an elastic region of length L_1^*(region 1), a damage region of length L_2 (region 2)and a traction-free crack length $L_3 \geq l_0$ (region 3). The stresses in each region can be expressed as

$$\sigma_i = \begin{cases} K_{i1} w_i & , \text{ region 1} \\ K_{i1}(1-D_i) w_i & , \text{ region 2} \\ 0 & , \text{ region 3} \end{cases} , \quad \tau_i = \begin{cases} K_{i2} u_i & , \text{ region 1} \\ K_{i2}(1-D_i) u_i & , \text{ region 2} \\ 0 & , \text{ region 3} \end{cases} . \tag{4.4}$$

Here, K_{i1} and K_{i2} are the interface stiffness values of interface i in the normal and shear direction, respectively, while D is the damage parameter which varies between 0 (no damage) and 1 (complete damage) for each interface and is expressed as $D_i = \delta_{ci}(\delta_i - \delta_{0i})/(\delta_i(\delta_{ci} - \delta_{0i}))$ where $\delta_i = \sqrt{u_i^2 + w_i^2}$. When $D_i = 1$ for an interface, the crack grows at that interface. If the crack grows at the graphene-copper interface, graphene transfer is successful.

For this system with two interface elements in contact (the graphene layer is not explicitly included in the model as it is atomically thin), equilibrium ensures that each interface experiences equal normal and shear tractions. We will use tractions on the graphene-copper interface to show the equations in case of crack growth at that interface. Replacing the subscript 2 with subscript 1 will yield equations for the other case. For damage at the bottom interface, substituting the equation for tractions from Eqn. (4.4)

into Eqn. (4.2), we have the following three differential equations for each region of the bottom interface:

$$E_P^* I \frac{d^4\Delta}{dx^4} = 0, \qquad 0 \le x \le L_3 \quad (4.5a)$$

$$E_P^* I \frac{d^4\Delta}{dx^4} - \frac{bh_P}{2}\frac{d}{dx}\left(K_{22}(1-D_2)\frac{h}{2}\frac{dw_2}{dx}\right) + bK_{21}(1-D_2)w_2 = 0, \qquad L_3 \le x \le L_2 + L_3 \quad (4.5b)$$

$$E_P^* I \frac{d^4\Delta}{dx^4} - \frac{bh_P}{2}\frac{d}{dx}\left(K_{22}\frac{h}{2}\frac{dw_2}{dx}\right) + bK_{21}w_2 = 0 \qquad L_2 + L_3 \le x \le L_1^* + L_2 + L_3 . \quad (4.5c)$$

When interface *2* damages and interface *1* exhibits an elastic response, equilibrium implies that:

$$K_{21}(1-D_2)w_2 = K_{11}w_1 \;\; ; \;\; K_{22}(1-D_2)u_2 = K_{12}u_1, \qquad L_3 \le x \le L_2 + L_3 \quad (4.6a\text{-}b)$$

$$K_{21}w_2 = K_{11}w_1 \;\; ; \;\; K_{22}u_2 = K_{12}u_1 \qquad L_2 + L_3 \le x \le L_1^* + L_2 + L_3 . \quad (4.6c\text{-}d)$$

These equations are non-dimensionalized by normalizing x with h_P and displacements (Δ, w_1,w_2) with Δ^*. In region 1, equations (4.3, 4.5c and 4.6c) can be combined to give the following dimensionless equation:

$$\frac{d^4 w_2}{dx^4} - \frac{3h_P K_{22}}{E_P^*}\left(\frac{d^2 w_2}{dx^2}\right) + \frac{12h_P K_{21}K_{11}}{E_P^*(K_{11}+K_{21})}w_2 = 0. \quad (4.7)$$

For decaying displacements, the general dimensionless solution to Eqn. 4.7 is given by

$$w_2 = A\exp(-\frac{\alpha x}{\sqrt{2}}) + B\exp(-\frac{\beta x}{\sqrt{2}}), \quad (4.8)$$

where, $\alpha = \sqrt{\frac{3K_{22}h_P}{E_P^*} - \sqrt{\left(\frac{3K_{22}h_P}{E_P^*}\right)^2 - \frac{48K_{21}K_{11}K_{22}h_P}{E_P^*(K_{11}+K_{21})}}}$,

$\beta = \sqrt{\sqrt{\left(\frac{3K_{22}h_P}{E_P^*}\right)^2 - \frac{48K_{21}K_{11}K_{22}h_P}{E_P^*(K_{11}+K_{21})}} + \frac{3K_{22}h_P}{E_P^*}}$ and A and B are constants of integration.

Note that $(K_{11}+K_{21})K_{22}^2 h_P/(K_{21}K_{11}E_P^*) > 16/3$ is required for real values of exponential coefficients in region 1 of interface *2* (Eqn. 4.8) and $(K_{11}+K_{21})K_{12}^2 h_P/(K_{21}K_{11}E_P^*) > 16/3$ is required for real solutions in region 1 of interface

1. Comparing the differential of Eqn. 4.6c with Eqn. 4.6d yields $K_{11}/K_{21} = K_{12}/K_{22}$. For an interface with characterized strength and fracture energy, these three equations constrain the interface stiffness values and consequently the values of δ_0.

Knowing the solution in region 1, we obtain boundary conditions (Eqns. 4.9c-d) for the elastic-damage boundary. The differential equations for regions 2 (Eqns. 4.6b, 4.7a, 4.7b) and region 3 (Eqn. 4.6a) are solved with a shooting method because boundary locations depend on L_2 and L_3 which are not fixed. In addition to continuity of displacements, rotation, moments and forces at the boundaries, the other boundary conditions for the system of differential equations are:

$$\Delta = \Delta^*, \quad \frac{d^2\Delta}{dx^2} = 0 \qquad : x = 0, \qquad \text{(4.9a-b)}$$

$$\frac{(\alpha+\beta)}{\sqrt{2}}\frac{d^2 w_2}{dx^2} + \frac{d^3 w_2}{dx^3} + \frac{\alpha\beta}{2}\frac{dw_2}{dx} = 0 \qquad : x = L_2 + L_3, \qquad \text{(4.9c)}$$

$$\frac{\alpha\beta^2 w_2}{2\sqrt{2}} - \frac{d^3 w_2}{dx^3} - \frac{\alpha}{\sqrt{2}}\frac{d^2 w_2}{dx^2} + \frac{\beta^2}{2}\frac{dw_2}{dx} = 0 \qquad : x = L_2 + L_3, \qquad \text{(4.9d)}$$

and boundaries are defined at steady state by displacements at interface *2* :

$$\delta_2 = \sqrt{w_2^2 + u_2^2} = \delta_0 \quad : x = L_2 + L_3, \qquad \delta_2 = \sqrt{w_2^2 + u_2^2} = \delta_c \quad : x = L_3. \qquad \text{(4.9e-f)}$$

During the damage zone growth, Eqn. 4.9f is not required since the boundary is known to be at $x = l_0$.

The equations are solved using a shooting method with MATLAB®. A guess is made for $d\Delta/dx$ and $d^3\Delta/dx^3$ at $x = 0$ to solve Eqn. 4.6a for the cracked region followed by the damaged region (Eqns. 4.6b, 4.7a-b) and guesses are updated based on Eqns. 4.10c-d for convergence. The next section discusses the results for finite element and beam theory simulations for the two different initiation and propagation criteria.

4.3 RESULTS AND DISCUSSION

In this section, we present the results from the finite element and beam theory analyses that have just been outlined. An extensive parametric study leads to selective transfer maps based on dominant parameters. A scaling analysis is also included.

4.3.1 Maximum Stress Initiation Criterion

Results are first presented for the stress-based damage initiation criterion, starting with finite element solutions followed by beam theory ones.

4.3.1.1 Finite Element Simulations

In the parametric study that follows, material and interface properties are varied as listed in Table 4.1 with parenthetical values indicating the baseline case. The interface properties for the graphene-copper interface are based on values reported by Na et al. [37] The interface strength in both directions is kept identical because in cases of different directional strengths of comparable magnitudes, damage is observed in both interfaces and simulations abort. For the baseline case where the graphene-copper interface has lower strength and fracture energy compared to the other interface, graphene transfer to the polymer is observed.

The effect of polymer elastic modulus on the load-displacement behavior is shown in Fig. 4.3a along with interface damage (see the damage contours SDEG in Figs. 4.3b-c). A lot of interface element distortion (shape changes from square to trapezoidal) can be seen for the compliant polymer with an elastic modulus of 100 MPa and both interfaces have a non-zero damage parameter. No interfacial separation is observed for this case (crack does not grow at any interface in the ABAUQS® screenshot for E_P = 100 MPa) while successful transfer of graphene to the polymer is observed for stiffer

polymers (indicated by crack growth at the graphene-copper interface in Fig. 4.3b for EP = 2500 MPa).

Table 4.1: Material properties and interface properties for the study of Graphene (Gr) transfer in ABAQUS®.

	Polymer	**Copper**	**Polymer-Gr interface**	**Copper-Gr interface**
Elastic Modulus (MPa)	100-5000 (2500)	110,000		
Poisson's Ratio	0.34	0.34		
Interface Strength (MPa)			0.1-4 (1)	0.5
Fracture Energy (J/m^2)			0.1-10 (8)	6
Interface Stiffness (MPa/mm)			100,000	50,000-1,000,000 (100,000)

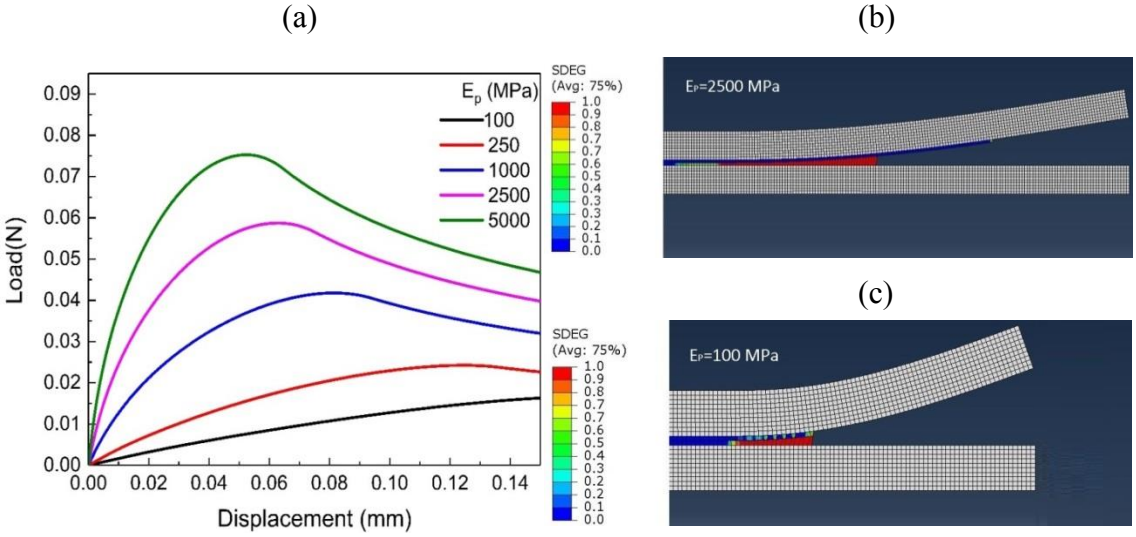

Figure 4.3: Effect of polymer elastic modulus on graphene transfer. (a) Load-displacement response, (b) the polymer-graphene interface has no damage for polymers with high elastic modulus but (c) compliant polymers have significant damage in both interfaces.

Variations in interface stiffness show no effect on interface selection or crack propagation as it is a secondary parameter when strength and fracture energy are fixed [69]. The effect of interface stiffness on crack length, damage zone length and mode-mix (defined as $\Psi_c = \tan^{-1}(u_i / w_i)$) is shown in Figs. 4.4a-b.

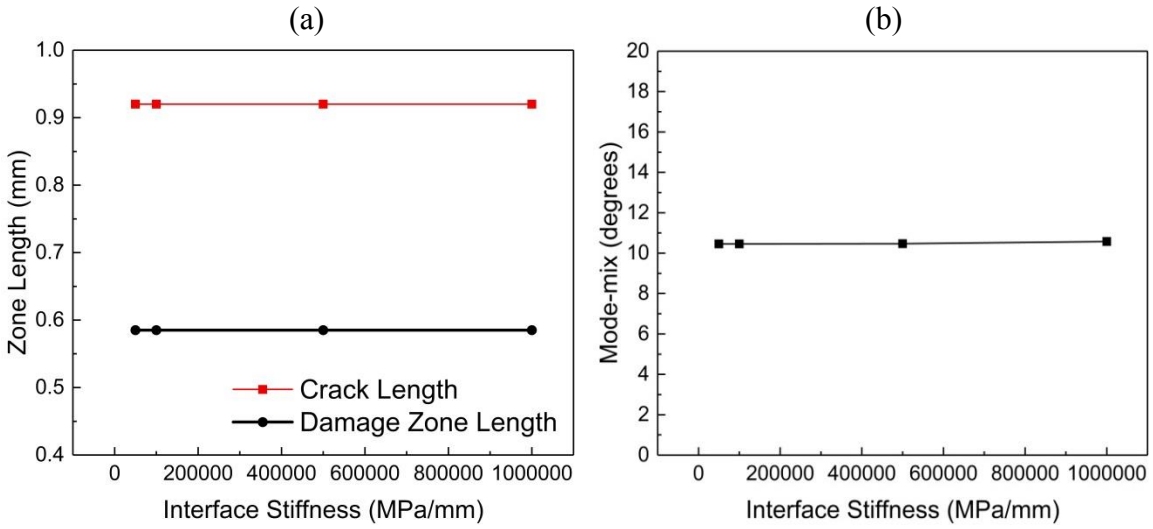

Figure 4.4: Effect of interface stiffness on (a) crack length, damage zone length and (b) absolute mode-mix at the crack tip (the mode-mix stays constant at -10.5^0).

For a fixed fracture energy, varying the strength changed the fracture locus depending on which interface had higher strength. On the other hand, changes in fracture energy for a given strength did not alter the interface selection or the load-displacement behavior. The value of the non-dimensional group $E^*\Gamma / \sigma^2 l_0$ governs the transition from strength driven fracture to fracture energy driven fracture for Mode I loading [126] and for mixed-mode single interface fracture [127]. This non-dimensional parameter has a large value of 135.6 for the graphene-copper interface indicating that graphene transfer is strength driven and Linear Elastic Fracture Mechanics (LEFM) is invalid based on the traction-separation relation reported by Na et al. [37]. Results presented in Fig. 4.5

suggest the same behavior for competing fracture.

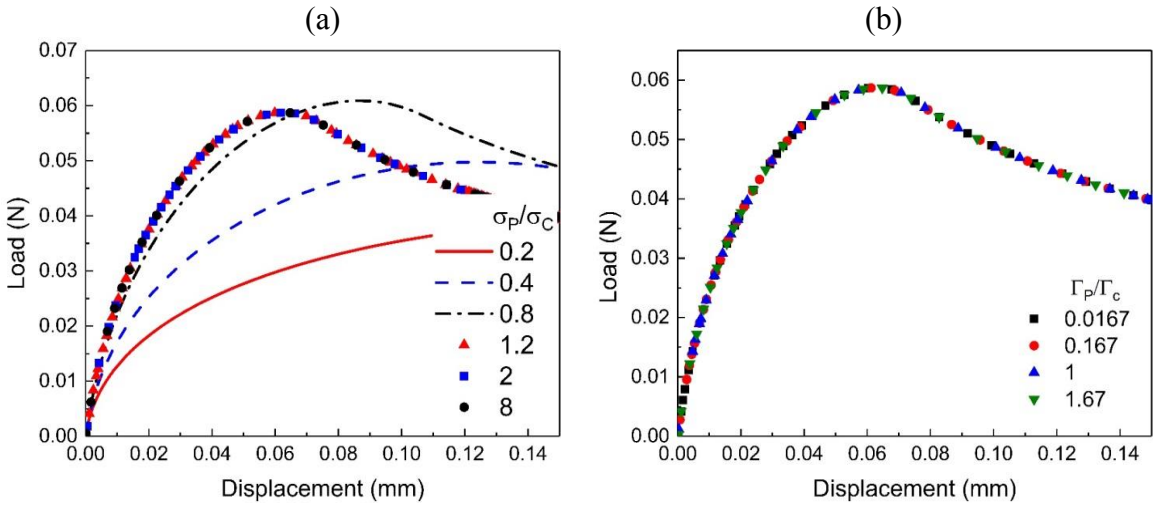

Figure 4.5: (a) Effect of variation in polymer-graphene interface (subscript P) strength when fracture energy of graphene-copper interface (subscript C) is lower. (b) Effect of variation in polymer-graphene interface fracture energy when strength of graphene-copper interface is lower.

As can be seen from Fig. 4.5a, when the ratio of interface strengths suggests a stronger polymer-graphene interface ($\sigma_1/\sigma_2 > 1$), changing $\sigma_1 (= \tau_1)$ has no effect on the load-displacement curve since it is the graphene-copper interface that fractures. But in the cases of strength ratio less than 1, the polymer-graphene interface fractures despite the fracture energy favoring crack growth at the graphene-copper interface.

The fracture map when both interface strengths are varied such that $E^*\Gamma/\sigma^2 l_0$ varies between 0.94 and 135.6 is shown in Fig. 4.6. For higher strengths, the effects of fracture energy begin to appear and considerable damage is seen at both interfaces along with cohesive element distortions before simulations abort (ABAQUS® screenshots in

Fig. 4.6). This happens for cases where strength favors the graphene-copper interface to break but fracture energy favors crack growth at the polymer-graphene interface.

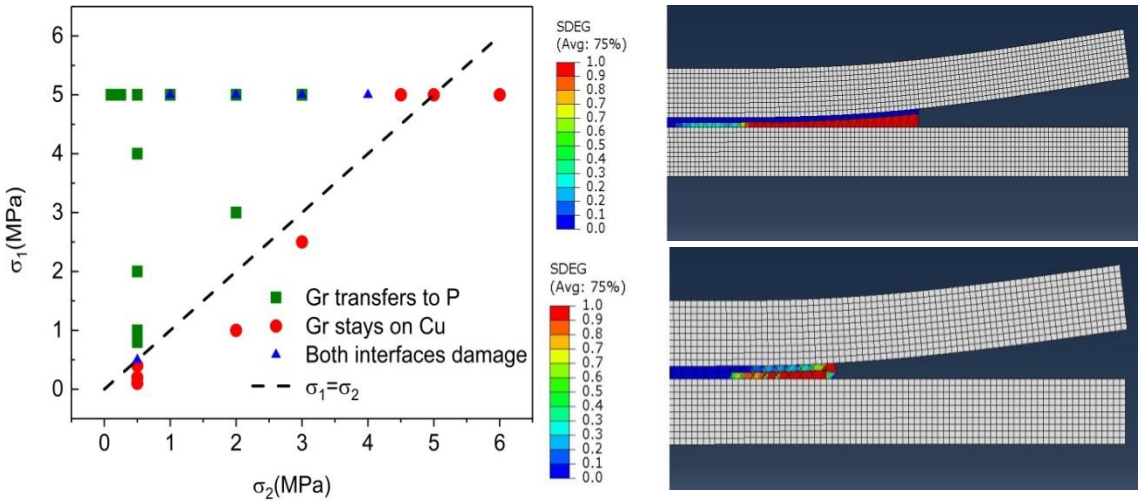

Figure 4.6: Fracture map showing the effect of interface strengths on graphene (Gr) transfer. ABAQUS® screenshots show the damage contours (SDEG) and element distortion at the interfaces for two cases- Top: $\sigma_1 = 5\,MPa, \Gamma_1 = 0.01\,\text{mJ/mm}^2, \sigma_2 = 1\,\text{MPa}, \Gamma_2 = 0.015\,\text{mJ/mm}^2$ and Bottom: $\sigma_1 = 5\,\text{MPa}, \Gamma_1 = 0.01\,\text{mJ/mm}^2, \sigma_2 = 4\,\text{MPa}, \Gamma_2 = 0.015\,\text{mJ/mm}^2$.

4.3.1.2 Beam Theory Simulations

For the maximum stress initiation simulations, it is evident from Fig. 4.4b that the transfer process is Mode I dominant with a mode-mix of only -10.5^0 at the crack tip. We simplify the mixed-mode beam theory by ignoring the shear stress terms to compare how close the model simulations approach the results from finite element simulations. The beam deflections and the load-displacement responses obtained from the beam theory and finite element simulations for the baseline case are compared in Figs 4.7a-b where good agreement is observed.

(a)

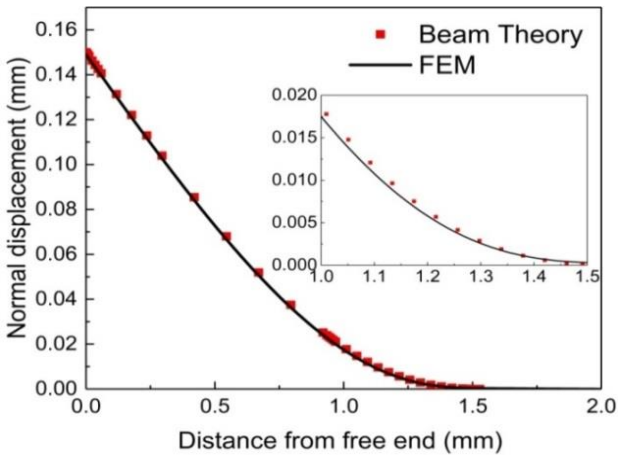

(b)

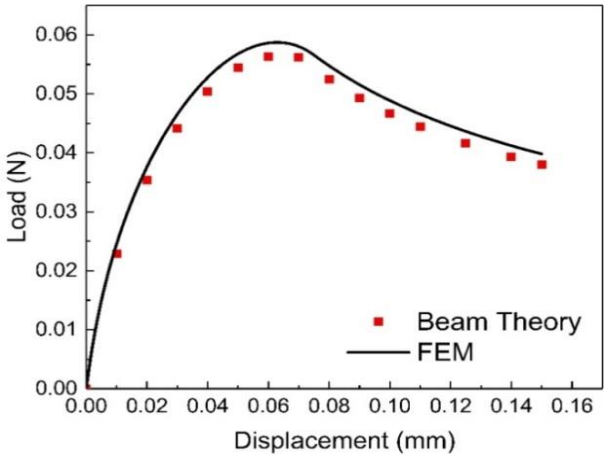

Figure 4.7 (a) Normal deflections of the beam provided by the beam theory and finite element simulations for the baseline case. The inset shows deflections in the damage zone. (b) Comparison of the load-displacement responses from the beam theory and finite element simulations.

Neglecting the shear stress in the beam theory model leads to differences in the stress distribution as shown in Fig. 4.8 because the initiation point has a very high mode-mix in ABAQUS® simulations. But the prediction of crack length and damage zone length only differs by 1.5% while the RMS error for the steady state load predictions is

4.5%. The stress distribution in Fig. 4.8 is only calculated for regions 2 and 3 in the beam theory solution since the boundary conditions (Eqns. 4.9c-d) are applied at the damage initiation point.

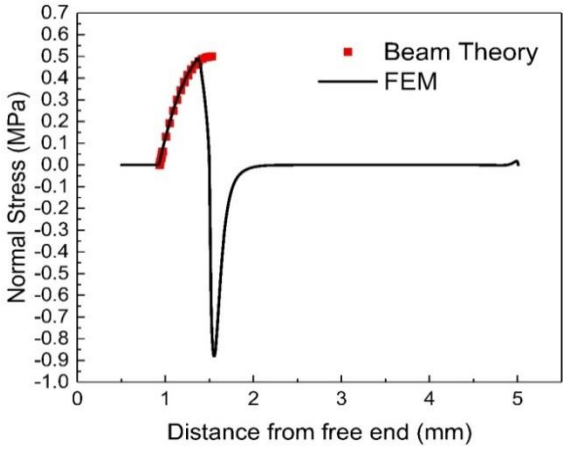

Figure 4.8: Comparison of the normal stress distribution at the polymer surface from beam theory and finite element simulations. Agreement is observed except at the transition between elastic zone and damage zone.

4.3.1.3 Scaling Analysis

For mode I dominant graphene transfer with damage initiation governed by the maximum stress criterion, the fracture is strength driven and equilibrium between the two interfaces implies that the non-fracturing interface will only exhibit an elastic response while the fracturing interface transitions from elastic behavior to damage growth to steady state crack propagation. In this scenario, we can neglect the displacements of the non-fracturing interface since they will be a few orders of magnitude smaller than the interface in its damage zone. Thus, Eqn. 4.5b reduces to:

$$E^* I \frac{d^4 w_2}{dx^4} + bK_{21}(1-D_2)w_2 = 0 \qquad L_3 \le x \le L_2 + L_3 \ , \tag{4.10}$$

and the system of equations resembles the equations for Mode 1 single interface fracture [111]. Scaling equations derived in our previous works [111, 125] are compared to the equations that fit the data for graphene transfer in Table 4.2. The parametric dependence is same for the most part with only a change in the *O(1)* number. A comparison of the fit is shown in Fig. 4.9a-d for the four scaling equations and excellent agreement is observed.

Table 4.2: Summary of the scaling equations to predict rotation, damage zone length, crack length and load for interface fracture (dependence on polymer material properties and traction-separation relation of the fracturing interface).

Previously obtained scaling equations for single interfaces	**Equations that fit graphene transfer data**
$\left.\frac{dw}{dx}\right\|_{x=0} = 1.61\left(\frac{K\delta_0\delta_c}{E^*h}\right)^{1/4}\left(\frac{\Delta}{h}\right)^{1/2}$ [125]	$\left.\frac{dw}{dx}\right\|_{x=0} = 1.6\left(\frac{K\delta_0\delta_c}{E^*h}\right)^{1/4}\left(\frac{\Delta}{h}\right)^{1/2}$ (4.11a)
$\frac{L_2}{h} = 1.1\left(\frac{E^*}{\sigma_0 h}\right)^{1/4}\left(\delta_c^{1/4}-\delta_0^{1/4}\right)$ [111]	$\frac{L_2}{h} = 1.1\left(\frac{E^*}{\sigma_0 h}\right)^{1/4}\left(\delta_c^{1/4}-\delta_0^{1/4}\right)$ (4.11b)
$\frac{L_3}{h} = 2\left(\frac{E^*\delta_c}{\sigma_0 h}\right)^{1/4}\left[\left(\frac{\delta_c}{\Delta}\right)^{-1/3}-1\right]$ [111]	$\frac{L_3}{h} = 1.83\left(\frac{E^*\delta_c}{\sigma_0 h}\right)^{1/4}\left[\left(\frac{\delta_c}{\Delta}\right)^{-1/3}-1\right]$ (4.11c)
$\frac{Ph^2}{E^*I} = 3.74\left(\frac{\sigma_0}{E^*}\right)^{3/4}\frac{\delta_c^{3/4}}{h^{1/4}\Delta^{1/2}}$ [111]	$\frac{Ph^2}{E^*I} = 3.74\left(\frac{\sigma_0}{E^*}\right)^{3/4}\frac{\delta_c^{3/4}}{h^{1/4}\Delta^{1/2}}$ (4.11d)

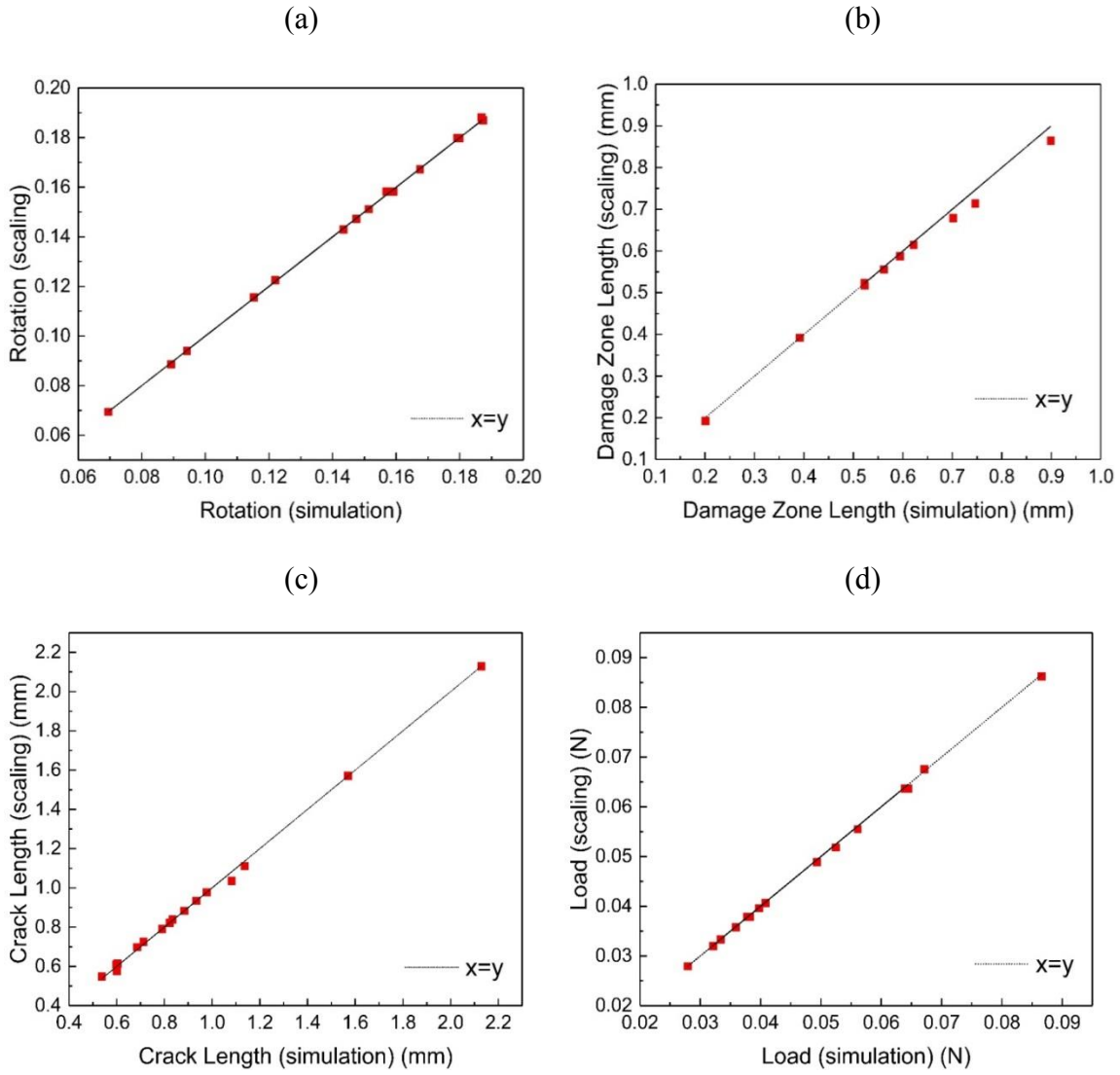

Figure 4.9: Comparison of scaling equation with beam theory results for (a) rotation at displaced end, (b) damage zone length, (c) crack length and (d) steady state load for graphene transfer.

4.3.2 Quadratic Stress Damage Initiation Criterion

The effect of changing the damage initiation criterion to the quadratic one is now considered.

4.3.2.1 Finite Element Simulations

ABAQUS® simulations are modified to provide a quadratic stress criterion for damage initiation. The material properties are same as the baseline case in Table 4.1 while the traction-separation relations of both interfaces are varied. The fracture map obtained for these simulations is shown in Fig. 4.10a. Quadrant 2 is for the cases where the polymer-graphene interface has higher strength and higher fracture energy (and hence, graphene transfers to polymer) while quadrant 3 represents situations where the copper-graphene interface has higher strength and fracture energy, and graphene stays on the copper foil (red data points). Quadrants 1 and 4 are the non-trivial regions. Finite element results in these quadrants suggest that graphene transfer to the polymer is unsuccessful for unfavorable strength but unfavorable fracture energy can be compensated for with higher strengths to obtain successful graphene transfer (black data points in quadrant 4). While these results are interesting, a closer look at the stress equilibrium in cohesive elements suggested that there are issues with the results in the fourth quadrant. The stresses at both interfaces should be equal in order to satisfy equilibrium in the cohesive elements. However, even though simulations converged, continuity in the normal and shear tractions was not satisfied in cohesive elements ahead of the crack front as can be seen in Fig. 4.10b.

For this reason, the fracture map obtained from the finite element simulations may not be reliable. The next section describes the results from beam theory that satisfies all the necessary constraints and equilibrium equations during crack propagation. A user element is also developed in ABAQUS® in order to further validate the beam theory results.

(a) (b)

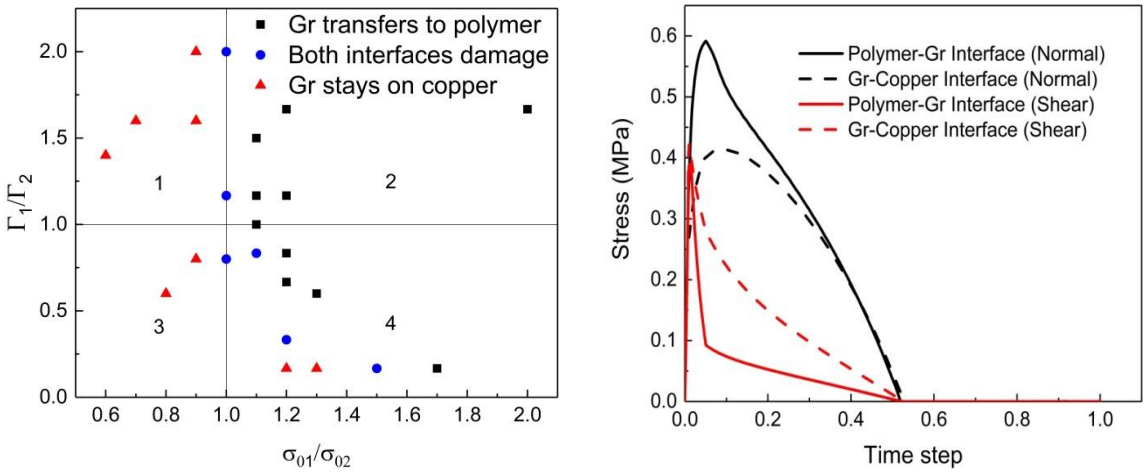

Figure 4.10: (a) Fracture map obtained from finite element solutions for graphene transfer with a quadratic stress damage initiation criterion. (b) Traction inequalities between the two interfaces at a location within the cohesive zone for the 4th quadrant condition ($\sigma_1/\sigma_2 = 1.2, \Gamma_1/\Gamma_2 = 0.67$).

4.3.2.2 Beam Theory Results

Since fracture is strength driven for the graphene transfer system, the beam theory model is developed with the assumption that the interface that experiences damage initiation first will experience crack growth while the other interface will always remain in the elastic regime. This ignores the cases where damage is seen at both interfaces (these cases are undesirable for material transfer). The beam theory model has another limitation that it converges for steady state simulations when the difference between δ_0 and δ_c is at most two orders of magnitude. A larger difference in the displacements leads to unrealistic stress distributions at the interface due to numerical issues in locating the damage initiation point for very small δ_0 values. Unfortunately, this is the case for the traction-separation relation [37] for the interface between graphene and copper that has been used so far in this paper.

The parameters for the traction-separation relations that were used for the mixed-mode beam theory are thus, considerably different and summarized in Table 4.3. Xin et al. [128] reported adhesion energy of as-grown graphene on copper foil in the range of 0.74-1.53 J/m^2 with a blister test which is considerably lower than 6 J/m^2 reported for rate-dependent graphene transfer [37]. The fracture energies for parameters in Table 4.3 fall in the same range as that of the blister test results. The parametric variation here also includes cases where $\sigma_0 \neq \tau_0$. The values were selected absent any reported values of parameters for mixed-mode traction-separation relations of graphene - seed copper interfaces. For the baseline case, the quantity $E^*\Gamma / \sigma^2 l_0$ has a value of 0.8. The fracture map for damage initiation (rather than steady state crack growth) is shown in Fig. 4.11. This fracture map is only a function of strengths because other properties such as E^*, h, Γ (or δ_c) have no effect on damage initiation. Quadrants 1 and 4 illustrate the interplay between directional strengths when the interface selection is non- intuitive.

Table 4.3: Parameters for traction-separation relations for mixed-mode graphene transfer with quadratic stress initiation criterion.

TSR Parameters	**Polymer-Gr interface**	**Copper-Gr interface**
Normal Interface Strength (MPa)	3.5-5 (4.5)	3-7 (3.5)
Shear Interface Strength (MPa)	3.5-6 (4.5)	2.5-9 (3.5)
Critical Displacement (mm)	0.0024	0.0008-0.0017 (0.001)
Interface Stiffness (MPa/mm)	100,000	100,000

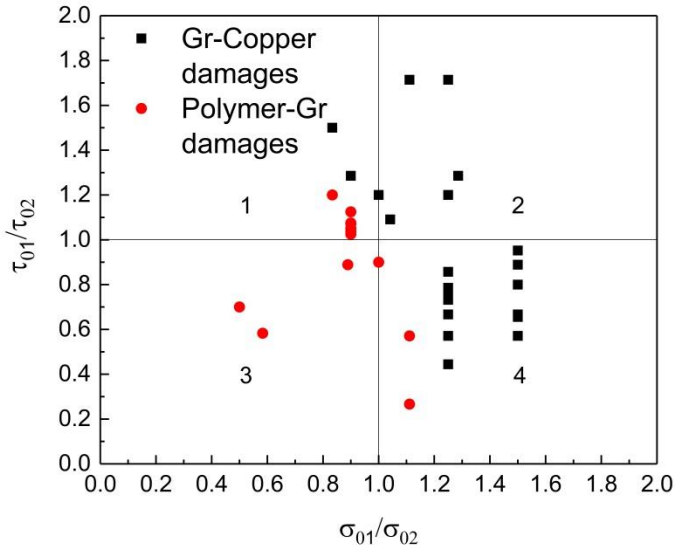

Figure 4.11: Quadratic stress damage initiation map for graphene transfer.

Steady state solutions were obtained once the damaging interface had been identified. Results for steady state crack growth in the baseline case (quadrant 2) are shown in Figs. 4.12a-d. The damage zone length increases until steady state is reached after which crack length increases steadily in Fig. 4.12b. The stress distribution in Fig. 4.12c shows that normal traction is higher at damage initiation and its subsequent decrease is contrasted by a temporary increase in the shear traction. The crack-tip mode-mix remained at a value of -32.9^0 during steady state growth. The evolution of the mode-mix during the development of the cohesive zone is shown in Fig. 4.12d.

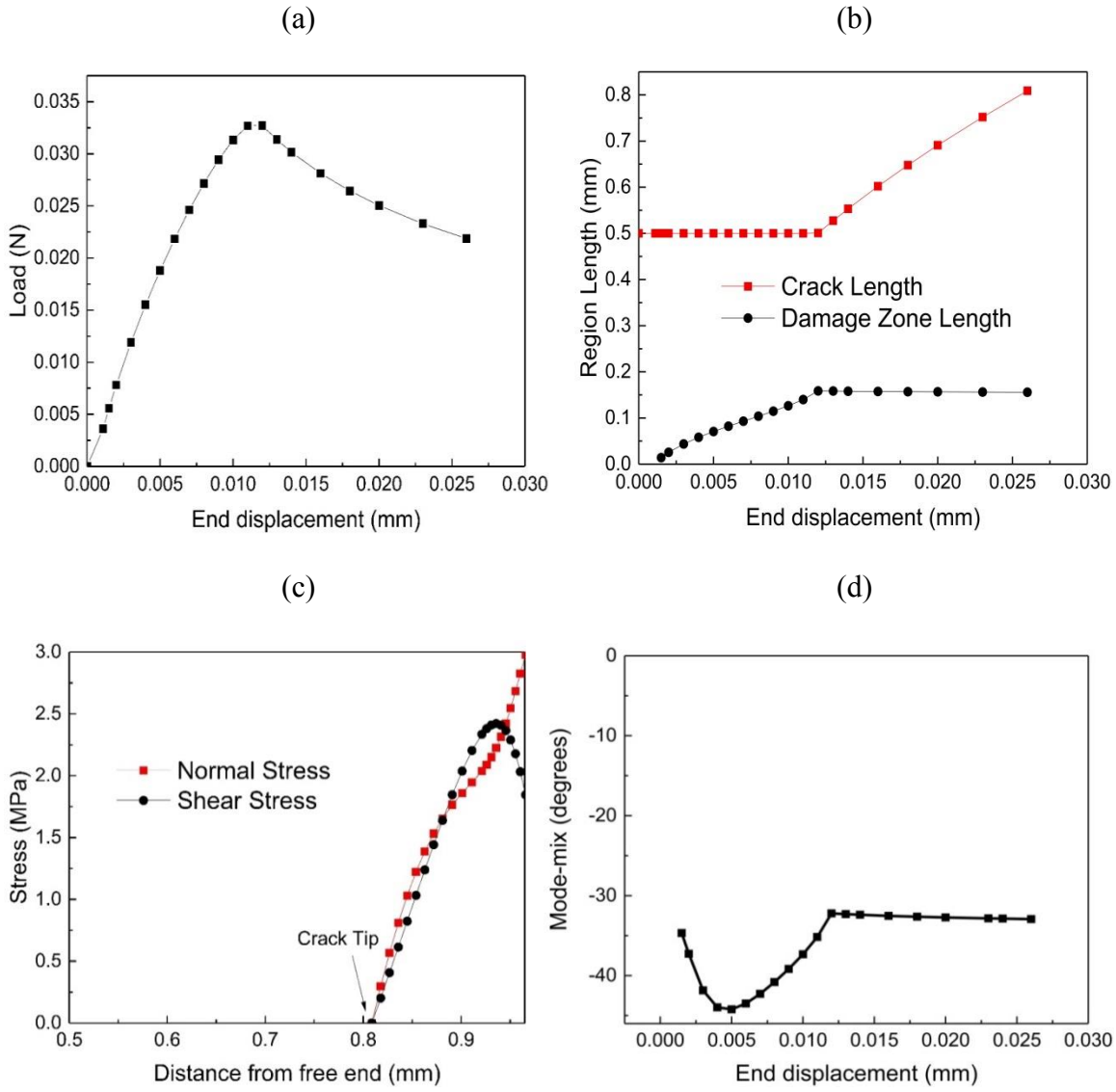

Figure 4.12: Simulation results for steady state growth in the baseline case: (a) load-displacement behavior, (b) crack length and damage zone length, (c) stress distribution at the interface at an end displacement of 0.026 mm and (d) variation in mode-mix at the crack tip.

To validate the beam theory model, a user-defined element (UEL) subroutine [129] is adopted and implemented in ABAQUS®. In the UEL subroutine, the cohesive traction and its tangent matrix are assessed by considering four conditions: contact, elastic loading, softening and complete failure. The elastic loading and softening follow

the definition of the traction-separation relation as shown in Eqn. 4.4. For the contact condition, a penalty stiffness is introduced along the normal direction to prevent material interpenetration. The penalty stiffness is defined to be the same as the initial stiffness of the traction-separation relation in order to maintain the elastic symmetry in tension and compression. Complete failure is associated with the interaction range (δ_c), outside of which the cohesive traction and the tangent stiffness are both zero. Both the polymer and copper beams are modeled by four-node plane strain reduced integral elements (CPE4R) and a tie constraint is applied to maintain the continuity conditions between adjacent layers. A comparison of the load-displacement and crack growth results is shown in Figs. 4.13a-b. Excellent agreement is observed between the models, validating the 1-D mixed mode beam theory model.

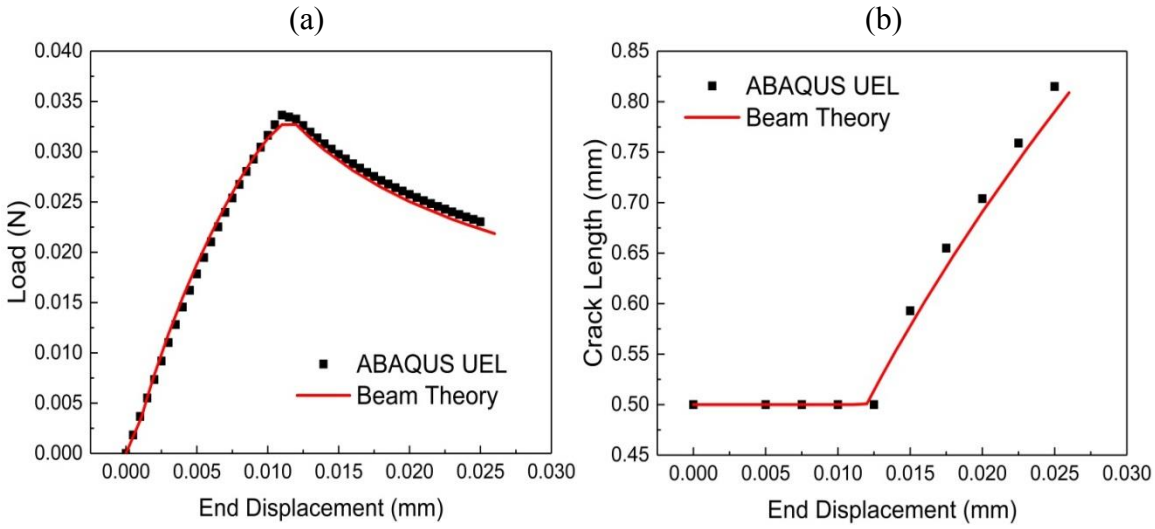

Figure 4.13: Comparison of (a) load-displacement behavior and (b) crack growth from beam theory and ABAQUS® user element simulations.

The validated beam theory model was used to conduct a parametric analysis by varying the polymer elastic modulus between 1500-3300 MPa, polymer thickness between 0.08-0.22 mm and parameters of the traction-separation relations for the

graphene-copper interface, as detailed in Table 4.3. Note that the equations only require an interchange of interface subscripts to study the fracture of the top interface. So the results from the parametric analysis can be applied to whichever interface is fracturing. Since the quadratic damage condition is met with maximum contribution from the normal stresses (see Fig. 4.12c), simulations with traction-separation relations where σ_0 is greater than τ_0 did not converge. Successful graphene transfer simulations are obtained only in quadrant 2 with $\sigma_{02} < \tau_{02}$.

We fit the data from converged simulations to obtain the relationships between load, crack length, damage zone length, rotation, mode-mix, polymer properties and the fracturing interface's traction-separation relation (Eqns. 4.12a-e). A comparison of the fit with simulation data can be seen in Figs. 4.14a-d.

$$P = 0.14(K\delta_0 h)^{0.6} E^{*0.4} \frac{b\delta_c^{0.9}}{\Delta^{0.5}}, \qquad (4.12a) \quad w' = 1.23\left(\frac{K\delta_0}{E^*}\right)^{0.2} \frac{\delta_c^{0.3}\Delta^{0.5}}{h^{0.8}}, \qquad (4.12b)$$

$$L_2 = 0.65\left(\frac{E^*}{K}\right)^{0.2}\left(\frac{\delta_c}{\delta_0}\right)^{0.34} h^{0.8}, \qquad (4.12c) \quad L_3 = 0.8\left(\frac{E^*}{K\delta_0}\right)^{0.19} \frac{\Delta^{0.6}h^{0.8}}{\delta_c^{0.4}}, \qquad (4.12d)$$

$$\text{and } \Psi_c = -49.4\left(\frac{K\delta_0 h}{E^*\delta_c}\right)^{0.2}. \qquad (4.12e)$$

While the parametric dependence is qualitatively similar to Mode I dominant situations, the power dependences are significantly different. Also note that the value of interface stiffness for both interfaces in all directions is kept equal in our simulations (while ensuring that the constraints on *K* are satisfied). In case of variations in interface stiffness, the functional dependence on *K* will likely be a combination of the different stiffness values. The parameter δ_0 is also not straightforward as it depends on both σ_0 and τ_0 of the fracturing interface and requires a damage initiation simulation to be

estimated. δ_0 is plotted as a function of σ_0 and τ_0 in Fig. 4.15 where $\delta_0 \propto \sigma_0^{0.6}$ and $\delta_0 \propto \tau_0^{0.2}$.

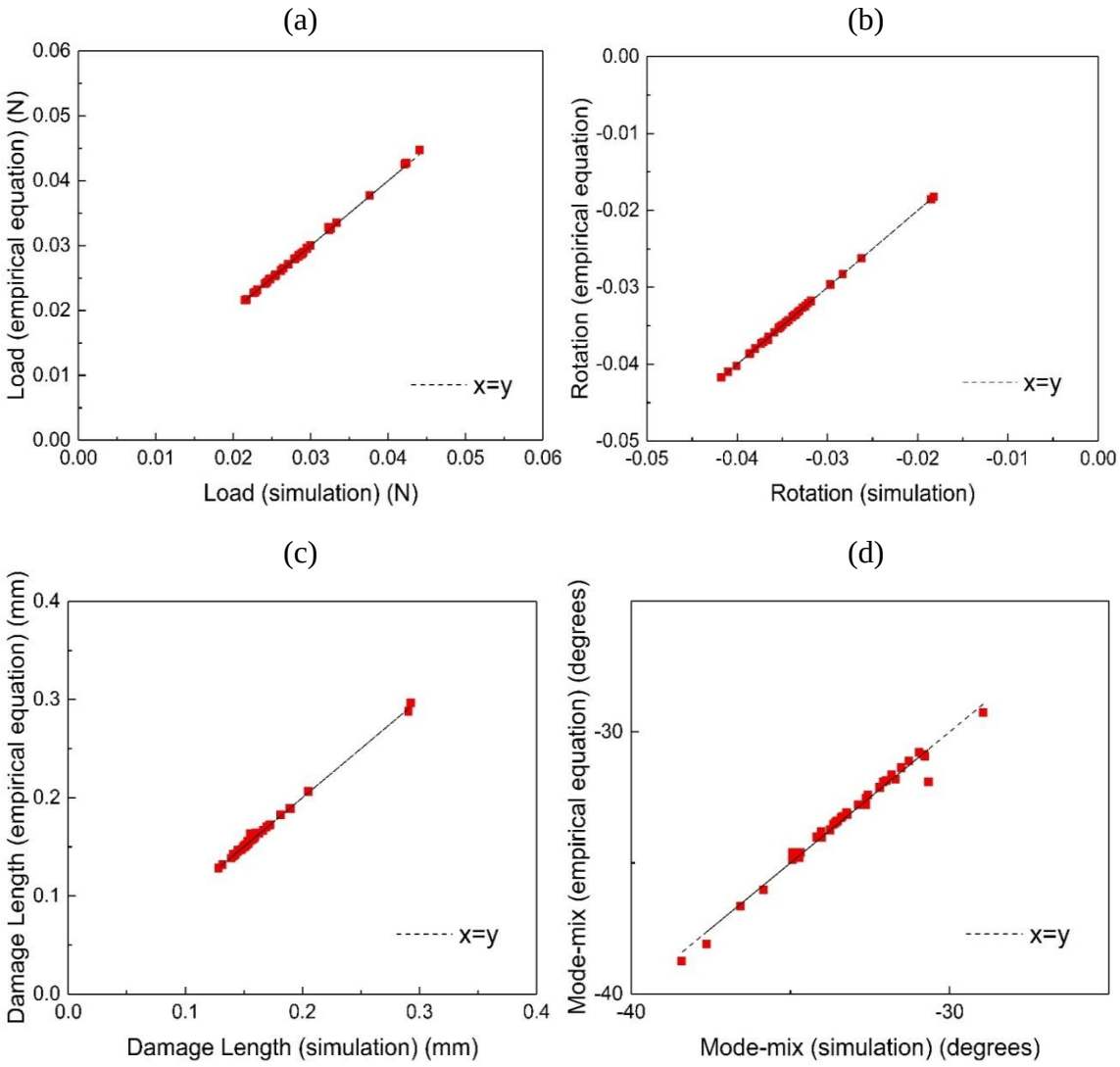

Figure 4.14: Comparison of steady state beam theory simulation results with the empirically obtained equations for (a) load, (b) rotation, (c) damage zone length and (d) mode-mix at the crack tip.

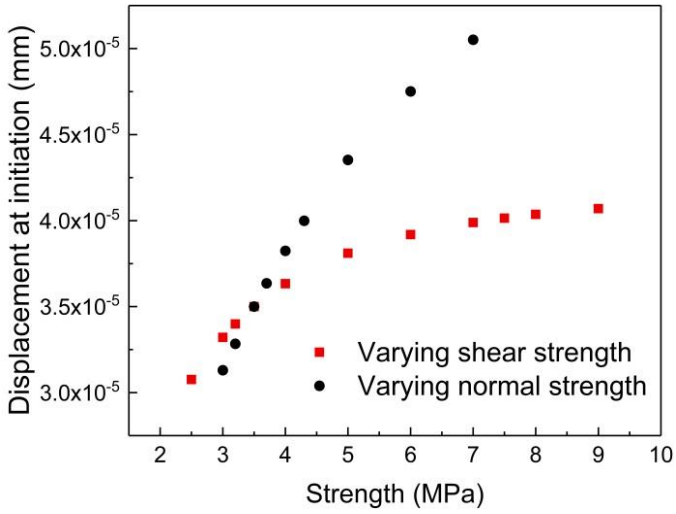

Figure 4.15: Dependence of δ_0 on changing interface strengths relative to the baseline case.

4.4 CONCLUSIONS

2D material transfer for a baseline system of polyimide-graphene-copper along with parametric variation in polymer and interface properties was modeled using the finite element method as well finite difference solutions to beam theory equations. Both maximum and quadratic stress damage initiation criteria were explored. Finite element simulations of competing fracture indicate it is driven by interface strength with no effect of fracture energy for values of $E^*\Gamma/\sigma^2 h > 10$. A low mode-mix of roughly -10^0 was observed at the crack tip in the case of maximum stress initiation criterion and the results compare well with the beam theory model that ignores shear stress terms. Scaling equations derived in previous works for single interface fracture fit perfectly for the competing fracture results of graphene transfer. However, ABAQUS® cohesive element simulations with the quadratic stress criterion exhibited unphysical interface stress distributions for certain traction-separation relations. The mixed-mode beam theory model enforces equilibrium and converges for most cases. A mode-mix of roughly -33^0

was observed at the crack tip. The empirical equations that fit the results have significantly different power laws for the parameter space explored for the quadratic stress initiation compared to a damage initiation criterion based on a Mode I dominant maximum stress. It is evident from the results that successful transfer of graphene is driven by interface strengths and not fracture energies for both initiation criteria based on the limited data on graphene interface characterization in literature. For crack path selection based on which interface experiences damage first, both normal and shear strengths are important in the maximum stress initiation criterion while the normal strength is more important in the case of quadratic stress initiation.

In the next chapter, finite element simulations for thin film transfer are presented where the thickness of the printable film ranges between 10-50 μm instead of being atomically thin. The significance of interfacial defects and material properties are also explored in addition to interface properties.

Chapter 5: Interface Mechanics of Thin Film Transfer Printing

Competing fracture in the transfer of thin films from a relatively rigid host substrate to a flexible polymer substrate is studied using finite element simulations with cohesive zone models. Cohesive zone models for delamination based on traction-separation relations with a maximum stress criterion for damage initiation and mode-independent fracture energy for complete separation are explored to identify important parameters that affect transfer printing. Successful transfer of a thin film to a relatively soft polymer substrate from a stiffer substrate depends on relative crack lengths, interface strengths and fracture energies. Interface selection occurs where the mode-mix at the crack tip is predominantly due to normal stresses, despite the interface toughness being mode-independent. The observations and the fracture maps developed here predict the interface selection directly with material properties of the interfaces, substrates and films.

5.1 INTRODUCTION

Transfer printing is a fabrication technique for microelectronics and other applications where a thin film is transferred from a host substrate to a target substrate by taking advantage of the difference in adhesion between the thin layer and the two substrates. This technique has been studied for the case of layers a few microns thick [38, 40, 41] and has also been demonstrated to work for transferring two-dimensional (2D) materials like graphene [42]. Inorganic semiconductors like silicon [45, 46], GaAs, InP [47] and CdSe [48], metals such as gold [49], copper [50] and aluminum [51], carbon in the form of diamond [52], graphene [53, 130] and carbon nanotubes [54], MoS_2 [130], hexagonal boron nitride and few layer black phosphorus [131], organic materials [55-57], colloids [58] and biological materials [59, 60] can be transferred to substrates in the form of nanomembranes, nanoribbons, nanowires, thin films, self-assembled monolayers and

quantum dots. Flexible displays [48, 132], thin film photovoltaics [133] and artificial skin [63, 134, 135] are some of the exciting potential applications [136] in thin film flexible electronics. A thin film transfer printing schematic is shown in Fig. 5.1a where a thin film is transferred from a host substrate to a flexible target substrate. Fig. 5.1b shows a roll-to-roll transfer printing schematic for thin film transfer that can enable high throughput and lower costs of manufacturing devices.

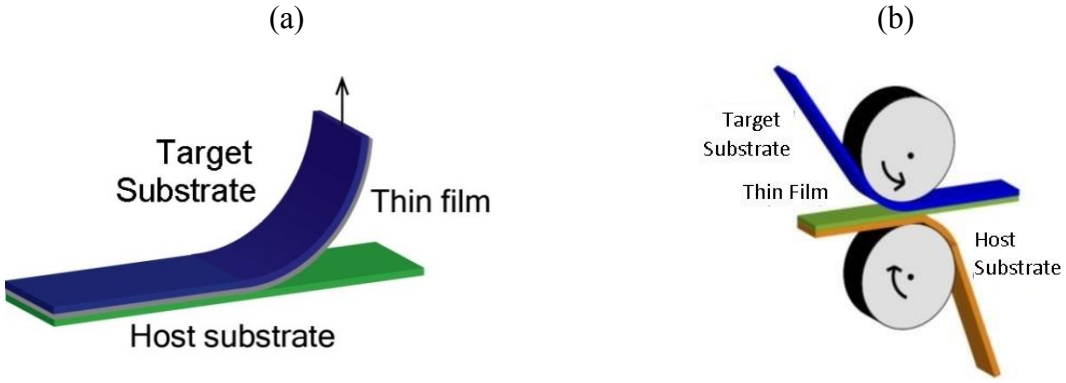

Figure 5.1: (a) Schematic diagram of transfer printing of thin films, (b) roll-to-roll transfer schematic from a host substrate to a target flexible substrate.

Transfer of the film relies on the competing forces associated with fracture at the interfaces between the film/host substrate and the film/target substrate. The surfaces can be modified to control adhesion between different substrates using chemical, thermal and mechanical strategies and favor delamination at the desired interface. The delamination can be modeled as a crack initiation and propagation along the interfaces. Each interface has a characteristic toughness (or critical energy release rate) Γ_c and strength σ_0, which provide competing fracture pathways. When the energy release rate G at an interface crack tip is greater than its toughness Γ_c, the crack grows [62]. In the case of competing fracture in thin film transfer, a comparison of toughness and energy release rates at both interfaces is made to determine the crack path. For example, if $G_t / G_b > \Gamma_t / \Gamma_b$ then the

crack propagates along the top interface (here, the subscripts *t* and *b* are used for the top and bottom interfaces, respectively) [40]. Interface strength does not enter such considerations as they are based on linearly elastic fracture mechanics concepts. It does enter cohesive zone modelling and is explored in the paper.

There is relatively little fundamental understanding of crack propagation along neighboring interfaces. Transfer printing has many challenges such as obtaining strong adhesion between the thin film and the target substrate, ensuring uniform coverage of the transferred film on the target substrate, avoiding cracks and defects in the thin layer during transfer, and achieving high throughput transfer for industrial manufacturing. Understanding the parametric relations that control the adhesion properties and quantifying the effect of competing interface interactions, mode-mix and viscoelasticity in this technique can improve the current manufacturing processes for transfer printing of thin films.

Tucket et al. [40] developed a computational model based on linearly elastic fracture mechanics concepts to study the transfer printing system. They calculated energy release rates from contour integrals using finite element simulations. Their work highlighted the role of interfacial defects and differential fracture energies in determining the quality of transfer printing. They also varied the stiffness of the target substrate which showed that stiff substrates are not affected by adhesion energies as much as compliant substrates. Kim-Lee et al. [41] developed a model and performed experiments for printing with a soft elastomer stamp. They explored the effect of interface toughness, interface defects as well as stamp geometry and thin film thickness on the process.

In this paper the effects of interface toughness and defects, variations in thin film elastic modulus, thin film thickness, interface strengths and mode-mix are studied. Previous work is extended by considering nonlinear fracture mechanics where finite

element simulations are performed with interfaces being characterized by traction-separation relations as explained in section II. The results of varying material and geometric properties of the layers and interface properties are discussed in section III followed by conclusions in section IV on predicting which interface fractures based on the properties of the interfaces and the material properties.

5.2 METHOD

To study the effect of interface properties, elastic modulus of the thin film, thin film thickness and crack lengths on competing interface fracture in the transfer printing process, we use finite element simulations to model the process in ABAQUS®. The schematic for the model with boundary conditions is shown in Fig. 5.2, where the top layer is the target substrate, the black middle layer is the thin film to be delaminated and the bottom layer is the host substrate. There are two interfaces, the top interface between the target substrate and the thin film, and the bottom interface between the thin film and the host substrate. These interfaces are modeled using bilinear traction-separation relations in the simulations as explained in the next sub-section.

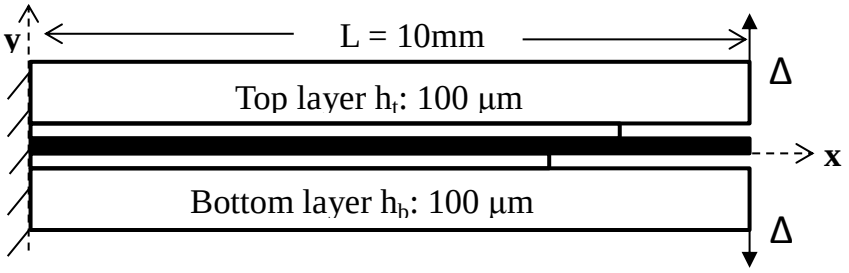

Figure 5.2: Model schematic of a thin film transfer system from a host substrate to a flexible polymer.

This delamination system potentially consists of 18 parameters (elastic moduli E_j, Poisson's ratios ν_j and thicknesses h_j of three materials, three properties of each interface

as per the characteristic traction separation relation chosen, applied end displacement Δ and initial crack lengths at the interfaces L_j), which makes a full parametric study out of scope for this paper. Here we report interesting characteristics observed by varying nine parameters - elastic moduli of the three materials, thickness of the printable film, two properties of each interface and the crack length at the bottom interface.

5.2.1 Cohesive Zone Model and Finite Element Simulations

The bi-linear cohesive zone model is used for both interfaces. The extent of damage at an interface is quantified with a damage parameter D (or SDEG in ABAQUS®) which varies between 0 (no damage) and 1 (complete damage) for each interface and is expressed as $D = \delta_c(\delta - \delta_0)/(\delta(\delta_c - \delta_0))$. Since transfer printing can have significant mode-mix at the crack tips, tractions in both normal and shear directions have to be considered. For the purpose of this study, a maximum stress initiation criterion is used. Interface damage is initiated when $\max\{\sigma/\sigma_0, \tau/\tau_0\} = 1$, where σ_0 and τ_0 are the normal and shear interface strengths. We use $\sigma_0 = \tau_0$ for the parameter space in this study.

Cohesive elements are used for the interfaces and 2D plane strain continuum reduced integration (CPE4R) elements are used for the polymer and copper substrates in ABAQUS®. A rigid beam type multi-point constraint is defined at the edges of the substrates to prescribe the displacement boundary conditions. A mesh size of 10 μm is used to ensure a sufficient number of cohesive elements in the damage zone for numerical convergence. The elastic moduli of the layers, interface strengths, interface fracture energies, thin film thickness and crack lengths are varied as listed in Table 5.1 to understand their effect on interface selection for crack growth to identify the parameter space for successful transfer printing.

5.3 RESULTS

To identify the effect of crack length and traction-separation relations independent of the material stiffness, simulations are performed with equal elastic modulus of all three layers ($E_t = E_f = E_b = 2500$ MPa). The crack length at the top interface L_t is kept constant while the crack length at the bottom interface L_b and thin film thickness h_f is varied as mentioned in Table 5.1.

Table 5.1: Material properties and interface properties for transfer printing simulations.

	Top	**Bottom**	**Thin Film**
Layer Elastic Modulus (MPa)	2500,5000,7500	2500,10000,50000,110000	2500,5000,10000
Layer thickness (mm)	0.1	0.1	0.01,0.02,0.05
Crack Length (mm)	1	0.4-2	-
Interface Strength (MPa)	0.5,1	0.5,1	-
Interface Fracture Energy (J/m^2)	3,4,6	3,4,6	-

The results show that the interface with the longer crack continues to fracture at steady state irrespective of the traction-separation relation specified even when both interfaces are significantly damaged (SDEG>1). This is because the energy release rate is greater at interfaces with longer cracks. However, for equal initial crack lengths ($L_b = L_t =$ 1 mm), the interface with the lower strength fractures. These results are depicted in Fig. 5.3a with an ABAQUS screenshot for a film of 20 μm thickness as well as the fracture map in Fig. 5.3b, which is similar to the quality map presented by Tucker et al. [40] for a stiff polymer, gold and silicon system.

(a)

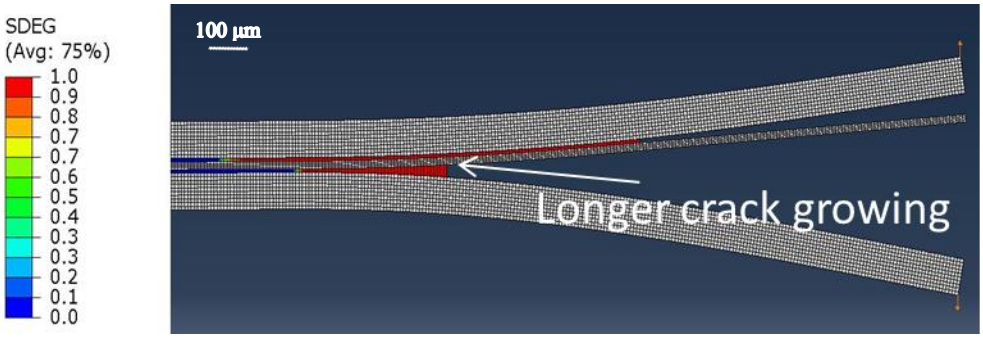

(b)

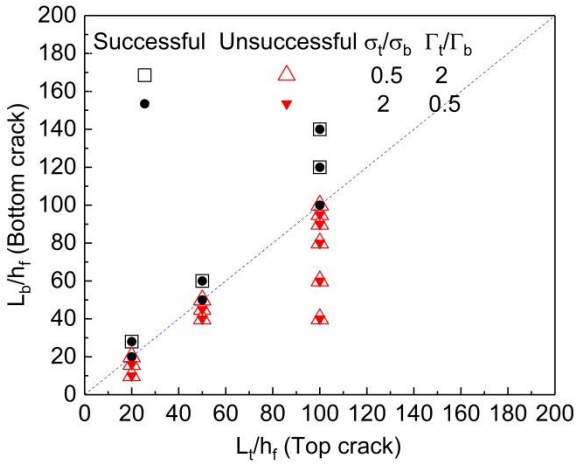

Figure 5.3: (a) ABAQUS® screenshot of a simulation with L_t/L_b = 0.83, h=20 μm, σ_t/σ_b=0.5 and Γ_t/Γ_b=2 where the bottom interface (which has a longer initial crack) fractures. (b) A fracture map showing regions of successful (bottom interface fracture) and unsuccessful (top interface fracture) transfer printing based on initial crack lengths, film thickness and traction-separation relations. The two regions are separated by the line L_t/L_b = 1.

These results remain unchanged for varying stiffness od the thin film and suggest that relative crack lengths are more important than thin film stiffness or traction-separation relations of similar order of magnitudes when E_t/E_b= 1. Interface strengths become important when initial crack lengths are equal and fracture energies play a role

when both interfaces also have equal strength as shown in Fig. 5.4. Here, crack propagates along the top interface when its strength is lower (σ_t/σ_b <1) while the bottom interface fractures for σ_t/σ_b >1.

Next we consider the case of a polymer, thin film, and stiff host substrate where E_t =2500 MPa, E_f = 2500 MPa and E_b = 110 GPa. The fracture map for this case is shown in Fig. 5.5. The energy release rate at each interface changes as a function of elastic moduli, crack length and thickness of the printable thin film [40]. Compared to the simulations with $E_t = E_f = E_b$ = 2500 MPa, here the host substrate is much stiffer and for this reason, a longer bottom crack is required when transferring thick films significantly changing the fracture map.

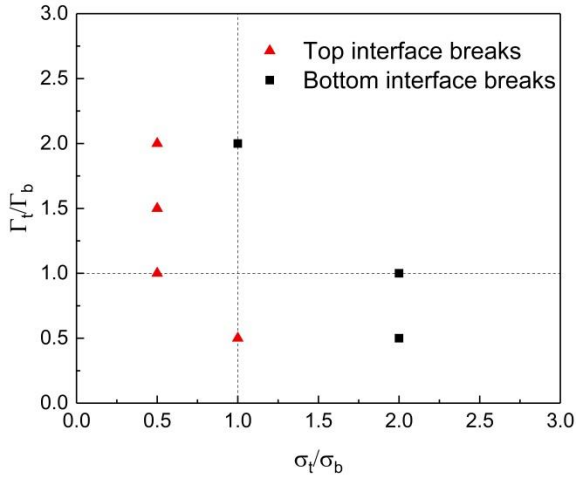

Figure 5.4: Fracture map for $E_t = E_f = E_b$ = 2500 MPa and L_t/L_b = 1 comparing results for varying ratios of strengths and fracture energies. Variation in h had no effect. When σ_t and σ_b have different values the interface with lower strength breaks. Otherwise, the interface with lower fracture energy breaks.

In addition to the host substrate elastic modulus, the target substrate stiffness also affects transfer printing. It has been shown previously [40, 41] that the energy release rate for the target substrate/thin film interface remains constant over a range of L_t/h values for

stiff target substrates whereas the energy release rate increases with increasing L_t/h for softer target substrates.

Our simulations suggest that the fracture map also changes with variation in thin film elastic modulus E_f. With increasing elastic modulus of the thin film, the fracture is eventually dominated by fracture energy. For 10 μm thin films, this turning point from crack length dominated interface selection to fracture energy driven selection occurs at E_f =10 GPa. In this case as well, variations in the interface strength have no effect on the fracture map.

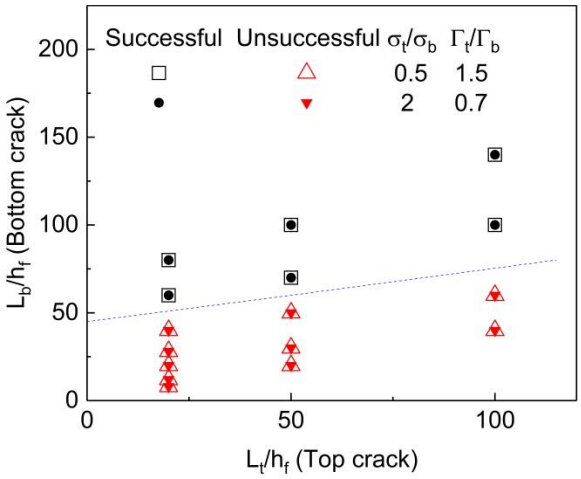

Figure 5.5: A fracture map showing regions of successful (bottom interface fracture) and unsuccessful (top interface fracture) transfer printing for a polymer target substrate (E_t =2500 MPa) and stiff host substrate (E_b = 110 GPa).

While results indicate fracture energy driven crack path selection in stiff films for the entire range of crack length ratios simulated, we observe some cases where the large difference in crack lengths leads to significant damage growth in both interfaces and simulations eventually fail to converge. Fig. 5.6 shows one such example where discontinuous damage zones develop in an interface and a situation where both interfaces

are equally likely to fracture arises. This leads to an unsteady state and the simulation aborts. In the case shown in Fig. 5.6, E_t =2500 MPa, E_f = 110 GPa, E_b = 110 GPa, h_f=0.01mm, Γ_t/Γ_b = 0.7, σ_t/σ_b = 2 and L_t/L_b = 0.5. The crack grows at the top interface as expected but convergence failure occurs halfway through the simulation. As the ratio of crack lengths is increased (L_t/L_b = 0.71,0.83, 2.5), the top interface crack propagates longer and the simulation converges. Systems that exhibit similar damage profiles as Fig. 5.6 would likely suffer from discontinuous transfer printing and poor coverage as the layers are displaced further apart. Displacement boundary conditions will have to be identified precisely to avoid operating in this region.

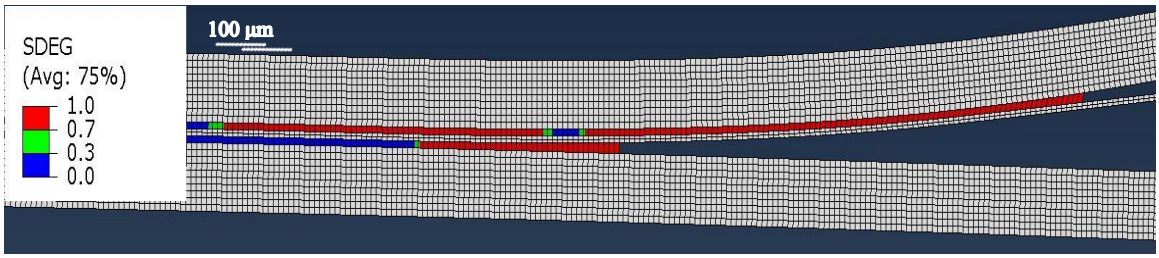

Figure 5.6: ABAQUS® simulation screenshot of the damage zone profile for a film thickness of 10 µm.

The effect of the thickness of the printable layer is studied by varying the thin film thickness between 10-50 µm. We observe a dependence of interface selection on film thickness for only a singular case with E_t =2500 MPa, E_f = 2500 MPa, E_b = 110 GPa, Γ_t/Γ_b = 0.7, σ_t/σ_b = 2 and L_t/L_b = 1. As shown in Figs. 5.7 a-b, crack grows at the bottom interface for a 10 µm film whereas the top interface fractures for a 50 µm thin film. In other words, making the film thicker changed the system from a strength driven to a fracture energy driven crack path selection. For the prescribed traction-separation relations and film thicknesses in our case, this implies an unsuccessful transfer for thicker

films. Kim-Lee et al. [41] performed simulations and experiments using silicon and glass substrates and they reported an increase in transfer printing yield by increasing the thickness of the printable layer to 3μm but lacked data on interfacial properties.

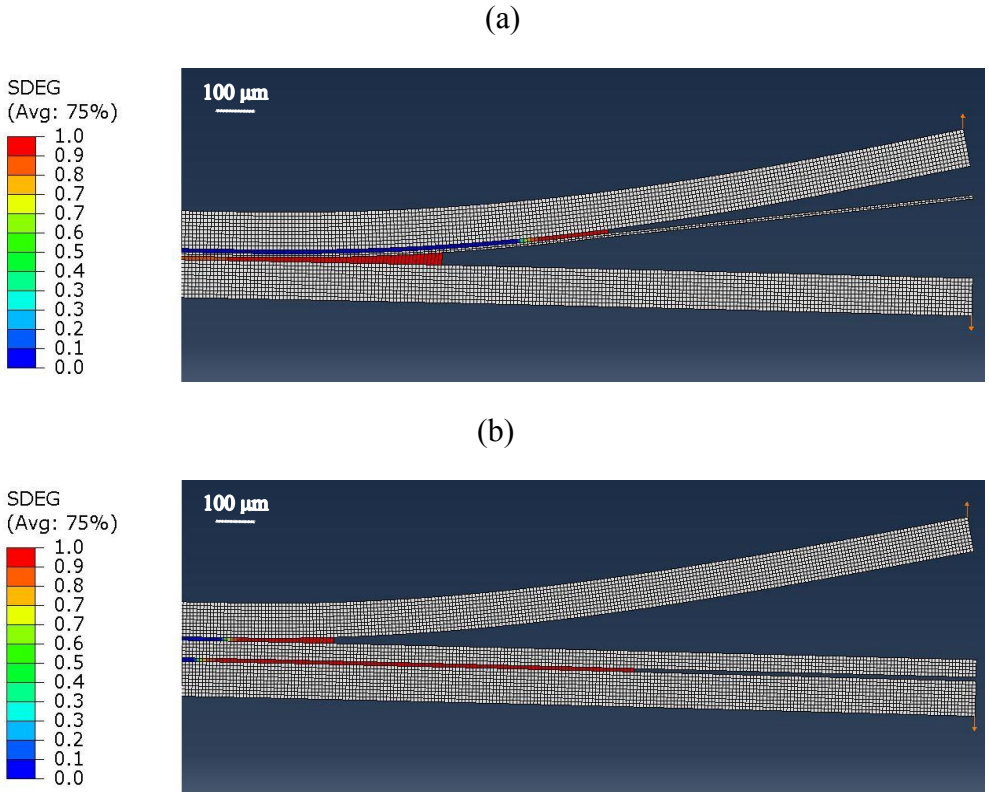

Figure 5.7: (a) ABAQUS® simulation screenshot of crack propagation at the bottom interface for film thickness of 10 μm, (b) ABAQUS® simulation screenshot of crack propagation at the top interface for film thickness of 50 μm.

The effects of varying E_f and h_f suggest the existence of a critical combination of these two parameters that defines the boundary between fracture toughness driven and strength driven crack path selection. The bending stiffness $E_f h_f^3$ would seem to be a good choice to predict this transition. However, it did not capture the trend.

The results discussed so far have been specific interesting cases. Results from more than a hundred simulations yielded a strong correlation between the fracturing

interface and crack tip mode-mix (defined as $\Psi = \tan^{-1}(\tau/\sigma)$). The fracture energy in all the simulations is independent of mode-mix which is why the observed correlation is surprising. Figs 5.8 a-b show the crack tip mode-mix when damage begins and when crack grows at an interface, respectively. No trend is seen during damage initiation but at steady state, the interface with the lower crack tip mode-mix is the interface that fractures. However, no universal power law relationship of crack growth with elastic moduli, film thickness or crack length ratio is observed.

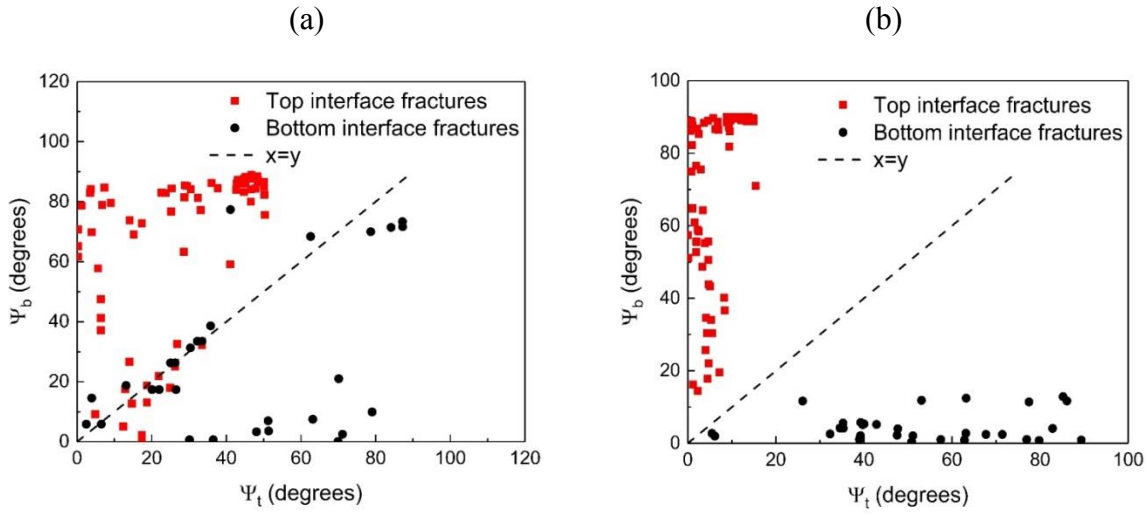

Figure 5.8: (a) Crack tip mode-mix at both interfaces when damage initiates in the system, (b) Crack tip mode-mix at both interfaces when crack grows steadily at an interface.

5.4 CONCLUSIONS

Transfer printing is simulated for varying material properties and interface properties to identify regions of successful thin film transfer. For compliant thin films and interfaces with cracks, the relative crack length ratio is extremely important in the transfer process. For equal crack lengths, interface strength is the determining factor and if the strengths are equal, then fracture toughness of the interface comes into play. This

result is consistent with observations for the transfer of a 2D material. If the transferred layer has a high elastic modulus, then fracture toughness is the most important parameter in crack path selection. For the transfer of such stiff films, large end displacement conditions combined with unfavorable crack length ratios can lead to significant damage in both interfaces and hence, non-uniform transfer. Increasing the thickness of the printable layer also pushes the system towards a fracture energy driven process. A strong correlation is observed between the crack tip mode-mix and the interface selection for crack growth despite fracture energy being mode-independent in the simulations. The interface fracturing in steady state always has a lower mode-mix than the other interface in our simulations. Future work in this area could include exploring larger variations in interface strengths and target substrates softer than 2500 MPa. More simulations are required to clearly understand the effect of all material and interfacial properties on the energy release rate.

Chapter 6: Concluding Remarks

In this dissertation, models and simulations for delamination in dry transfer printing are created. The system potentially depends on nineteen or more parameters, and there are gaps in existing studies about the interplay between those parameters and their effect on crack growth. The knowledge gaps addressed in this work include the effect of interface strengths, fracture energies and mode-mix on competing fracture as well as quantifying the dependence of steady state crack propagation on material and interface properties. Computationally, the conventional method of finite element simulations with software packages such as ABAQUS® has several issues with convergence, equilibrium and run time when using interface elements. For this reason, 10,000 times faster and robust finite difference models are developed to simulate interface fracture in transfer printing.

Finite element simulations and beam theory models are developed to determine the quantitative effect of material and interface properties on crack propagation at an interface in mode I and mixed-mode loading. Initially, single interface fracture is simulated to explore the possibility of semi-analytical solutions for the differential equations describing mode I and mixed-mode fracture. The models are validated with experiments and ABAQUS® simulations. Scaling analysis and data fitting yield simple algebraic equations to calculate load, crack length, damage zone length, end rotation and mode-mix from material and interfacial properties. Next, models are developed to simulate graphene transfer from a growth substrate (copper) to a flexible polymer substrate. For the same interfacial defect length at both interfaces, graphene transfer is found to be a function of interface strengths. Fracture maps are developed showing the regions of successful graphene transfer based on relative interfacial properties. The

transfer of few microns thick films is modeled with different interfacial defects at the two interfaces to understand the effect of film thickness and defects. The parameter driving the transfer process varies based on the elastic modulus and thickness of the thin film. The main findings from this study and future directions are described below.

6.1 Characteristic Scaling Equations For Softening Interactions Between Beams

The simplest case to start modeling interface fracture is a double-cantilever beam with cohesive interactions at the contacting surfaces. In mode I loading, only normal tractions exist at the interface. A bi-linear cohesive zone model is used to describe the interface interactions and the beam deflections are given by a fourth order differential equation derived from force and moment balances using classical beam theory. In the case of a bilinear traction-separation relation, the interface can have three regions depending on the extent of damage - the elastic region, the damage region and the cracked region. The system of equations and boundary conditions to model crack growth in this 1-D setup are identified and solved using a shooting method. A 2-D finite element model is also developed in ABAQUS® to validate the beam theory model. The model is experimentally validated by comparing simulation results to the load-displacement data from a wedge test of hydroxylated silicon surfaces.

A parametric analysis is performed to identify relationships between the traction-separation parameters and steady state crack growth. The changes in load, crack length and damage zone length with increasing end displacement exhibit expected behavior. The three quantities are also observed to be strongly dependent on interface strength and critical displacement. However, no dependence is seen on the interface stiffness. The steady state load, crack length, damage zone length and elastic zone length are fully

expressed with four dimensionless parameters: $\delta_0/\Delta, \delta_c/\Delta, h/\Delta, \sigma_0/E^*$ described in chapter 2. The algebraic equations obtained through scaling analysis for these parameters significantly reduce the complexity of modeling crack growth at an interface and quantify the parametric dependences.

6.2 A COHESIVE ZONE MODEL AND SCALING ANALYSIS FOR MIXED-MODE INTERFACIAL FRACTURE

There is always some mode-mix when two dissimilar materials are separated by interface fracture. The purely mode I double cantilever model does not account for shear tractions and hence, another model is developed to understand the effect of mode-mix on crack growth. A beam on a rigid substrate is modeled with finite element simulations in ABAQUS® and a finite difference beam theory model in MATLAB®. We consider a bilinear traction-separation relation for the interface with stiffness K in both normal and tangential directions, effective displacement δ_0 for damage initiation and effective displacement δ_c for damage completion. The beam theory model is considerably faster than finite element simulations and a decent agreement is observed between the two models. Expected trends such as constant mode-mix and fracture energy at steady state are observed further validating the simpler beam theory model.

A parametric analysis is performed to quantify the dependence of load, crack length, end rotation, damage zone length and mode-mix on material and interface properties. Scaling analysis yields power law equations for load, end rotation and crack length at steady state. However, data fitting is required to obtain equations for damage zone length and mode-mix. Some similarities are observed between the mode I and mixed-mode scaling equations.

6.3 A Parametric Cohesive Zone Beam Theory Analysis of Mixed-mode Graphene Transfer

2D materials are an important class of materials useful in manufacturing flexible electronics. After exploring and developing models for single interface fracture, models are developed to understand competing fracture when transfer printing 2D materials like graphene from their growth substrate onto a flexible substrate. The model includes a stiff growth substrate (copper), two interfaces - graphene/copper and polymer/graphene and a flexible polymer as the target substrate. The fracture is simulated with mode I dominant as well as mixed-mode fracture equations. Two damage initiation criteria are explored - maximum stress and quadratic stress damage initiation. Finite element simulations using cohesive elements in ABAQUS® have several issues with equilibrium and convergence when modeling competing fracture. Beam theory models are found to be more robust and 10,000 times faster.

The main assumption while deciding crack path selection in the model is that the interface that experiences damage initiation first is the interface that cracks. Compliant target substrates lead to significant damage in both interfaces which is undesirable for transferring graphene uniformly onto the polymer. Three equations constraining the interface stiffness are identified to ensure real solutions in the elastic zone of the interfaces. However, variation in stiffness within the prescribed bounds does not have any effect on steady state crack growth. The most important parameter that drives the interface selection is found to be interface strength and not fracture energy. This is true for both damage initiation criteria explored in our research. Effects of fracture energy are seen when the dimensionless length scale $E^{*}\Gamma/\sigma^{2}l_{0}$ has a value smaller than 1 as described in chapter 4.

The maximum stress damage initiation criterion leads to a predominantly mode I fracture with a mode-mix of -10^0 at the crack tip. A beam theory model with only normal tractions at the interface shows a reasonable agreement with 2D ABAQUS simulation results. A fracture map is developed to show the regions of successful graphene transfer where strength of the graphene-copper interface is lower than the polymer-graphene interface strength. The scaling analysis equations from mode I double cantilever beam model fit the graphene transfer data perfectly.

The quadratic stress damage initiation criterion leads to a mixed-mode fracture condition with a mode-mix of -33^0 at the crack tip. ABAQUS® simulations for this set of simulations do not show equilibrium at the interface. However, the beam theory model works well and yields a strength driven fracture map. A user element based ABAQUS model is simulated to validate the beam theory model. The fracture map shows the interplay between the interface strengths in the normal and shear directions to identify regions of successful vs. unsuccessful graphene transfer. A parametric analysis is performed and data fitting is used to obtain power law equations for load, crack length, end rotation, damage zone length and mode-mix. These power laws are found to be significantly different than the equations for mode I dominant fracture. The displacement for damage initiation is found to be a stronger function of normal strength than shear strength. In summary, for competing fracture where both interfaces have the same interfacial defects, it is best to have favorable interface strengths in both normal and shear directions for the graphene-polymer interface to ensure successful transfer. For other cases, it is possible to initiate damage in the desired interface but chances of eventually damaging both interfaces are high.

6.4 Interface Mechanics of Thin Film Transfer Printing

In addition to 2D materials, a few microns thick films of gold, copper, inorganic semiconductors can also be transfer printed to manufacture electronic devices. Models are developed for thin film transfer in ABAQUS® to study competing fracture and identify the desirable interface and polymer properties for successful transfer. This model also provides an opportunity to understand the effect of interfacial edge defects and properties of the thin film. Varying the elastic moduli of the three layers in the model, traction-separation relations of the two interfaces and thin film thickness give insight into the different regimes of transfer printing.

The results show that for very thin or compliant films, interface defects (or initial cracks) are the most important parameter in crack path selection. The interface with the larger interfacial crack fractured in most cases. The critical ratio of the two interfacial defects changes based on the elastic moduli of the three layers and leads to different fracture maps. Traction-separation parameters such as strength and fracture energy when varied by a factor of two do not have any effect on these fracture maps. However, having a longer interfacial crack isn't enough. The fracture energies of the interfaces and end displacements should be such that the other interface does not undergo too much damage or else both interfaces will be likely to fracture leading to non-uniform or unsuccessful transfer. In the case of equal interfacial defects, the interface strength is the deciding factor for crack propagation. The interface with the lower strength breaks irrespective of the fracture energy as has been observed for 2D materials. However, for stiff (E >10GPa) or thicker films, the relative fracture energies determine the interface of crack growth.

Over a hundred simulations are analyzed to identify a combination of parameters to identify the crack path in competing fracture. One striking correlation is observed between mode-mix and interface selection. Even though the fracture energies used in the

cohesive zone model are mode-independent, the interface that fractures always has a lower mode-mix at the crack tip.

The results of this dissertation for transfer printing of 2D materials and thin films are the following:

- Transfer of graphene (or other molecularly thin films) relies on the relative strengths of the graphene-copper and polymer-graphene interfaces rather than fracture energies.
- ABAQUS® cohesive elements have their limitations in simulating mixed-mode competing fracture. They are time consuming and fail to converge or obtain stress equilibrium in multiple cases. Beam theory models are much faster and robust in comparison.
- Algebraic equations to calculate load, crack length, damage zone length, end rotation and mode-mix have been developed for single interface and competing interface fracture, eliminating the need of solving the system of differential equations for certain configurations.
- For compliant films or very thin films, interfacial edge defects in the form of initial crack lengths are the most important factor for determining the success of transfer printing.
- For stiff or thick films, crack path selection depends on the relative fracture energies of the interfaces. However, for a highly unfavorable crack length ratio, large end displacements could cause significant damage in the other interface. Hence, there has to be a balance between the relative interfacial defects, fracture energy and end displacement for uniform transfer.

- A strong correlation between crack-tip mode-mix and interface selection exists at steady state. The fracturing interface always has lower mode-mix.

6.5 Future Work

6.5.1 Effect of Tension and Peel Angles on Transfer Printing

In the models developed so far to study transfer printing, tension in the substrates has been neglected. However, during roll-to-roll (R2R) transfer of materials, there is tension in the substrate layers. To understand the effect of this tension on material transfer, a combination of beam theory and membrane theory will have to be used to model the system. The model schematic is shown in Fig. 6.1. Since fracture occurs in a small zone (highlighted in purple in the figure), developing a model for that small region with end displacements and tensions along the layers would be useful to study the transfer printing process.

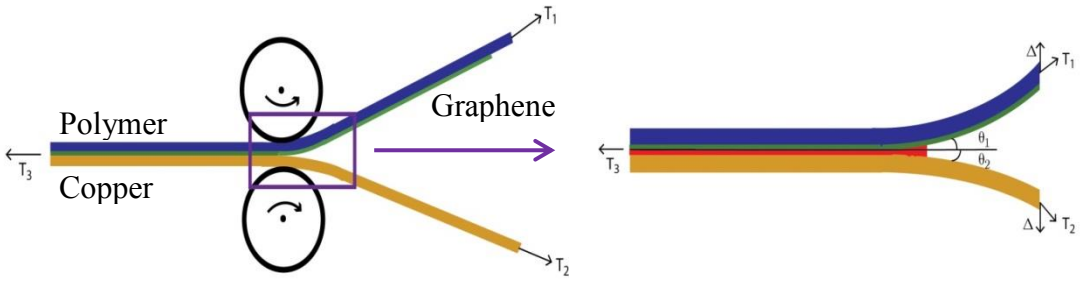

Figure 6.1: Schematic of the roll-to-roll graphene transfer process also showing the zoomed in fracture zone (with damaged interface in red) which can be modeled for studying the effect of tension and peel angles.

The simplified equation for a beam with small out-of-plane deformations and significant in-plane loading can be written as:

$$\frac{Eh^3}{12(1-\upsilon^2)}\frac{d^4w}{dx^4}-T_x\frac{d^2w}{dx^2}=-q, \tag{6.1}$$

where E, h, υ are properties of the beam, w is the out-of-plane deflection, T_x is the in-plane loading and q is the distributed traction at the interface. Non-dimensionalizing the equation by replacing $w=\bar{w}\Delta, x=\bar{x}L, T_x=T_0\bar{T}$ and $q=q_0\bar{q}$ gives:

$$\frac{Eh^3\Delta}{12(1-\upsilon^2)q_0L^4}\frac{d^4\bar{w}}{d\bar{x}^4}-\frac{T_0\Delta}{q_0L^2}\bar{T}\frac{d^2\bar{w}}{d\bar{x}^2}=-\bar{q}. \tag{6.2}$$

For a polymer such as polyimide (PI) or polyethylene terephthalate (PET), $E \sim O(10^9)$, $h \sim O(10^{-4})$, $\Delta \sim O(10^{-4})$, $q_0 \sim O(1)$, $L \sim O(10^{-1})$ and $T_0 \sim O(10^2)$ which makes the first term $O(10^{-4})$ and the second term is $O(1)$. For the copper foil with $E \sim O(10^{11})$, the first term is $O(10^{-2})$ and second term is $O(1)$. This indicates the importance of including the effect of tension for both substrates.

Graphene is also highly sensitive to tensile strain. For CVD graphene transferred using a roll-to-roll process, the film speed and roller diameter have a significantly effect on the tensile strain. Xin et al. [39] transferred CVD graphene onto PET/EVA films and observed cracks on the graphene surface for low film speed and small roller diameters which create a larger strain. Na et al. [137] reported the threshold strain for graphene cracking to be 0.5%. Before cracks appear, sliding could also happen between the graphene and the polymer layer. Depending on the polymer used and its thickness, the critical elongation for sliding can vary. For these reasons, modeling the effect of tension and controlling it in the R2R process is important to enable successful, uniform transfer of graphene onto a polymer layer.

6.5.2 Use of Experimentally Characterized Traction-Separation Relations in the Models

The parametric analysis performed on the models is based on the graphene-copper traction separation relation measured by Na et al. [37] and Xin et al. [39] But the interface properties for the polymer-graphene or polymer-thin film interfaces can vary significantly from the graphene-copper interactions. Asymmetric strengths in the normal and shear directions can also have a huge impact on the transfer characteristics. Thus, it is important to simulate these models with experimentally verified interface properties for different materials to truly identify the parameter space for successful transfer of thin films. The data on interface properties is very limited at this moment and future work on characterizing interfaces will be useful in developing and optimizing the transfer process.

References

1. Gupta, A., T. Sakthivel, and S. Seal, *Recent development in 2D materials beyond graphene.* Progress in Materials Science, 2015. **73**: p. 44-126.
2. Geim, A.K. and K.S. Novoselov, *The rise of graphene.* Nat Mater, 2007. **6**(3): p. 183-191.
3. Zhu, Y., et al., *Graphene and Graphene Oxide: Synthesis, Properties, and Applications.* Advanced Materials, 2010. **22**(35): p. 3906-3924.
4. Novoselov, K.S., et al., *Electric field effect in atomically thin carbon films.* Science, 2004. **306**(5696): p. 666-669.
5. Novoselov, K.S., et al., *Room-temperature quantum hall effect in graphene.* Science, 2007. **315**(5817): p. 1379.
6. Novoselov, K.S., et al., *A roadmap for graphene.* Nature, 2012. **490**(7419): p. 192-200.
7. Kim, K.S., et al., *Large-scale pattern growth of graphene films for stretchable transparent electrodes.* Nature, 2009. **457**(7230): p. 706-710.
8. Ferrari, A.C., et al., *Science and technology roadmap for graphene, related two-dimensional crystals, and hybrid systems.* Nanoscale, 2015. **7**(11): p. 4598-4810.
9. Choi, W., et al., *Synthesis of graphene and its applications: a review.* Critical Reviews in Solid State and Materials Sciences, 2010. **35**(1): p. 52-71.
10. Schedin, F., et al., *Detection of individual gas molecules adsorbed on graphene.* Nat Mater, 2007. **6**(9): p. 652-655.
11. Fowler, J.D., et al., *Practical chemical sensors from chemically derived graphene.* ACS Nano, 2009. **3**(2): p. 301-306.
12. Shan, C., et al., *Direct electrochemistry of glucose oxidase and biosensing for glucose based on graphene.* Analytical Chemistry, 2009. **81**(6): p. 2378-2382.
13. Alwarappan, S., et al., *Probing the electrochemical properties of graphene nanosheets for biosensing applications.* The Journal of Physical Chemistry C, 2009. **113**(20): p. 8853-8857.
14. Nayak, T.R., et al., *Graphene for controlled and accelerated osteogenic differentiation of human mesenchymal stem cells.* ACS Nano, 2011. **5**(6): p. 4670-4678.
15. Nair, R.R., et al., *Graphene as a transparent conductive support for studying biological molecules by transmission electron microscopy.* Applied Physics Letters, 2010. **97**(15): p. 153102.
16. *Graphene electronics market - global industry analysis, size, share, growth, trends, and forecast, 2015 - 2025*. 2015, Transparency Market Research.
17. Ago, H., *CVD growth of high-quality single-layer graphene*, in *Frontiers of Graphene and Carbon Nanotubes*. 2015.
18. Edwards, R.S. and K.S. Coleman, *Graphene synthesis: relationship to applications.* Nanoscale, 2013. **5**(1): p. 38-51.

19. Li, X., et al., *Large-area synthesis of high-quality and uniform graphene films on copper foils.* Science, 2009. **324**(5932): p. 1312-1314.
20. Song, J., et al., *A general method for transferring graphene onto soft surfaces.* Nat Nano, 2013. **8**(5): p. 356-362.
21. Campos, N., et al., *Surface treatment of polyimide substrates for the transfer and multitransfer of graphene films.* Applied Surface Science, 2015. **349**: p. 101-107.
22. Unarunotai, S., et al., *Transfer of graphene layers grown on SiC wafers to other substrates and their integration into field effect transistors.* Applied Physics Letters, 2009. **95**(20): p. -.
23. Suk, J.W., et al., *Transfer of CVD-grown monolayer graphene onto arbitrary substrates.* ACS Nano, 2011. **5**(9): p. 6916-6924.
24. Lee, Y., et al., *Wafer-scale synthesis and transfer of graphene films.* Nano Letters, 2010. **10**(2): p. 490-493.
25. Gorantla, S., et al., *A universal transfer route for graphene.* Nanoscale, 2014. **6**(2): p. 889-896.
26. Li, X., et al., *Transfer of large-area graphene films for high-performance transparent conductive electrodes.* Nano Letters, 2009. **9**(12): p. 4359-4363.
27. Kang, J., et al., *Efficient transfer of large-area graphene films onto rigid substrates by hot pressing.* ACS Nano, 2012. **6**(6): p. 5360-5365.
28. Bae, S., et al., *Roll-to-roll production of 30-inch graphene films for transparent electrodes.* Nat Nano, 2010. **5**(8): p. 574-578.
29. Caldwell, J.D., et al., *Technique for the dry transfer of epitaxial graphene onto arbitrary substrates.* ACS Nano, 2010. **4**(2): p. 1108-1114.
30. Wang, Y., et al., *Electrochemical delamination of CVD-grown graphene film: toward the recyclable use of copper catalyst.* ACS Nano, 2011. **5**(12): p. 9927-9933.
31. Gao, L., et al., *Repeated growth and bubbling transfer of graphene with millimetre-size single-crystal grains using platinum.* Nat Commun, 2012. **3**: p. 699.
32. Wang, X., et al., *Direct delamination of graphene for high-performance plastic electronics.* Small, 2014. **10**(4): p. 694-698.
33. Kang, J., et al., *Graphene transfer: key for applications.* Nanoscale, 2012. **4**(18): p. 5527-5537.
34. Yoon, T., et al., *Direct measurement of adhesion energy of monolayer graphene as-grown on copper and its application to renewable transfer process.* Nano Letters, 2012. **12**(3): p. 1448-1452.
35. Kwanghyun, Y., et al., *Direct physical exfoliation of few-layer graphene from graphite grown on a nickel foil using polydimethylsiloxane with tunable elasticity and adhesion.* Nanotechnology, 2013. **24**(20): p. 205302.
36. Lock, E.H., et al., *High-quality uniform dry transfer of graphene to polymers.* Nano Letters, 2011. **12**(1): p. 102-107.
37. Na, S.R., et al., *Selective mechanical transfer of graphene from seed copper foil using rate effects.* ACS Nano, 2015. **9**(2): p. 1325-1335.

38. Carlson, A., et al., *Transfer printing techniques for materials assembly and micro/nanodevice fabrication.* Advanced Materials, 2012. **24**(39): p. 5284-5318.
39. Xin, H., et al., *Roll-to-roll mechanical peeling for dry transfer of chemical vapor deposition graphene.* Journal of Micro and Nano-Manufacturing, 2018.
40. Tucker, M.B., D.R. Hines, and T. Li, *A quality map of transfer printing.* Journal of Applied Physics, 2009. **106**(10): p. -.
41. Kim-Lee, H.-J., et al., *Interface mechanics of adhesiveless microtransfer printing processes.* Journal of Applied Physics, 2014. **115**(14): p. 143513.
42. Álvarez Rodríguez, P., et al., *Surface treatment of polyimide substrates for the transfer and multitransfer of graphene films.* Applied Surface Science, 2015. **107**: p. 101-107.
43. Xia, Y. and G.M. Whitesides, *Soft Lithography.* Angewandte Chemie International Edition, 1998. **37**(5): p. 550-575.
44. Kumar, A. and G.M. Whitesides, *Features of gold having micrometer to centimeter dimensions can be formed through a combination of stamping with an elastomeric stamp and an alkanethiol ''ink'' followed by chemical etching.* Applied Physics Letters, 1993. **63**(14): p. 2002-2004.
45. Menard, E., et al., *A printable form of silicon for high performance thin film transistors on plastic substrates.* Applied Physics Letters, 2004. **84**(26): p. 5398-5400.
46. Kawahara, A., H. Katsuki, and M. Egashira, *Fabrication of semiconductor oxide thick films by slide-off transfer printing and their NO2-sensing properties.* Sensors and Actuators B: Chemical, 1998. **49**(3): p. 273-278.
47. Sun, Y. and J.A. Rogers, *Fabricating semiconductor nano/microwires and transfer printing ordered arrays of them onto plastic substrates.* Nano Letters, 2004. **4**(10): p. 1953-1959.
48. Kim, T.-H., et al., *Full-colour quantum dot displays fabricated by transfer printing.* Nature Photonics, 2011. **5**: p. 176.
49. Sanetra, N., et al., *Printing of highly integrated crossbar junctions.* Advanced Functional Materials, 2012. **22**(6): p. 1129-1135.
50. Felmet, K., Y.-L. Loo, and Y. Sun, *Patterning conductive copper by nanotransfer printing.* Applied Physics Letters, 2004. **85**(15): p. 3316-3318.
51. Lee, B.H., et al., *High-resolution patterning of aluminum thin films with a water-mediated transfer process.* Advanced Materials, 2007. **19**(13): p. 1714-1718.
52. Kim, T.-H., et al., *Printable, flexible, and stretchable forms of ultrananocrystalline diamond with applications in thermal management.* Advanced Materials, 2008. **20**(11): p. 2171-2176.
53. Liang, X., Z. Fu, and S.Y. Chou, *Graphene transistors fabricated via transfer-printing in device active-areas on large wafer.* Nano Letters, 2007. **7**(12): p. 3840-3844.
54. Meitl, M.A., et al., *Solution casting and transfer printing single-walled carbon nanotube films.* Nano Letters, 2004. **4**(9): p. 1643-1647.

55. Liu, S., et al., *Direct patterning of organic-thin-film-transistor arrays via a "dry-taping" approach.* Advanced Materials, 2009. **21**(12): p. 1266-1270.
56. Jiang, X., et al., *Polymer-on-polymer stamping: universal approaches to chemically patterned surfaces.* Langmuir, 2002. **18**(7): p. 2607-2615.
57. Yeom, J. and M.A. Shannon, *Detachment lithography of photosensitive polymers: a route to fabricating three-dimensional structures.* Advanced Functional Materials, 2010. **20**(2): p. 289-295.
58. Yao, J., et al., *Patterning colloidal crystals by lift-up soft lithography.* Advanced Materials, 2004. **16**(1): p. 81-84.
59. Thibault, C., et al., *Direct microcontact printing of oligonucleotides for biochip applications.* Journal of Nanobiotechnology, 2005. **3**(1): p. 7.
60. Lange, S.A., et al., *Microcontact printing of DNA molecules.* Analytical Chemistry, 2004. **76**(6): p. 1641-1647.
61. Chen, H., et al., *Experiments and viscoelastic analysis of peel test with patterned strips for applications to transfer printing.* Journal of the Mechanics and Physics of Solids, 2013. **61**(8): p. 1737-1752.
62. Feng, X., et al., *Competing fracture in kinetically controlled transfer printing.* Langmuir, 2007. **23**(25): p. 12555-12560.
63. Lee, W., et al., *Fabrication and characterization of a conformal skin-like electronic system for quantitative, cutaneous wound management.* Journal of Visualized Experiments : JoVE, 2015(103): p. 53037.
64. Cao, Q., et al., *Medium-scale carbon nanotube thin-film integrated circuits on flexible plastic substrates.* Nature, 2008. **454**: p. 495.
65. Kim, H.-s., et al., *Unusual strategies for using indium gallium nitride grown on silicon (111) for solid-state lighting.* Proceedings of the National Academy of Sciences, 2011. **108**(25): p. 10072-10077.
66. Anderson, T.L., *Fracture mechanics: fundamentals and applications*. Third ed. 2005, Boca Raton, Florida: CRC Press.
67. Irwin, G.R., *Onset of fast crack propagation in high strength steel and aluminium alloys.* Sagamore Research Conference Proceedings, 1956. **2**: p. 289-305.
68. Haixia, M., et al. *Initiation and propagation of interfacial delamination in integrated thin-film structures*. in *Thermal and Thermomechanical Phenomena in Electronic Systems (ITherm), 2010 12th IEEE Intersociety Conference on*. 2010.
69. Gowrishankar, S., et al., *A comparison of direct and iterative methods for determining traction-separation relations.* International Journal of Fracture, 2012. **177**(2): p. 109-128.
70. Dugdale, D.S., *Yielding of steel sheets containing slits.* Journal of the Mechanics and Physics of Solids, 1960. **8**(2): p. 100-104.
71. Needleman, A., *A continuum model for void nucleation by inclusion debonding.* Journal of Applied Mechanics, 1987. **54**(3): p. 525-531.
72. Mohammed, I. and K.M. Liechti, *Cohesive zone modeling of crack nucleation at bimaterial corners.* Journal of the Mechanics and Physics of Solids, 2000. **48**(4): p. 735-764.

73. Feraren, P. and H.M. Jensen, *Cohesive zone modelling of interface fracture near flaws in adhesive joints.* Engineering Fracture Mechanics, 2004. **71**(15): p. 2125-2142.
74. Li, S., et al., *Mixed-mode cohesive-zone models for fracture of an adhesively bonded polymer–matrix composite.* Engineering Fracture Mechanics, 2006. **73**(1): p. 64-78.
75. Na, S.R., et al., *Ultra long-range interactions between large area graphene and silicon.* ACS Nano, 2014. **8**(11): p. 11234-11242.
76. Li, S., J. Wang, and M.D. Thouless, *The effects of shear on delamination in layered materials.* Journal of the Mechanics and Physics of Solids, 2004. **52**(1): p. 193-214.
77. Li, S., et al., *Use of mode-I cohesive-zone models to describe the fracture of an adhesively-bonded polymer-matrix composite.* Composites Science and Technology, 2005. **65**(2): p. 281-293.
78. Parmigiani, J.P. and M.D. Thouless, *The effects of cohesive strength and toughness on mixed-mode delamination of beam-like geometries.* Engineering Fracture Mechanics, 2007. **74**(17): p. 2675-2699.
79. MarketsandMarkets, *Flexible electronics & circuit market by application (OLED & LCD display, printed sensor, battery, thin-film PV, OLED lighting), circuit structure (single-sided, multilayer, double-sided, rigid), vertical, and geography - global forecast to 2023*. 2018.
80. Prandtl, L., *Ein Gedankenmodell für den Zerreißvorgang spröder Körper.* ZAMM - Journal of Applied Mathematics and Mechanics / Zeitschrift für Angewandte Mathematik und Mechanik, 1933. **13**(2): p. 129-133.
81. Prandtl, L. and W.G. Knauss, *A thought model for the fracture of brittle solids.* International Journal of Fracture, 2011. **171**(2): p. 105-109.
82. Barenblatt, G.I., *The mathematical theory of equilibrium cracks in brittle fracture*, in *Advances in Applied Mechanics*. 1962, Elsevier. p. 55-129.
83. Kanninen, M.F., *An augmented double cantilever beam model for studying crack propagation and arrest.* International Journal of Fracture, 1973. **9**(1): p. 83-92.
84. Chow, C.L., C.W. Woo, and J.L. Sykes, *On the determination and application of cod to epoxy-bonded aluminium joints.* The Journal of Strain Analysis for Engineering Design, 1979. **14**(2): p. 37-42.
85. Williams, J.G., *End corrections for orthotropic DCB specimens.* Composites Science and Technology, 1989. **35**(4): p. 367-376.
86. Ungsuwarungsri, T. and W.G. Knauss, *The role of damage-softened material behavior in the fracture of composites and adhesives.* International Journal of Fracture, 1987. **35**(3): p. 221-241.
87. Stigh, U., *Damage and crack growth analysis of the double cantilever beam specimen.* International Journal of Fracture, 1988. **37**(1): p. R13-R18.
88. Williams, J.G. and H. Hadavinia, *Analytical solutions for cohesive zone models.* Journal of the Mechanics and Physics of Solids, 2002. **50**(4): p. 809-825.

89. Parvin, M. and W.G. Knauss, *Damage induced constitutive response of a thermoplastic related to composites and adhesive bonding.* International Journal of Fracture, 1990. **42**(1): p. 57-72.
90. Blaysat, B., et al., *Interface debonding characterization by image correlation integrated with Double Cantilever Beam kinematics.* International Journal of Solids and Structures, 2015.
91. Thouless, M.D. and Q.D. Yang, *A parametric study of the peel test.* International Journal of Adhesion and Adhesives, 2008. **28**(4–5): p. 176-184.
92. Na, S.R., D.A. Sarceno, and K.M. Liechti, *Ultra long-range interactions between silicon surfaces.* International Journal of Solids and Structures, 2016. **80**: p. 168-180.
93. Gialamas, P., et al., *Peeling of an elastic membrane tape adhered to a substrate by a uniform cohesive traction.* International Journal of Solids and Structures, 2014. **51**(18): p. 3003-3011.
94. Wei, Y. and J. Hutchinson, *Interface strength, work of adhesion and plasticity in the peel test.* International Journal of Fracture, 1998. **93**(1-4): p. 315-333.
95. Williams, M.L., *The stresses around a fault or crack in dissimilar media.* Bulletin of the Seismological Society of America, 1959. **49**(2): p. 199-204.
96. England, A.H., *A crack between dissimilar media.* Journal of Applied Mechanics, 1965. **32**(2): p. 400-402.
97. Comninou, M., *The interface crack.* Journal of Applied Mechanics, 1977. **44**(4): p. 631-636.
98. Rice, J.R., *Elastic fracture mechanics concepts for interfacial cracks.* Journal of Applied Mechanics, 1988. **55**(1): p. 98-103.
99. Hutchinson, J.W., M.E. Mear, and J.R. Rice, *Crack paralleling an interface between dissimilar materials.* Journal of Applied Mechanics, 1987. **54**(4): p. 828-832.
100. Sih, G.C. and J.R. Rice, *The bending of plates of dissimilar materials with cracks.* Journal of Applied Mechanics, 1964. **31**(3): p. 477-482.
101. Charalambides, P.G., et al., *A test specimen for determining the fracture resistance of bimaterial interfaces.* Journal of Applied Mechanics, 1989. **56**(1): p. 77-82.
102. Wang, J.S. and Z. Suo, *Experimental determination of interfacial toughness curves using Brazil-nut-sandwiches.* Acta Metallurgica et Materialia, 1990. **38**(7): p. 1279-1290.
103. Liechti, K.M. and Y.S. Chai, *Asymmetric shielding in interfacial fracture under in-plane shear.* Journal of Applied Mechanics, 1992. **59**(2): p. 295-304.
104. Sun, C.T. and C.J. Jih, *On strain energy release rates for interfacial cracks in bi-material media.* Engineering Fracture Mechanics, 1987. **28**(1): p. 13-20.
105. Lin, K.Y. and J.W. Mar, *Finite element analysis of stress intensity factors for cracks at a bi-material interface.* International Journal of Fracture, 1976. **12**(4): p. 521-531.

106. Kang Yong, L. and C. Hyung Jip, *Boundary element analysis of stress intensity factors for bimaterial interface cracks.* Engineering Fracture Mechanics, 1988. **29**(4): p. 461-472.
107. Smelser, R.E., *Evaluation of stress intensity factors for bimaterial bodies using numerical crack flank displacement data.* International Journal of Fracture, 1979. **15**(2): p. 135-143.
108. Ryoji, Y., et al., *Mixed mode fracture criteria for an interface crack.* Engineering Fracture Mechanics, 1994. **47**(3): p. 367-377.
109. Banks-Sills, L., N. Travitzky, and D. Ashkenazi, *Interface fracture properties of a bimaterial ceramic composite.* Mechanics of Materials, 2000. **32**(12): p. 711-722.
110. Evans, A.G. and J.W. Hutchinson, *Effects of non-planarity on the mixed mode fracture resistance of bimaterial interfaces.* Acta Metallurgica, 1989. **37**(3): p. 909-916.
111. Jain, S., et al., *Characteristic scaling equations for softening interactions between beams.* International Journal of Fracture, 2016. **201**(1): p. 1-9.
112. Wu, C., et al., *On determining mixed-mode traction–separation relations for interfaces.* International Journal of Fracture, 2016. **202**(1): p. 1-19.
113. Mukherjee, B., R.C. Batra, and D.A. Dillard, *Edge debonding in peeling of a thin flexible plate from an elastomer layer: a cohesive zone model analysis.* Journal of Applied Mechanics, 2016.
114. Yuan, H., et al., *Interfacial stress analysis of a thin plate bonded to a rigid substrate and subjected to inclined loading.* International Journal of Solids and Structures, 2007. **44**(16): p. 5247-5271.
115. Szekrényes, A. and J. Uj, *Beam and finite element analysis of quasi-unidirectional composite SLB and ELS specimens.* Composites Science and Technology, 2004. **64**(15): p. 2393-2406.
116. Park, K. and G.H. Paulino, *Cohesive zone models: a critical review of traction-separation relationships across fracture surfaces.* Applied Mechanics Reviews, 2013. **64**(6): p. 060802-060802-20.
117. de Morais, A.B., *Cohesive zone beam modelling of mixed-mode I–II delamination.* Composites Part A: Applied Science and Manufacturing, 2014. **64**: p. 124-131.
118. Jung Lee, M., et al., *Determination of cohesive parameters for a mixed-mode cohesive zone model.* International Journal of Adhesion and Adhesives, 2010. **30**(5): p. 322-328.
119. de Morais, A.B., *Simplified cohesive zone analysis of mixed-mode I–II delamination in composite beams.* Polymer Composites, 2013. **34**(11): p. 1901-1911.
120. Hutchinson, J. and Z. Suo, *Mixed mode cracking in layered materials.* Advances in Applied Mechanics, 1991(29): p. 63-191.
121. Weinan, Z., et al., *Advancements in 2D flexible nanoelectronics: from material perspectives to RF applications.* Flexible and Printed Electronics, 2017. **2**(4): p. 043001.

122. Kim, S.J., et al., *Materials for flexible, stretchable electronics: graphene and 2D materials.* Annual Review of Materials Research, 2015. **45**(1): p. 63-84.
123. Na, S.R., et al., *Clean graphene interfaces by selective dry transfer for large area silicon integration.* Nanoscale, 2016. **8**(14): p. 7523-7533.
124. Needleman, A., *An analysis of tensile decohesion along an interface.* Journal of the Mechanics and Physics of Solids, 1990. **38**(3): p. 289-324.
125. Jain, S., et al., *A cohesive zone model and scaling analysis for mixed-mode interfacial fracture.* International Journal of Solids and Structures, 2017. **129**: p. 167-176.
126. Bao, G. and Z. Suo, *Remarks on crack-bridging concepts.* Applied Mechanics Reviews, 1992. **45**(8): p. 355-366.
127. Sills, R.B. and M.D. Thouless, *The effect of cohesive-law parameters on mixed-mode fracture.* Engineering Fracture Mechanics, 2013. **109**: p. 353-368.
128. Xin, H., et al., *Adhesion energy of as-grown graphene on copper foil with a blister test.* Carbon, 2017. **123**: p. 243-249.
129. Park, K. and G.H. Paulino, *Computational implementation of the PPR potential-based cohesive model in ABAQUS: Educational perspective.* Engineering Fracture Mechanics, 2012. **93**: p. 239-262.
130. Andres, C.-G., et al., *Deterministic transfer of two-dimensional materials by all-dry viscoelastic stamping.* 2D Materials, 2014. **1**(1): p. 011002.
131. Buscema, M., et al., *Photovoltaic effect in few-layer black phosphorus PN junctions defined by local electrostatic gating.* Nature Communications, 2014. **5**: p. 4651.
132. Nabil, H.A., et al., *Flexible displays: wavy architecture thin-film transistor for ultrahigh resolution flexible displays (Small 1/2018).* Small, 2018. **14**(1): p. 1870002.
133. Dennler, G. and N.S. Sariciftci, *Flexible conjugated polymer-based plastic solar cells: from basics to applications.* Proceedings of the IEEE, 2005. **93**(8): p. 1429-1439.
134. Someya, T., et al., *A large-area, flexible pressure sensor matrix with organic field-effect transistors for artificial skin applications.* Proceedings of the National Academy of Sciences of the United States of America, 2004. **101**(27): p. 9966-9970.
135. Wagner, S., et al., *Electronic skin: architecture and components.* Physica E: Low-dimensional Systems and Nanostructures, 2004. **25**(2): p. 326-334.
136. Nathan, A. and B.R. Chalamala, *Special issue on flexible electronics technology, part 1: systems and applications.* Proceedings of the IEEE, 2005. **93**(7): p. 1235-1238.
137. Na, S.R., et al., *Cracking of polycrystalline graphene on copper under tension.* ACS Nano, 2016. **10**(10): p. 9616-9625.